UNIVERSITÀ
DEGLI STUDI
DI TRIESTE

Università degli Studi di Trieste

XXXV Ciclo del Dottorato di Ricerca in
Earth Science, Fluid-Dynamics, and Mathematics. Interaction and Methods

PHYSICS AND MODELLING OF GENERATION AND PROPAGATION OF NOISE BY COMPLEX SOURCES IN REALISTIC BASINS

Settore scientifico-disciplinare: ICAR/01

Ph.D. Student:	Giovanni Petris
Ph.D. Program Coordinator:	Prof. Stefano Maset
Supervisor:	Prof. Vincenzo Armenio
Co-Supervisor:	PhD. Marta Cianferra
Co-Supervisor:	PhD. Angelo Camerlenghi

Academic Year 2021–2022

Author: Giovanni Petris

e-mail: giovanni.petris@phd.units.it

Dipartimento di Ingegneria e Architettura,
University of Trieste, Piazzale Europa 1,
34127 Trieste, Italy

Supervisor: Prof. Vincenzo Armenio

e-mail: vincenzo.armenio@dia.units.it

Affiliation: Dipartimento di Ingegneria e Architettura,
University of Trieste, Piazzale Europa 1,
34127 - Trieste - Italy

Co-Supervisor: PhD. Marta Cianferra

e-mail: marta.cianferra@dia.units.it

Dipartimento di Ingegneria e Architettura,
University of Trieste, Piazzale Europa 1,
34127 - Trieste - Italy

Co-Supervisor: PhD. Angelo Camerlenghi

e-mail: acamerlenghi@ogs.it

Affiliation: Istituto Nazionale di Oceanografia e di Geofisica Sperimentale - OGS,
Borgo Grotta Gigante 42/C,
34010 - Sgonico (TS) - Italy

Day of the defence: 23.03.2022

To cite this work: Giovanni Petris, *Physics and modelling of generation and propagation of noise by complex sources in realistic basins* , Ph.D. Thesis, School of Earth Science, Fluid-Dynamics, and Mathematics. Interaction and Methods, University of Trieste (2022). Digital resource deposited in the National Legal Deposit service. NBN: *to be assigned.*

Abstract

The need to develop more accurate numerical tools for the propagation of noise in underwater environments is driven by the continuous increase of human activity in the sea and coastal areas. Noise has been shown to be dangerous to marine wildlife, and steps should be taken soon to mitigate it. Knowing that the primary sources of noise pollution at sea are marine propellers, one of the problems is assessing how the noise generated interacts with the environment, since up to now, the main focus was the characterization of the acoustic signature in the near field or, alternatively, the propagation of simplified acoustic sources in sea-like domains.
The work conducted in this thesis assesses the modeling of complex acoustic sources and the propagation of acoustic pressure in realistic domains. A propagation model based on the solution of the acoustic wave equation in the time and space domain is implemented and used in conjunction with the Ffowcs Williams and Hawkings (FW-H) to analyze the possible patterns occurring in the underwater environment. Specifically, we analyzed the noise radiated by a marine propeller in a canal, focusing on the effects of the boundaries on the acoustic field and, secondly, the consequence of a rotating body placed underneath a free surface. We defined a new methodology called Full Acoustic Analogy (FAA) to achieve these results. This methodology aims to overcome some intrinsic limitations of the known Acoustic Analogies. The study presented here attempts to bridge the gap between noise characterization and its propagation by introducing a new methodology for evaluating flow-induced noise in a realistic environment.
The propagation model developed, which used the finite-difference-time-doamin method has been compared against benchmark cases (monopole source propagating in classical waveguides) for which an analytical solution is available, and it provides accurate results of the acoustic field. Furthermore, a second analysis is conducted on two classical waveguides: the Ideal one and the Pekeris one. The solution of the wave equation in time and physical space enables the implementation of different sources, such as dipole and quadrupole; therefore, we analyzed the acoustic response of the Pekeris waveguide. The results show that the propagation of the acoustic pressure is strongly affected by the directivity pattern of the source. This was the first step in evaluating the capabilities of the solution of the acoustic equation in the presence of sources characterized by complex directivity since our ultimate goal is to evaluate the noise emitted by a propeller.
The analysis of the complex noise field in the near field can be conducted with two different numerical approaches. The first approach, defined as direct, relies on the solution of

the compressible Navier-Stokes equations. A Direct Numerical Simulation is necessary to resolve all the length scales associated with the fluid flow and the acoustic regime. The compressible nature of the numerical experiment allows the direct evaluation of the acoustic pressure. This approach's drawback is its limited applicability to realistic cases since it requires a significant amount of computational power and consequently limits the capability to evaluate propagation in an extended environment. The second approach relies on a hybrid method. The so called acoustic analogies allows the decoupling of the fluid flow computation from the acoustic pressure computation. The fluid flow solutions collected at different time windows are then used as a source term for evaluating the far-field acoustic pressure. This method needs an acoustic analogy, a set of equations that describe how to convert the kinetic energy of the fluid flow into acoustic energy, which is then propagated in the far field. Among acoustic analogies, the equation of FW-H is best suited to evaluate the acoustic pressure generated by an immersed body in motion. It is largely applied to rotating machines, such as marine propellers, which are the subject of study in this thesis. The significant limitations of acoustic analogies are the conditions necessary for their application.

The most stringent is that the domain where noise propagates has to be infinite in length and with constant physical properties, such as the density and speed of sound. So any mechanism of refraction and reflection may be difficult or, in some cases, impossible to reproduce. Different boundaries, such as the air-water interface and the seabed, generally confine the marine environment, where gradients of density and speed of sound are also present. The study presented here attempts to bridge the gap between the generated noise's characterization and propagation by introducing the FAA methodology for evaluating flow-induced noise in a realistic environment.

The FAA analogy is introduced, and we describe how the acoustic pressure obtained with the FW-H equation is used as a source term in the propagation model. After the validation of the new proposed methodology in an unbounded homogeneous domain, we investigate the propagation of the linear part of the noise generated by a naval propeller within a canal. Local maxima and minima of the acoustic fields arise from the interaction between the noise source and the environment; in particular, they derive from the superposition of direct and reflected waves. Moreover, a rotating body placed underneath a free surface generates a peculiar asymmetry of the acoustic field associated with the interaction between the acoustic waves and the free surface.

Contents

Chapter 1

Introduction

Human activity continually impacts the environment. Unfortunately, one of the results is pollution. We are accustomed to the image of the effects of pollution as smog in the cities or an oil spill in the ocean, but we are less prone to identify the effects of noise pollution in the underwater environment. Most of the research conducted in the past decades has focused on mitigating the noise emissions of human activity inland. For example, progress in reducing noise generated by jet aircraft led to a new field of research called aeroacoustic [43].

In recent years, the increasing use of shipping for global trade, the continued anthropization of natural coastal areas, and the construction of pervasive offshore structures have increased the interest in the effects of noise emissions on the marine environment, particularly on the fauna [70, 23]. The hazard associated with the input of acoustic energy (noise) in the marine environment has been recognised by the United Nations Convention on the Law of the Sea (UNCLOS) [51] in1982. More recently (2008), the European Union created a framework [21] to monitor and mitigate the anthropogenic impact on the marine environment, focusing, among the others, on underwater noise.

Numerical and physical experiments have revealed that in the low-frequency region (below 200 Hz), the primary source of noise produced by a ship is the propeller [32]. More stringent regulations defined by the Maritime Safety Committee ([16]) on noise emission have led the shipbuilding companies to design silent class ships, to reduce their environmental impact. However, predicting how the noise source interacts with the marine environment is still challenging due to the difficulties in performing numerical and physical experiments in real scenarios. Therefore, there is a need to develop numerical tools that accurately describe noise generated by complex systems and its propagation in the marine environment, as suggested by the International Maritime Organization [52].

In laboratories for hydroacoustics experiments, increasingly sophisticated techniques have been developed, see for example Felli et al. [25] where a novel wavelet-based filtering procedure is adopted to investigate the near-field pressure fluctuations on a rudder at different deflection angles. The laboratory experiments are suitable to evaluate the acoustic signature of the propeller in the vicinity of the noise source. However, the propagation of

a signal over long distances cannot be correctly predicted.
Experiments of the noise generated by ships in operational conditions have been performed, but typically these experiments are opportunistic, such as the measurements conducted in the Santa Barbara Channel [46]. Furthermore, the experimental conditions, the ship type and the environment's state may differ substantially from case to case. Therefore, this type of measurements are suitable for acquiring coarse estimations of the noise generated but are not suited to gaining a better understanding of the interaction between the environment and the source.
Among the possible computational approaches, the acoustic analogy is widely in use in the scientific community. The acoustic analogy consists of a hybrid method where the computation of the acoustic field is decoupled from that of the hydrodynamic field. First, a hydrodynamic field is obtained using a computational method and, successively, the hydrodynamic data are given as input to the acoustic model. The hydrodynamic field is usually evaluated using unsteady Reynolds-averaged Navier-Stokes (URANS), Detached Eddy Simulations (DES), or Large-Eddy Simulation (LES) (see the review of [69]). Among the available methods, LES and DES represent the best compromise between effectiveness and efficiency to resolve correctly the flow unsteadiness responsible of noise production [48, 34, 58]. The theory behind the acoustic model was originally developed by Lighthill [43], Ffowcs-Williams and Hawkings (FW-H) [26], and Curle [17]. Among the acoustic models, the FW-H equation is suitable for characterizing the noise generated by an immersed body in motion, and is of common use in the scientific community for the evaluation of propeller noise, see among others [9, 3, 38]. Specifically, for a ship propeller or, in general, a rotor, the noise associated to the load on the blades and their rotation is of a tonal type and shows main peaks at frequencies Nn and n, where N and n are respectively the number of blades and the revolution rate, whereas the noise associated with the wake is broadband and confined in the low-frequencies (see [69] and [15] and literature therein reported).
the main limitation of the acoustic analogy lies in the propagation domain characteristics. Indeed, the propagation of the acoustic pressure given by FW-H is assumed to occur in an infinite homogeneous domain, namely variation of the density field and associated speed of sound cannot be considered along with the presence of boundaries. The only remarkable exception is the presence of a plain free surface, which can be simulated considering the half-space Green function within the solution of the integral terms composing the FW-H equation ([13] for a detailed discussion and application). Therefore, the sole use of the acoustic analogy for the propagation in realistic marine environment is insufficient. For this purpose, to overcome the acoustic analogies limitations, we propose a new methodology called Full Acoustic Analogy (FAA), which combines the classical acoustic analogy with a propagation model.
This new methodology (FAA) is based on three-step: i) the numerical solution of the fluid flow of the problem of interest, ii) the evaluation of the acoustic pressure generated by the fluid flow with the FWH equation at specific microphones, iii) the propagation of the acoustic pressure in a complex environment. The last step allows to evaluate the propagation of the acoustic pressure in environments with multiple boundaries and characterized by the variation of density and speed of sound. In this sense, the proposed methodology is

an extension of classical acoustic analogies based on the hybrid method. Being a general methodology, it can serve for various applications, considering both hydro and aero-acoustic frameworks.
An underwater problem is usually defined by three different aspects, such as frequency of the source, depth of the water column, and the range-dependent environment; consequelntly, different models must be used concerning the type of problem. There are different models for the propagation of an acoustic signal, we choose to solve the wave equation in the space-time domain, as there are several advantages, first of all the possibility of directly using the FW-H data and being able to consider complex sources.
The problem we faced was that the acoustic wave equation solved in time and space is not one of the most studied propagation models, at least for underwater noise propagation. Indeed, the principal propagation model uses the solution of the Helmholtz equation. The propagation of a simple acoustic source in a heterogeneous environment can be evaluated by considering the wave equation recast in the frequency domain, thus solving the Helmholtz equation. In marine acoustics, several important applications of this method are found in [71, 49]. Solving the Helmholtz equation has a low computational cost when the numerical domain is two-dimensional, but it has some limitations on the source's complexity (especially when complex directivity patterns are present). The ability to use complex directivity sources in the propagation model is fundamental for coupling with acoustic analogies. Indeed, propagation models based on the Helmholtz equation are typically problem-oriented methods.
On the other hand, solving the wave equation on the physical space-time domain is suitable for studying the propagation low-frequency sources in 3D domains of limited extension, up to a few kilometers. Consequently, the use of the wave equation in the physical domain was somewhat abandoned in the past due to the high computational cost and the interest in the propagation of the noise at very large distances, of the order of hundred kilometers. However, nowadays, interest has raised in the analysis of near-field acoustics because of the anthropogenic noise (marine vessel, geophysical exploration, ...) in confined regions, such as canals, ports or fjords. In this case, the main advantage of the wave equation solution in the physical domain consists in the possibility of treating complex sources together with the environment's variability. However the use of this methodology in the marine environment is still unexplored, and few references are available [27, 30]. Therefore, we needed to develop a numerical algorithm for the the solution acoustic wave equation in the physical space using a Finite-Difference-Time-Domain (FDTD).
In the first part of the study, we develop the numerical algorithm adopted for solving the wave equation was implemented, considering a Finite-Difference-Time-Domain (FDTD) method. The complex part of the algorithm is the implementation of the open-boundary conditions, which allows the acoustic wave equation to exit the numerical domain. Then we compared the solution obtained with the acoustic wave equation against benchmark cases (monopole source propagating in classical waveguides) for which an analytical solution is available. The analysis is conducted on two classical waveguides: the Ideal one and the Pekeris one. The results obtained with the acoustic wave equation are comparable with analytical results, verifying the correctness of the propagation method. Moreover, the

solution of the wave equation in time and physical space enables the implementation of different sources, such as dipole and quadrupole; therefore, we compared the effects on the acoustic field of these sources in the two classical waveguides. Some issues related to the source implementation have been addressed at this stage. Alongside the use of the so called hard source method, we defined a new hard image source method that performed better when a close boundary is present in the propagation domain. All the work presented in the first part has been published in [54].
In the second part of the study, we developed the FAA methodology in detail, along with the coupling between the FW-H equation and the acoustic wave equation. We verified the FAA methodology using a marine propeller as a case study. For this purpose, the results of the Large-Eddy Simulation or LES of a marine propeller, based on the simulation done in [15], have been exploited. We were able to verify that the noise associated with the blades' loads and rotation was correctly evaluated. Specifically, considering homogeneous and unconfined domains, the acoustic pressure from the FAA model overlaps the signal predicted by the FW-H equation. The propagation of the linear part of the FW-H is reproduced correctly with the acoustic wave equation.
After verification of the new methodology, we were able to evaluate the propagation of the acoustic pressure generated by a marine propeller in a canal, evidencing the effects of the boundaries on the acoustic field. This is the first example that highlights the advantages of this methodology. In addition, the specific case of a rotating propeller placed below a free surface is analyzed, where a characteristic asymmetry of the acoustic field is found and examined. In [53] we have published the new methodology and the analysis conducted on the propagation in closed domain.
In the last part, we examined the effects of the density e speed of sound variability on the propagation of the noise generated by a real scaled propeller, applying the scaling of the acoustic pressure proposed in [13] for the source. The distinct acoustic patterns that emerged from the stratification were investigated. This aspect is of fundamental importance since stratification is always present in a marine environment and may largely affect the propagation of acoustic pressure.

Chapter 2

Propagation Models

Acoustic wave propagation in complex domains is a wide field of research; indeed, the characteristic of the environment may primarily affect the acoustic field, depending on their specific characteristics. For example, the sound emitted by a musical instrument in a room is affected by the wall's geometry; this moved the study of suitable materials or devices able to absorb the incoming acoustic waves. On the other hand, the noise of a flying aircraft travels in approximately unbounded domains. However, in this case, the air's inhomogeneities along the air column can play an important role in noise propagation. When considering an acoustic source placed underwater, the seabed's morphology, sediment rheology, and the water column's inhomogeneities affect the acoustic response. Therefore, the study of the propagation of acoustic waves in an underwater environment is still an undergoing field of research due to its complexity.
Two main approaches to computing wave propagation are solving the wave equation in a time-space domain or considering its equivalent formulation in the frequency domain, thus solving the so-called Helmholtz equation. The latter approach is the most used so far due to the low computational cost compared to the wave equation solution in the time and space domain. In recent years, the interest in the first approach has increased to overcome some limitations of the solution in the frequency domain, such as implementing complex directivity and narrow-band sources (opposite to monochromatic sources), which are not always representative of anthropogenic sources. In this work, we focused on the solution of the acoustic wave equation in the time and space domain due to its advantage over the Helmholtz equation. A brief description of the Helmholtz equation and its application in the marine environment is presented in the next section 2.1, followed by a introduction to the application of the wave equation in the marine environment in section 2.2

2.1 Helmholtz Equation Propagation Model

The principal numerical models to compute the propagation of acoustic waves at sea relays on the solution of the Helmholtz equation. This choice was driven by the necessity of computing the propagation at a very long distance (order of ten-to-hundred kilometres along

the horizontal directions), which is achievable due to the low computational cost associated with the Helmholtz equation's solution. Therefore, established literature and algorithm are available to compute the propagation of acoustic waves in marine environments.
The solution of the Helmholtz equation can be computed with different numerical methods, such as the Wavenumber Integration (WI), Normal Mode (NM) and Parabolic Equation (PE). These numerical models have different domains of applicability concerning the problem under investigation. In the review of [24], an overview of most of the available models is given. In general, an underwater sound propagation problem is characterised by three factors. First, is the range of frequency of the source, where low frequencies are considered below $500\,Hz$. The second factor is if the morphology of the domain change or not with the distance from the source (range-dependent or range-independent problem). The third factor is the source depth compared to the water column, whether the source is in shallow or deep water.
One of the limiting factors of the Helmholtz equation is that the solution is usually obtained in a two-dimensional (2D) domain. The acoustic pressure is computed over vertical slices of the ocean environment. These slices are bounded by a free surface above, and the seabed below and are defined as fluid waveguides. Despite in the past, the propagation in the three-dimensional (3D) space has been addressed [68], these results were not achieved by solving the Helmholtz equation in a fully 3D domain, but in a reconstruction of the domain composed of $N \times 2D$ slices along the azimuthal direction, still solving the propagation in two-dimensional (2D) domain. This approach was necessary to reduce the computational cost of solving the Helmholtz equation in 3D, which is comparable to the solution of the wave equation in the time and space domain. In [65], a comparison between the two approaches $N \times 2D$ versus fully 3D, has been carried out within an ocean canyon, which is one of benchmark for the study of acoustic propagation in 3D domains. The 3D approach was found to estimate a higher sound pressure level inside the canyon than the $N \times 2D$, highlighting the latter's limitations. There is a necessity of utilize full 3D domain for correctly estimating the propagation of acoustic waves and therefore this is still an undergoing field of research for the scientific community [44].
Typical solutions of the Helmholtz equation are obtained with omnidirectional sources, also referred to as point sources. These assumptions can be considered valid when concerned with the propagation to very long distances. However, in reality, most of the anthropogenic sources have a significant directivity, meaning that sound emission has not a spherical symmetry but a preferred direction of emission. The evaluation of the noise emission in the vicinity of the source should take in consideration the directivity of the source. Considering a directivity pattern in the Helmholtz equation is not straightforward, and it is possibile only in specific cases. Analytical approaches have been employed by Kuznetsov et al. [41, 42] to evaluate the directivity of moving monopole, dipole, and quadrupole in a layered medium. These results are valid only on a particular waveguide, which represents a simplified marine environment. Therefore the method is not of general application and is not for more complex bathymetry or specific cases.
We refer the reader to the book of Jensen et al. [37] for in depth descrption of the numerical approach to the solution of the Helmholtz equation.

2.2 Wave Equation Propagation Model

The solution of the wave equation in the time and space domain requires more computational resources than the Helmholtz equation's solution. In recent years the available computational resources have increased, and it is now possible to solve the wave equation directly, although in smaller domains (up to a few kilometers) and the low-frequency regime. Indeed, this approach is limited to specific cases. However, most of the anthropogenic activity at sea occurs near the coast in a limited area where the 3D effects of the environment are of fundamental importance for the propagation of noise emission. Moreover, the wave equation is more suitable for evaluating the interaction of the complex directivity pattern of the source with the surrounding environment.
Among the possible discretization method we choose is the finite-difference-time-domain (FDTD). However, the use of the FDTD for the solution of the propagation of acoustic waves in a marine environment is still quite undiscovered, consequently few litterature is available. The first study was conducted by [27]. The author considered a two-dimensional axial symmetric domain, using the FDTD approach and focused on the scattering of Arctic ice, taking into consideration the elasticity of the medium. This first example was conducted with the FDTD since it is more capable of treating scattering from an object than the Helmholtz equation. More recently, the FDTD method was applied to study the noise generated by marine hydrokinetic power devices [30]. In this case, the authors solved the wave equation coupling the velocity–pressure equations by adopting the FDTD method in a three-dimensional space. The source noise considered, the hydrokinetic power devices, was still a monochromatic omnidirectional source. Therefore, it was still not representing a real anthropogenic source. The use of the wave equation instead of the Helmholtz equation was by necessity to model accurately the morphology of the coastal area where the hydrokinetic power devices were placed.
Several studies have been conducted in room acoustic [7, 61]. The advantage of room acoustics is that the propagation domain is limited and closed, making the wave equation solution better suited. However, most of the sources considered are still represented by analytical functions. Recently, the research in room acoustic has developed multiple approaches to implementing complex acoustic sources [1]. These results can readily be applied to propagation in a marine environment.
Apart from the higher computational cost compared to the Helmholtz equation, the other limiting factor of solving the wave equation in the time-space domain is the implementation of the open-boundary conditions. These boundary conditions allow acoustic waves to exit from the numerical domain, avoiding spurious reflection. Unless simple 1D cases are considered [22], where there is an exact formulation that avoids completely spurious reflection, these conditions are not exact for higher dimensions. Numerous types of open-boundaries conditions were proposed [28], and still is an ongoing field of research. Moreover, the complexity of these boundary conditions increases with the order of the scheme used to solve the wave equations.

2.3 Numerical Solution of the Acoustic Wave Equation

The solution of the wave equation with the FDTD is a classical numerical problem. The preferred method to solve the wave equation is to solve the pressure and velocity equations separately. This approach was necessary for seismologic research, where the knowledge of velocity and acceleration of the ground is fundamental to assessing the risk in the event of an earthquake. This choice is also the preferred method for room acoustic, where the main objective is to understand sound propagation in a closed environment. In a marine environment, the knowledge of velocity is secondary. Instead, the main concern is to evaluate the pressure level. Therefore, it is preferable to solve only for pressure, solving the acoustic wave equation. The main limitation of this approach is the less literature available for implementing the boundary condition, which is one of the critical problems of the wave equation, particularly the open boundary conditions. These boundary conditions allow the waves to exit the numerical domain, mimicking an infinite domain. The algorithm to solve the acoustic wave equation has been developed using the Julia programming language [5]. In the following 2.3.1 section, the acoustic wave equation is introduced, and in 2.3.2 the description of the numerical method implemented for solving the acoustic wave equation is presented. In 2.3.4, a discussion on the avaible approach to implement the source is presented.

2.3.1 Acoustic Wave Equation

An acoustic source generates small perturbations of pressure which propagates as waves. In a quiescent fluid, the pressure field p, perturbed by acoustic waves, is

$$p = p_0 + p',$$

where p_0 is a bulk value (*i.e.*, the hydrostatic pressure field) and p' a pressure perturbation. The pressure field is in relation to an equivalent density field

$$\rho = \rho_0 + \rho',$$

where ρ_0 is the bulk density giving rise to p_0, and ρ' is the density perturbation associated to p'. According to the linear wave equation, the perturbation propagates from a source point in the three-dimensional space. The acoustic wave equation derives from the linearization of the mass and momentum conservation equations, assuming an inviscid fluid and adiabatic transformations. The three-dimensional acoustic wave equation for an inhomogeneous fluid reads as:

$$\frac{1}{c(\mathbf{x})^2}\frac{\partial^2 p'(\mathbf{x},t)}{\partial t^2} = \rho(\mathbf{x})\nabla\left(\frac{1}{\rho(\mathbf{x})}\nabla p'(\mathbf{x},t)\right) + S(\mathbf{x},t), \tag{2.1}$$

where c is the local speed of sound, $\mathbf{x}$ is the coordinate vector, t is time, and S is a source term. Hereafter, the symbol ($'$) is omitted for the sake of clarity. A rigorous derivation of the acoustic wave equation is described in [56].

The solution of this equation provides the acoustic pressure in all the space at every time, and variation of density and speed of sound directly affects the propagation. When the solution is obtained in the time and space domain, compared to the frequency domain (i.e., Helmholtz equation), the fluid property can change in all the 3D directions, overcoming the usual assumption of the idealized stratified medium. Moreover, the morphology of the seabed, which is of fundamental importance for reflecting the acoustics eaves, can be constructed and addressed more straightforwardly. The second important aspect is that the source term is also represented in the space and time domain. Therefore anthropogenic sources can be used if the knowledge of the pressure in time and space is available.
The acoustic wave equation assumes that all the mediums in the domain are considered fluid since the shear component of the velocity is not considered. The approximation is exact for all fluids and is an approximation for any solid material. However, the approximation fails to represent solids in which the shear wave speed is comparable to the velocity of the compressional wave. In general, we are concerned about the propagation in the vicinity of the source in a marine environment. If this is the case, this assumption is valid since the upper layer of the seabed, which is relevant for the propagation in the vicinity of the source, is composed of sediment, such as sand. Another consideration is that solid materials with a high shear velocity have also a very high density compared to water. Therefore, most of the energy is reflected at the interface with water.
In this formulation, the second assumption of the acoustic wave equation is that the propagation is not dissipative. Therefore, the amplitude of the acoustic waves is a function only of the distance from the source and the characteristic of the propagation domain. This can be considered a strong assumption, but water does not exhibit strong acoustic energy dissipation unless for frequency above $1000\,Hz$ and over distances of the order of ten-to-hundred Km. Therefore, water is a non-absorbing medium for low-frequency sources ([1]). This assumption is not valid for solid materials, even at low frequencies, since solid materials are always dissipative. The relation between stress and strain rules energy absorption in a solid material. But as stated before, in this formulation, all the mediums are considered fluids and, therefore, not dissipative. In the work of Petrov [55], a different formulation of the acoustic wave equation is presented, which considers the solid material's viscoelasticity effects. This formulation of the acoustic wave equation should be considered when the effects of dissipation are considered relevant to the problem of interest.

2.3.2 Numerical Implementation

The acoustic wave equation (2.1) is solved using the FDTD method, and the derivatives are approximated using finite differences. The $3D$ domain is Cartesian, and all the cells have the same length in all directions; hence, the domain is composed of cubic cells. Pressure, density and speed of sound are defined over the cells vertices. The integration of equation (2.1) is explicit. A second-order finite difference scheme approximates both the time and the spatial derivatives; therefore, the algorithm is second-order accurate both in time and space.
Here we introduce the discrete form of Eq.(2.2) in a one-dimensional space plus an ad-

ditional term necessary to implement the open-boundary conditions, which are discussed later. Indeed, to solve the wave equation al the boundary conditions of the problem must be defined.

$$p_i^n = -p_i^{n-2} + 2p_i^{n-1} + \frac{\Delta t^2}{\Delta x^2} c_i^2 \rho_i * \\ * \left[\frac{1}{2} \left(\frac{1}{\rho_{i+1}} + \frac{1}{\rho_i} \right) \left(p_{i+1}^{n-1} - p_i^{n-1} \right) - \frac{1}{2} \left(\frac{1}{\rho_i} + \frac{1}{\rho_{i-1}} \right) \left(p_i^{n-1} - p_{i-1}^{n-1} \right) \right] \tag{2.2}$$

where p_i^n is the acoustic pressure at the point defined by the index i at the iteration time n. The source term S is not treated explicitly since we used the hard source method for implementing the source, which is discussed in the next subsection. Fixing the length of the domain to L_x and the number of cells to n_x, a discrete position along the x-*direction* is defined as $x_i = i\Delta x$, $i \in [0, n_x]$. The variable of the problem are then defined at each vertices x_i. The overall time of the simulation is $T = n\Delta t$, where Δt is the time interval, consequently the time step is constant. The indices $n-1$ and $n-2$ denote the two previous time steps, respectively. In order to evaluate the pressure at time n, it is only required the knowledge of the pressure at the two previous time iteration.
The time interval Δt is defined by the stability criterion of the numerical method. With the use of the Von Neumann stability analysis, the stability criterion for the proposed numerical scheme is evaluated as

$$\Delta t \leq (1/c) * (1/dx^2 + 1/dy^2 + dz^2)^{-1/2}.$$

The choice of the spatial discretisation is driven by the maximum source frequency of the source. Indeed, to solve the wave equation, a minimum number of grid points *per* wavelength is required and for the second-order finite difference scheme, is 8 [19].
All numerical methods are characterized by numerical dispersion. The discretization of the wave equation introduces a discretized speed of sound, a function of the grid spacing. For a second-order numerical scheme, the dispersion error is such that higher frequencies tend to travel with a lower speed of sound compared to the lower frequencies. The dispersion error can be alleviated by increasing the minimum grid points *per* wavelength, therefore increasing the computational cost or increasing the order of the numerical scheme.
The density, (ρ_i), and speed of sound (c_i) of the ambient fluid are assigned at the each cell vertices of the computational grid. Therefore, the value of these two properties can vary along the domain, and variation of the property along the fluid column can be addressed. The variation of these two properties can also be used to define seabed morphology. The computation of the laplacian term required the value of the density at the midpoints between two vertices. To obtain the midpoint value and interpolation is required. In Eq 2.2 the harmonic mean is used, but other interpolation method can be implemented. We chose this interpolation method since is more stable in the presence of a sharp density gradient. Note that, in general, the density and speed of sound are a function of time. Nonetheless, the time scale associated with acoustic wave propagation is very small compared to the time scale of the variation of marine environment property.

The solve the wave equations also, the boundary conditions must be prescribed. In this work, we considered three boundary conditions: Dirichlet, Neumann and open-boundary. The Dirichlet boundary condition is obtained by imposing the desired acoustic pressure value at the boundary points

$$p_i^n = p(\mathbf{x}, \mathbf{t}),$$

where $p(\mathbf{x}, \mathbf{t})$ is the known value of acoustic pressure, and p_i^n is the corresponding discretize position and time. The air-water interface is an example of the application of the Dirichlet boundary condition. In this case, the interface is represented by imposing a pressure-free boundary condition $p = 0$; therefore, all the acoustic energy is reflected into the domain. This is a good approximation since the transmission coefficient is almost zero due to the sharp gradient of density and speed of sound at the interface [8]. As a result, the amplitude of the reflected waves is equal to the incident one, apart from a 180° phase shift. This is the standard procedure used in all the propagation model, but more research should be conducted on this approximation due to the recent work of Godin [29], which highlight anomalous transparency of the water-air interface for very low-frequency sources.
The Neumann boundary condition is obtained by imposing the desired derivative of acoustic pressure at the boundary points

$$\frac{p_{i+1}^n - p_{i-1}^n}{2\Delta x} = \frac{\partial p(\mathbf{x}, \mathbf{t})}{\partial x} = 0$$

. The interface between a solid medium and water can be approximated with the Neumann boundary condition. This approximations is valid when the density of water is lesser than the one of the solid medium, and in this case, the transmission coefficient is considered 1. Therefore al the acoustic waves are reflected without a phase shift.
A wave without attenuation, apart from the geometrical spreading, is able to propagate to infinity, but the numerical domain must be limited. In absence of a reflective boundary that constrains the energy, the waves have to leave the numerical domain, making necessary the implementation of an open-boundary condition. For low-order schemes and 1-D problems, exact open-boundary conditions are available, which damp the wave's amplitude without reflecting energy inside the domain [22]. For 3-D problems, different types of open-boundary conditions were proposed in the literature to minimize spurious reflection inside the domain since there isn't an exact solution. Therefore, any type of open-boundary condition for a 3-D problem is subject to spurious reflection. Among the different types of open-boundary we implemented the Perfectly Matched Layer (PML) method, described in [11]. The PML proposed by Chern [11] is exact, to machine zero, for homogenous cases (where no jump in density occurs) and exhibits small reflection in the presence of density discontinuities. The PML method introduces a buffer layer, a new portion of the numerical domain defined as the PML region, adjacent to the real numerical domain where the acoustic waves propagate. The acoustic waves entering the PML regions are damped without reflecting energy at the interface with the real domain. This result is obtained by solving a modified wave equation

2.3 in this region.

$$\begin{cases} p_i^n = -p_i^{n-2} + 2p_i^{n-1} + \dfrac{\Delta t^2}{\Delta x^2} c_i^2 \rho_i * \\ \quad * \left[\dfrac{1}{2} \left(\dfrac{1}{\rho_{i+1}} + \dfrac{1}{\rho_i} \right) \left(p_{i+1}^{n-1} - p_i^{n-1} \right) - \dfrac{1}{2} \left(\dfrac{1}{\rho_i} + \dfrac{1}{\rho_{i-1}} \right) \left(p_i^{n-1} - p_{i-1}^{n-1} \right) \right] + \\ \quad + \dfrac{\Delta t^2 \rho_i c_i}{\Delta x} \left(\sigma_i \psi_{i+1}^{n-1} - \sigma_{i-1} \phi_{i-1}^{n-1} \right), \\ \phi_i^n = \phi_i^{n-1} - \dfrac{1}{2} \Delta t c_i \left(\sigma_{i-1} \phi_{i-1}^n + \sigma^n s_i \phi_i \right) - \dfrac{1}{2\Delta x} \left(p_{i+1}^{n-1} - p_{i-1}^{n-1} \right) \\ \psi_i^n = \psi_i^{n-1} - \dfrac{1}{2} \Delta t c_i \left(\sigma_{i-1} \psi_i + \sigma_i \psi_{i+1} \right) - \dfrac{1}{2\Delta x} \left(p_{i+1}^{n-1} - p_{i-1}^{n-1} \right). \end{cases} \tag{2.3}$$

In Eq. 2.3, we see an additional term not present in Eq. 2.2, which contains two auxiliary variables ψ, ϕ and a damping coefficient σ, and two separate equations for the evaluation of the time evolution of ψ, ϕ. The *damping coefficient* σ is set to $\sigma_i = 1/\Delta x$, as suggested in [11], in the PML region and 0 in the real region. With this condition, in the real region, Eq. 2.2 is recovered to correctly evaluate the acoustic waves' propagation. The variables ψ, ϕ , defined at the cell vertices (i) of the numerical grid, are used to dampen the acoustic pressure in the PML region and are evaluated from the pressure field. The variables are initialized (at time step $n = 0$) as zero. In three dimensions, a total of six equations for the auxiliary variables are defined since two auxiliary variables are introduced for each direction. The only free parameters to be set are the PML thickness (i.e., the number of grid points where the *damping coefficients* σ_i is not zero.) We found that imposing a thickness length proportional to the principal wavelength of the source is sufficient to obtain satisfactory damping of the incoming waves together with negligible numerical reflections of the pressure waves at the interface between the PML region and the real region. The equations presented here are solved in a dimensional form opposite to the non-dimensional one presented in [11].

2.3.3 Source Implementation

The acoustic waves originates from a source, and it must be implemented in the numerical scheme. Most of the studies on implementing acoustic source are done in the room acoustic fields [6, 64]. The results of these studies can be adapted to underwater acoustic. In general, underwater sources are less critical concerning numerical errors since they are associated with a low-frequency range compared to the room acoustic. Among the possible strategies of implementing the source, three are commonly in use, namely the *hard source*, the *soft source*, and the *transparent source*.

The *hard source* may be considered the simplest and most effective method. The known acoustic pressure is imposed at the source node(s), as a time-varying Dirichlet boundary condition. In these source node(s) the wave equation (2.1) is not solved since the pressure is imposed at each time step. Therefore, the source function S is set to zero in the computational domain. In Figure 2.1, we show the nodes close to the source, the latter depicted

in red. If the pressure values representing the source are known at specific nodes, they can be used as a source node(s), and in Figure 2.1 illustrates these nodes in grey. From these nodes, the acoustic pressure is propagated into the numerical domain.

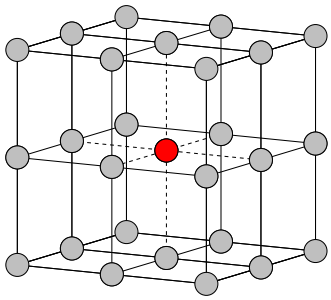

Figure 2.1: Schematic of the hard source implementation. The red dot is the source and the grey dots represent the computational grid points where the pressure signal is imposed as boundary condition.

In this work, we use the hard source method for its simplicity and because it is possible to define the value of pressure evaluated using analytical function exactly. Moreover, if the pressure of a more complex source is known at specific points, which coincides with the points of the numerical grid, the pressure from that points can be propagated into the numerical domain. This approach allows the direct computations of noise propagation from complex sources, which are not constructed from simple sources, such as a propeller, once its noise signature is known at specific points.
The use of the *hard source* has some limitations. The first is related to the frequency of the source; a phase delay is observed with increasing the frequency of the source. This is mainly observed at tens kilo-Hertz frequency, which is outside the range of application of underwater source. To overcome this problem, a solution is to impose the correct pressure in multiple clustered points [6]. The *hard source* since is a Dirichlet boundary condition, acts as a barrier; therefore the energy incident to the source nodes is reflected. This could lead to an overestimation or underestimation of acoustic pressure when the source is positioned near a reflecting wall. The need to overcome this underside effects lead to the implementation of the *soft source* and the *transparent source*. Moreover, we present also the *hard image source*, which is introduced here for the first time, which can be apply to specific case to reduce the underside effects of the *hard source*.
The simpler method to avoid the spurious reflection of the cis the *soft source* method. The source function S, is then considered in the wave equation (2.1), and updated at each time step. This method allows avoiding the numerical errors of the *hard source* implementation because the incoming waves can pass through the source and interfere with it since in this method the wave equation is solved in the source node(s). The problem is that the pressure evaluated at the source location differs from the prescribed amplitude. The correct response of the source is obtained if the results are normalized. The knowledge of analytical functions describing the propagation of acoustic sources resolves the normalization

problem. However, for real-world applications, where analytical functions are not available, the normalization process is not straightforward, hindering the use of this approach. This method has additional limitations when considering finite size sources because, in this case, the acoustic pressure must be prescribed at all grid points, even if they are contained within the source, posing additional constraints to its use in real-world applications.
A second implementation is the *transparent source*, developed ([62]), which is able to eliminate the scattering property of the hard source, making the source transparent to incoming waves. The applicability of this method is limited to line source and point sources, making it not suited for multiple clustered points and, moreover, it requires higher computational cost since two numerical simulations are required to obtain the solution.
The *hard image source*, here presented, can be used when analytical function are available or when the values of the acoustic pressure due to the reflection from a nearby boundary are known at the source. In the presence of a free surface in the propagation domain, the use of the image method can mitigate the effects of the reflection of the acoustic waves incident to the *hard source*. The knowledge of the reflected waves onto the source nodes enables the addition of this component to the already imposed source pressure. The value of pressure of the *hard image source* are evaluated as follows:

$$p_{hard\,image}(r,t) = \hat{p}_{hard}(r,t) + \hat{p}_{img}(r_{img},t)\mathcal{H}(t - r_{img}/c), \tag{2.4}$$

where $\hat{p}_{img}$ is the $\hat{p}_{hard}$ function evaluated at r_{img}, which is the distance between the source and its image. The Heaviside function acts as a delay activating the image source only upon the arrival of the first reflected wave.

2.3.4 Layout of the Numerical Implementation

Know that we have presented all the single steps needed to solve the acoustic wave equation, we give the overall layout of the numerical method:

1. Initialization: The physical $(p_i^n, p_i^{n-1}, p_i^{n-2})$ and auxiliary $(\psi_i^n, \phi_i^n, \psi_i^{n-1}, \phi_i^{n-1})$ fields are initialized at zero. The field variables, ρ_i, c_i, are initialized so as to map the ocean environment, and σ_i is initialized to be 0 in the real region and 1 in the PML regions.

2. Time Loop: The following time loop is repetend n times until final time T is reached.

   - Acoustic Pressure: The value of p_i^n is evaluated from Eq.2.3 at locations i of the numerical domain. Note that the 3D version of Eq.2.3 has i, j, k indexes for space location, and the Laplacian term also contains the derivatives in the other two directions.

   - Source: The source term is imposed at the source location as a time-varying Dirichlet boundary condition, $p_i^n = p(x,t)$, where the imposed values are evaluated from the know analytical function at the position $x = i\Delta x$ of the numerical grid and at the time $t = n\Delta t$.

- PML: The value of ψ_i^n, ϕ_i^n are evaluated from Eq.2.3. Note that in the 3D space, four additional equations are solved since four auxiliary variables are added, two for each direction. The methodology is explained in detail in [11].

- Boundary Condition: All the boundary conditions are applied.

- Final Step: All the physical and auxiliary fields are updated, $p^{n-1} = p^n$, $p^{n-2} = p^{n-1}$, $\psi^{n-1} = \psi^n$, $\psi^{n-1} = \psi^n$

3. Data Collection: The dataset is stored for successive post-processing and analysis.

The main limitation of this numerical code is the memory requirement. Indeed, the physical and auxiliary fields must be known in all the domains, and refining or increasing the size of the numerical domain increases the memory requirement. In terms of execution, the explicit method is relatively fast compared to implicit methods and allows using a very large grid. The biggest numerical grid utilized in this work was on the order of 400M cells. The parallelization of the code is obtained with the OpenMP paradigm. In particular, evaluating the Laplacian term is the most consuming part of the execution. The OpenMP paradigm allows the distribution of the execution of the Laplacian term over multiple cores. Better results can be achieved using the MPI parallelization paradigm, but it was out of the scope of this work.

Chapter 3

Propagation of acoustic waves generated from complex sources in a marine waveguide

The propagation model based on the acoustic wave equation and introduced in 2.3 is validated in two distinct parts. In the first part 3.1, we considered a semi-infinite marine environment bounded just from above by a free surface and infinite along the horizontal and towards the bottom. In the second part 3.2, we compared the numerical and analytical solutions obtained with the Helmholtz equation in two classical waveguides: the ideal and Pekeris waveguides. Then, in section 3.3, we evaluate the effects on the acoustic field due to the directivity pattern of the acoustic sources in the Pekeris waveguide. This is of fundamental importance since most anthropogenic sources are not assimilable to an omnidirectional source, at least in the near acoustic field.

3.1 Validation of the acoustic wave propagation model in a semi-infinite domain

In this section, we describe the validation of the propagation model using three different sources, namely monopole, dipole, and quadrupole. These three sources are relevant for the underwater noise propagation problem because they, or a composition of them, represent archetypal models of real noise sources present at sea, like, among the others, ship propellers and hydrokinetic turbines. The dipole and the quadrupole exhibit directivity patterns and allow the evaluation of the directivity effect in a marine environment. In Figure 3.1 we report a schematic of the sources used in this section, considering the presence of a free surface.
In our numerical validitation, the marine environment is represented as a semi-infinite homogeneous water domain bounded by a top free surface. This simplification allows the use of the image method to obtain an analytical solution of the problem. An image source

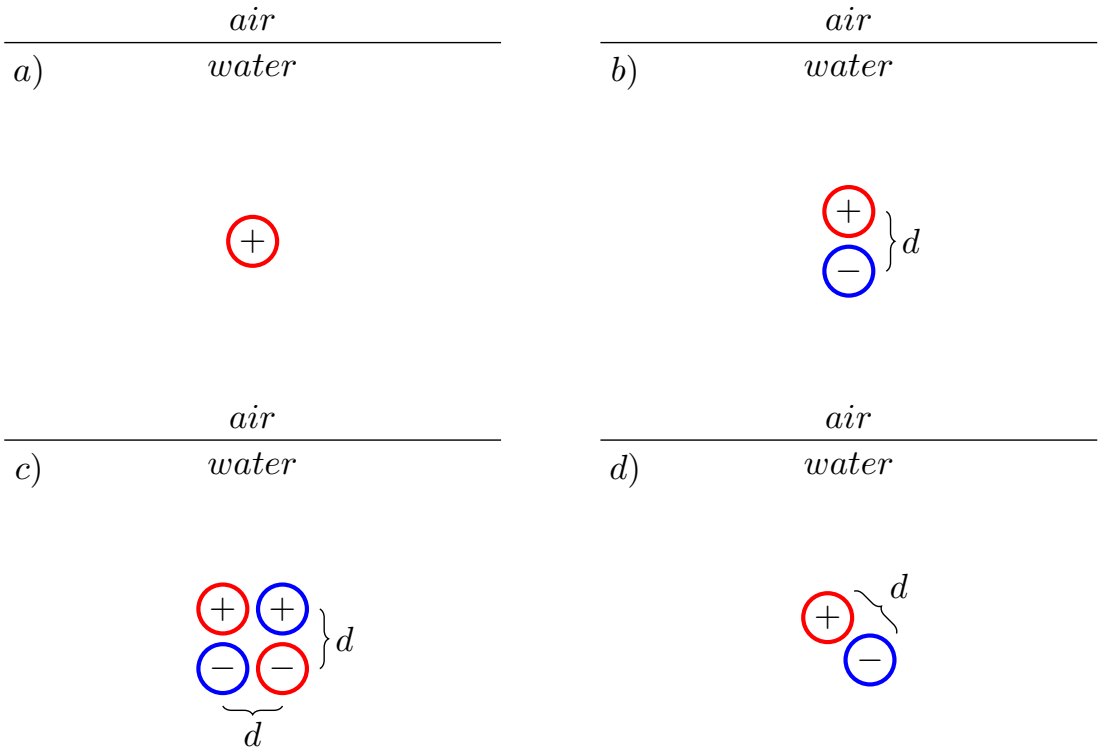

Figure 3.1: Schematic of the sources used in this study: *a*) monopole; *b*) dipole; *c*) quadrupole; *d*) 45° inclined dipole.

is placed by the opposite side with respect to the free surface so that the result inside the real domain is the sum of the acoustic pressure generated by the real source and by the image source. The sign of the image source is opposite to that of the real source so as to verify the condition $p = 0$ at the free surface [59]. Hereafter the speed of sound is $c = 1500\,\mathrm{m\,s^{-1}}$ and the water density is $\rho = 1000\,\mathrm{kg\,m^{-3}}$. The frequency of the source is set to f_{20} =20 Hz and f_{100} =100 Hz respectively giving wavelengths $\lambda_{20} = 75\,\mathrm{m}$ and $\lambda_{100} = 15\,\mathrm{m}$, respectively. The wavelength associated to the source λ_f (f stands for the frequency of the source), is used to make the length non dimensional. Hereafter, the symbol $(\tilde{\cdot})$ defines non dimensional quantities. As a consequence the grid spacing of 1 m gives $\tilde{\Delta}x_{20} = 0.013$ and $\tilde{\Delta}x_{100} = 0.066$ respectively for the two frequencies. The numerical domain is $600m$ ($8\lambda_{20}$ and $40\lambda_{100}$) long in the x-direction, $200m$ ($2.66\lambda_{20}$ and $13.33\lambda_{100}$) deep in the z-direction, and 100 m ($1.33\lambda_{20}$ and $6.66\lambda_{100}$) large in the y-direction. Open-boundary conditions are imposed over all directions but the top surface, in order to mimic a semi-infinite column of water bounded from above. The numerical grid satisfies requirement about the minimum number of points per wavelength, and the overall dimension of the domain is within the value suggested in [19] to minimize the dispersion error.
The sound power radiated by these sources changes from case to case. At the same fre-

quency, the quadrupole and dipole do not radiate the same energy as the monopole. Thus, the sound power radiated by the dipole and quadrupole is normalized with respect to the sound power radiated by a monopole in a uniform homogenous domain. A careful derivation of the sound power radiated by the sources presented in the next section, is described in Norton [50].

3.1.1 Monopole

The simpler archetypal source is the monopole. It exhibits a spherical directivity and the acoustic waves are a function of the radius distance r only. The function describing the acoustic pressure generated by a monopole $p_m(r,t)$ is:

$$p_m(r,t) = -\frac{ik\rho c Q_m}{4\pi r} e^{i(\omega t - kr)}, \tag{3.1}$$

where r is the distance from the origin of the monopole, t is time, Q_m is the source strength, $\omega = 2\pi f$ is the angular frequency, and $k = 2\pi/\lambda$ is the wavenumber. The relation between the angular frequency and the wavelength is regulated by the speed of sound of the medium $c = \omega/k$. The sound power radiated by the monopole Π_m in an infinite domain, is:

$$\Pi_m = \frac{Q_m^2 \rho c k^2}{8\pi}. \tag{3.2}$$

The sound power radiated is obtained integrating the acoustic intensity over a surface area which is perpendicular to the acoustic intensity. This relation is valid only in the far-field, where the pressure and the particle velocity are in phase ($kr >> 1$) [50]. It is used as a reference quantity to normalize the source strength of the dipole and quadrupole, after imposing $Q_m = 1$.
In Figure 3.2, the directivity of the monopole is shown over a plane passing trough the source, and the waves propagates in an infinite homogenous domain. A monotonic decreasing of the acoustic pressure is observed with the distance r from the center, where the monopole is placed. The spherical symmetry of the monopole is evident from the observation of the Sound Pressure Level (SPL), which is evaluated as follows:

$$SPL = 20 \log_{10} \left(p_{rms}/p_0 \right), \tag{3.3}$$

where p_{rms} is the root-mean-square of the pressure, and p_0 is the reference pressure, which for an underwater acoustic environment is $p_0 = 10^{-6}$ Pa. The SPL is used to evaluate the acoustic level in space; therefore, it is useful to understand the distribution of acoustic energy in space.
In the validation case, the monopole source is located $36.5m$ ($0.48\lambda_{20}$ and $2.4\lambda_{100}$) below the free surface at the center of the computational cell (Figure 3.1 *a*); it is used to estimate the error of our propagation model, using the *hard source* and the *hard img source* method when comparing with the analytical solution. The free surface lies in the near field of the 20 Hz source and in the far-field for the 100 Hz one. In Figure 3.3 we show the SPL

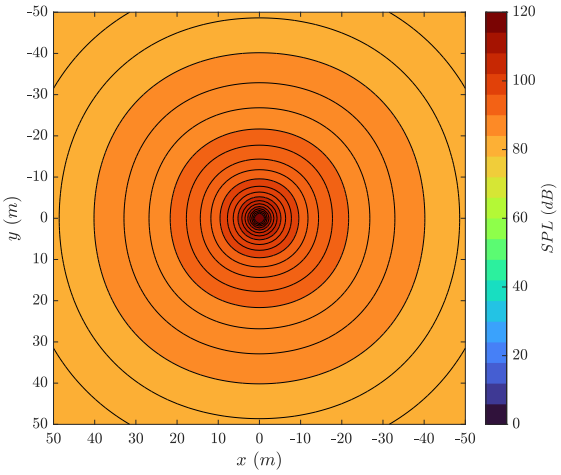

Figure 3.2: Directivity plot of a monopole with a frequency of 20 Hz in a infinite homogeneous water domain.

generated by the source on the $x-z$ plane passing through the source for both frequencies. In panel a, the 20 Hz source is in the near field, and significant interference pattern is not observed. In panel b of Figure 3.3, for the 100 Hz source, the interference pattern is observed. It appears in the shape of divergent ribbons of pressure originated in the region between the source and the free surface. The interaction between the source and the free surface leads to the observation of minima and maxima of the SPL. This is known as the Lloyd Mirror effect [67]. To be noted that, since the source has spherical symmetry, the solution is axial-symmetric as the planes of Figure 3.3 are representative of the solution as a whole.

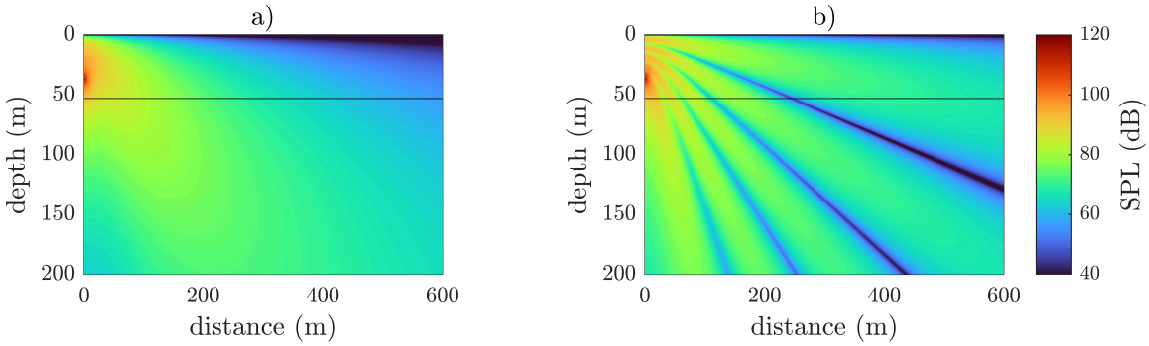

Figure 3.3: SPL on the x-z plane passing through the monopole source: a) $f_{20} = 20$ Hz; b) $f_{100} = 100$ Hz.

In Figure 3.4, we show the comparison between the numerical results and the analytical solution; the pressure signal is sampled along the black line sketched in Figure 3.3 at a depth

of $z = 52m$. The numerical results are labeled Hard and Hard Img respectively based on the method used for the implementation of the source. For the 100 Hz monopole source a second numerical experiment is conducted with a refined grid, and the case is label Hard Refi, since the *hard source* method is used. In this case, the distance between two vertices is halved compared to the other cases in the three directions ($\Delta x_i = 0.5\,\text{m} = 0.033\lambda_{100}$).

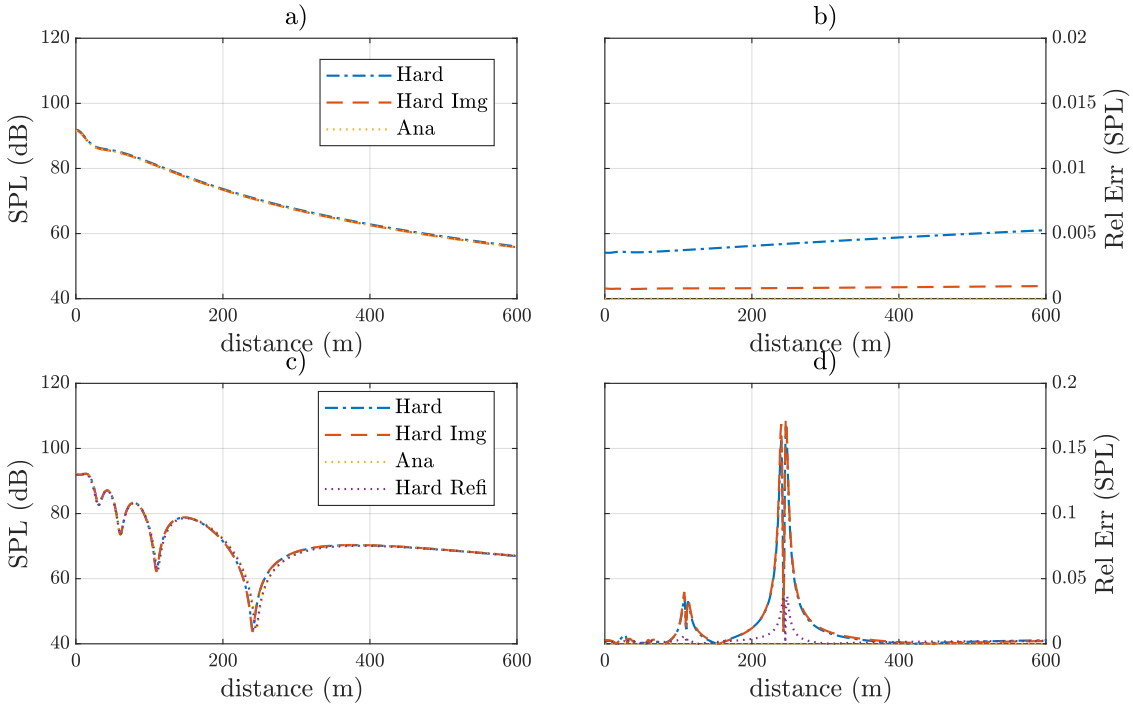

Figure 3.4: Error analysis of the quadrupole source along a line at a depth of 52 m: *a*) SPL of the 20 Hz source; *b*) relative error of the 20 Hz source; *c*) SPL of the 100 Hz source; *d*) relative error of the 100 Hz source.

In Figure 3.4 panel *a*, we observe a monotonic behavior for the SPL. The source and the free surface do not generate an interference pattern since the source is located on the near field of the free surface compared to the f_{100} monopole (Figure 3.4 panel *c*), where a non-monotonic behavior is observed, reflecting the ribbon-like structure of the acoustic field.
In Figure 3.4 panel *b* and *d* we show the relative error, which is evaluated as:

$$RelativeError = \frac{|SPL_{numerical} - SPL_{analytical}|}{SPL_{analytical}}$$

In the Hard case, the relative error increases with the distance from the source. Conversely, for the Hard Img case, we obtain better results. The relative error is almost constant along the line. For both cases the relative error is confined within 0.6%. The *hard img source*

method gives better results because it directly takes in consideration the effect of the free surface on the source.
In Figure 3.4 panel *d*, the relative error of the f_{100} monopole is higher than the f_{20} monopole. However, the maximum relative error of 15% is limited and confined where the SPL reaches the minimum. For the Hard and Hard Img cases the minimum value of the SPL is still correctly obtained, and, the error is mainly associated to a small shift of the curves due to a weak dispersion feature, and, away from the minima, the relative error is bounded below 4%.
The higher error of the f_{100} monopole is related to numerical dispersion, the dependency of the speed of sound on the frequency. Indeed, the numerical scheme herein employed is such that higher frequencies travel slower [19]. Consequently, the distance at which the minimum of SPL occurs for the numerical simulation is shorter than for the analytical solution. The refinement of the grid reduces the error associated with the numerical dispersion. The distance at which the minimum of the SPL occurs is evaluated correctly as observed for the Hard Refi case, and in this case the relative error is below 4% along the line.
To summarize, the *hard source* implementation corrected with the *hard img source* method is found to improve the results. However, it has to be noted that this method might fail under certain conditions in the presence of density variation along the fluid column since the correction relies on the image method, which is based on the assumption of propagation in a semi-infinite homogeneous field. Specifically, the density and speed of sound variation along the fluid column are the main limiting factor. However, if this variation occurs at a distance larger than that of the source from the free surface the *hard img source* method still gives accurate results because the image solution implemented over the boundary nodes is not affected by inhomogeneities in the field.

3.1.2 Dipole

The second archetypal source considered is the dipole which is constitued of two monopole in close vicinity of each other. The two monopole have the same source strength Q_d and oscillates in opposite phase. With this arrangement the acoustic pressure is function of both the distance radius r and the azimuth angle θ. The directivity of the dipole is characterized by two lobes and a zero sound pressure plane placed in between of the two monopoles as observed in Figure3.5. The SPL has been evaluated in infinite homogenous domain. The function describing the acoustic pressure generated by a dipole is $p_d(r,t)$ is:

$$p_d(r,t) = \frac{ik\rho cQ_d}{4\pi r_1} e^{i(\omega t - kr_1)} - \frac{ik\rho cQ_d}{4\pi r_2} e^{i(\omega t - kr_2)}, \tag{3.4}$$

where r_1, r_2 is the distance from the origin of the two monopole which are considered at a distance of d as portrayed in Figure 3.1 *b*). The minus sign derives due to the opposite phase of the monopole. The sound power radiated by the dipole Π_d in an infinite domain, is:

$$\Pi_d = \frac{Q_d^2 \rho c k^4 (d/2)^2}{6\pi}. \tag{3.5}$$

Since k is usually $<< 1$, the dipole is less efficient than the monopole in radiating energy. This is evident comparing the monopole and dipole sound power formula and assuming the same source strength. The source strength of the dipole Q_d is calculated setting its own sound power equal to that of a monopole with source strength $Q_m = 4\pi/\rho ck$, and d =0.4 m, obtaining the dipole source strength $Q_d \simeq 51.69\, Q_m$ for the 20 Hz source and $Q_d \simeq 10.34\, Q_m$ for the 100 Hz source respectively.

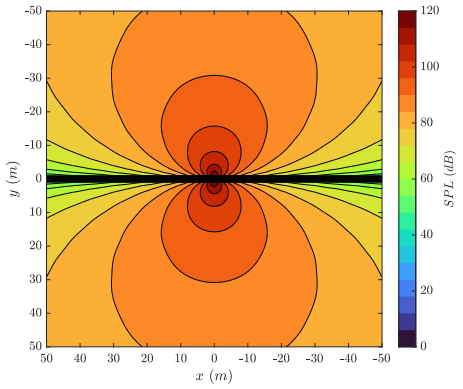

Figure 3.5: Directivity plot of a dipole with a frequency of 20 Hz in a infinite homogeneous water domain.

In the validation case, the dipole source is placed at the same depth as in the previous cases (36.5 m), and the radiated pressure field is compared with the analytical solution.
In Figure 3.6, we show the SPL of the source on the $x-z$ plane passing through the source. Panel a contains the SPL of the 20 Hz dipole. The space distribution of energy appears more complex than in the monopole case due to the directivity of the source. The SPL of the 100 Hz dipole shown in panel b is similar to the 100 Hz monopole, with a larger number of acoustic ribbons giving a larger number of planes of low pressure level. Also, the near field distribution of the acoustic pressure appears more complex than in the monopole case.

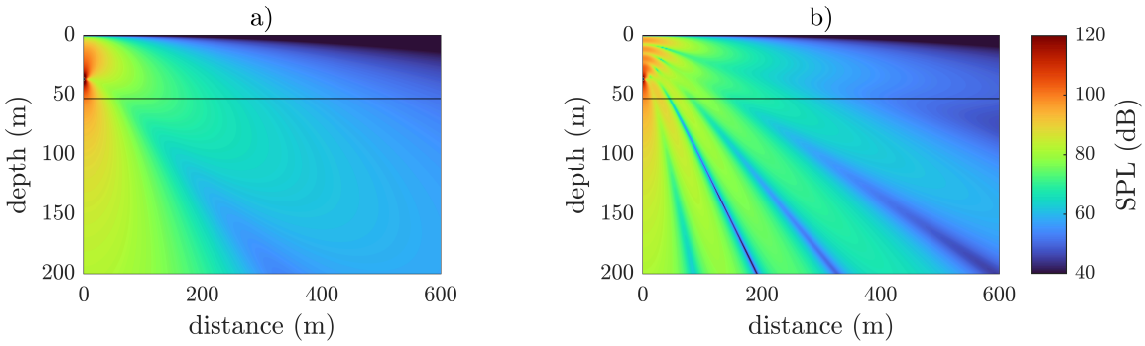

Figure 3.6: SPL on the x-z plane passing through the dipole source is shown. a) $f_{20} = 20$ Hz source; b) $f_{100} = 100$ Hz source.

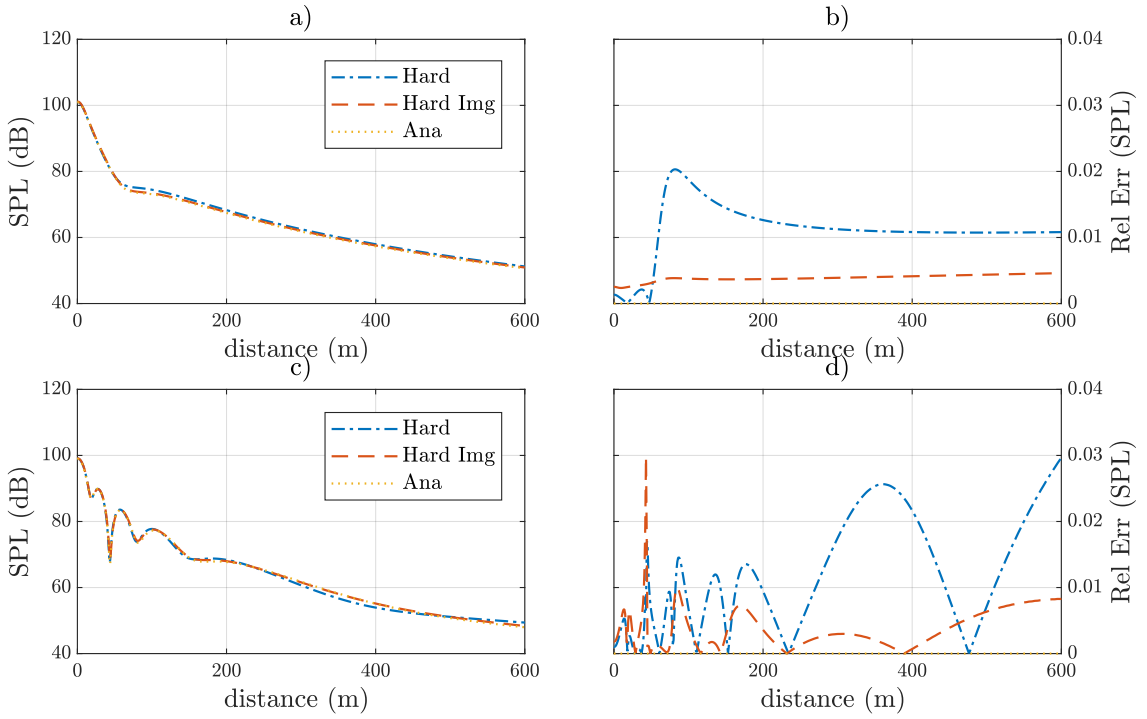

Figure 3.7: Error analysis of the dipole source along a line at a depth of 52 m: *a*) SPL of the 20 Hz source; *b*) relative error of the 20 Hz source; *c*) SPL of the 100 Hz source; *d*) relative error of the 100 Hz source.

As for the previous case, we show the comparison between the numerical and the analytical results at a depth of 52 m (Figure 3.7). In panel *a* we show the SPL profile of the 20 Hz dipole. The main difference observed compared to the monopole is the rapid decay near the source up to a local minimum. The relative error shown in panel *b* is limited to 2% for the Hard case, and it is maximum near the local minimum of SPL. The Hard Img case gives better results, and the relative error is almost constant across the domain and remains confined below the 0.5%.
In panel *c*, we show the SPL profile of the 100 Hz dipole. Compared to the monopole source, the amplitudes of the local minima are smaller, and these are clustered near the source. The dispersion error appears larger for the high frequency source, as shown in panel *d*. The relative error is limited within 3% for the Hard and Hard Img cases. The relative error of the Hard Img case is maximum at the second local minimum of the SPL profile, and then it remains nearly unchanged and below 1%. Conversely, the relative error in the Hard case increases with the distance from the source.

3.1.3 Quadrupole

The third archetypal source considered is the lateral quadrupole which is constituted of two dipole in close vicinity of each other, therefore the single monopoles that constitute the quadrupole are positioned at the vertices of a square with a side of length d as portrayed in Figure 3.1 *c*). This is know as a the lateral quadrupole. The two dipole have the same the source strength Q_q and oscillates in opposite phase. The acoustic pressure is function of both the distance radius r and the azimuth angle θ. The directivity of the quadrupole is characterized by four lobes and two zero pressure plane placed in between the four monopole as observed in Figure 3.8. The sound power radiated by the quadrupole Π_q in an infinite domain, is:

$$\Pi_q = \frac{4Q_q^2 \rho c k^6 (d/2)^4}{30\pi}. \tag{3.6}$$

To obtain the same sound power of the previous case, keeping the monopole source strength to $Q_m = 4\pi/\rho ck$, the quadrupole source strength becomes $Q_q \simeq 3348.96 Q_m$ for the 20 Hz source and $Q_q \simeq 137.96\, Q_m$ for the 100 Hz source respectively.

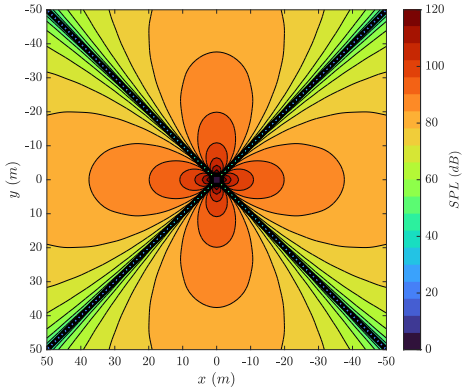

Figure 3.8: Directivity plot of a quadrupole with a frequency of 20 Hz in water.

Also in this validation case, the quadrupole source is placed at the same depth as in the previous cases (36.5 m). The radiated acoustic pressure is compared with the analytical solution. In Figure 3.9 we show the SPL of the quadrupole source on the $x-z$ plane passing through the source. In panel *a* the SPL of 20 Hz quadrupole shows that the quadrupole introduces a plane of zero sound emission perpendicular to the free surface. For the 100 Hz quadrupole the distribution of the energy is similar to that of the other sources, namely in form of divergent ribbons propagating from the region confined between the source and the free surface.

The comparison between the numerical and the analytical solutions at a depth of 52 m is shown in Figure 3.10. In panel *a* we show the SPL profile for the 20 Hz quadrupole. Compared to the dipole, we observe the presence of a minimum value of SPL in the near field. The relative error shown in panel *b* is smaller than 1.5% over the line for the Hard

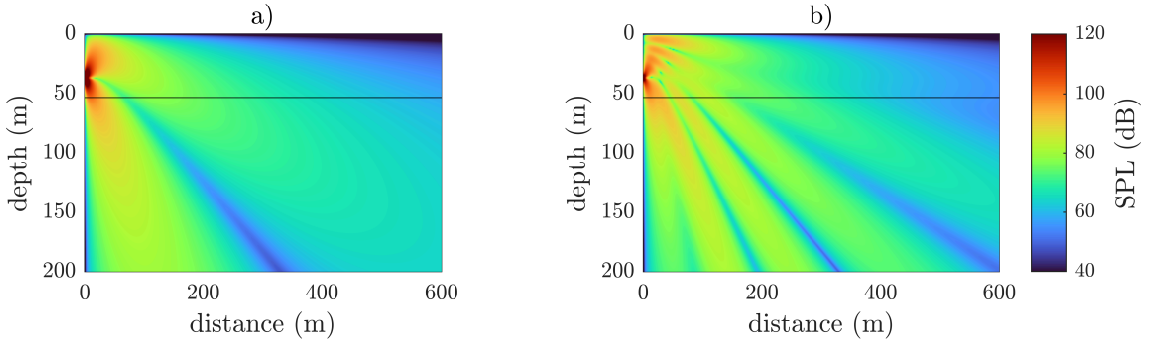

Figure 3.9: SPL on the x-z plane passing through the quadrupole source. *a*) the $f_{20} = 20\,\text{Hz}$ source; *b*) the $f_{100} = 100\,\text{Hz}$ source.

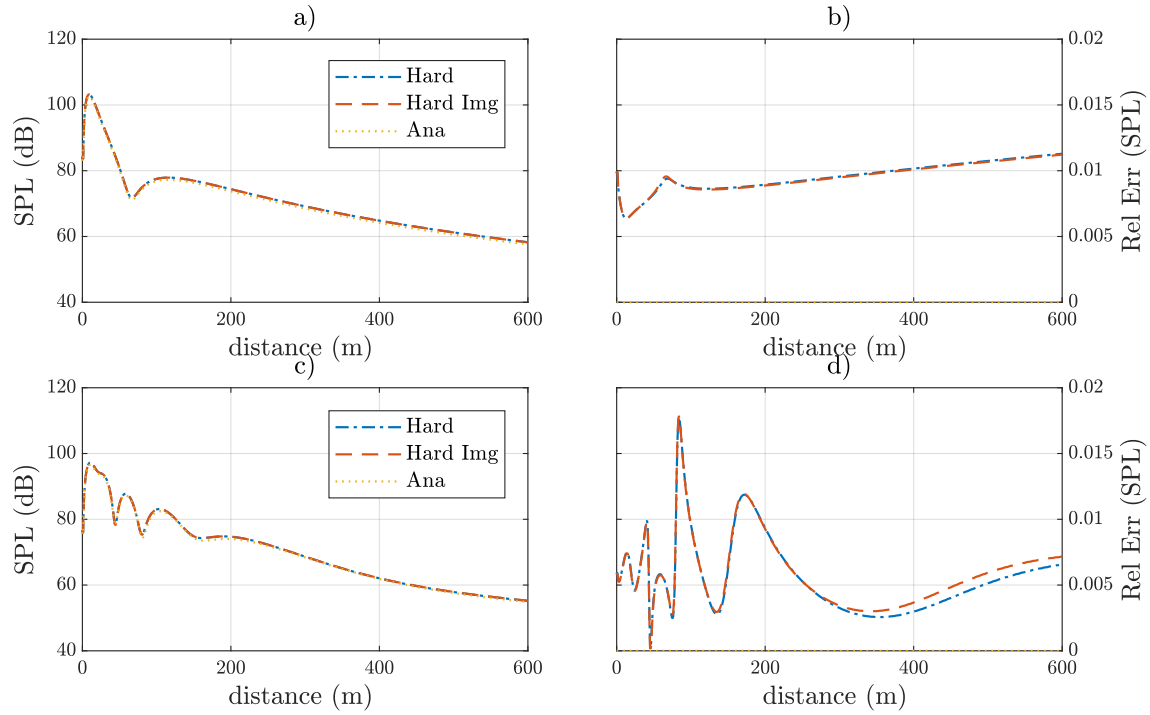

Figure 3.10: Error analysis of the quadrupole source along a line at a depth of 52 m: *a*) SPL of the 20 Hz source; *b*) relative error of the 20 Hz source; *c*) SPL of the 100 Hz source; *d*) relative error of the 100 Hz source.

and the Hard Im cases. Increasing the frequency increases the number of local minima of the SPL (panel *c*). The relative error (panel *d*), does not increase significantly with the frequency. Overall, for the Hard and Hard Img cases, the error is smaller than 2%, and the latter gives better results near the source. As for the previous sources, the error is mostly

associated with a slight spatial shift of the signal due to the mentioned dispersion error.
As a conclusion of the Section 3.1, the analysis shows that the direct solution of the wave equation using an overall second-order accurate numerical scheme provides accurate results for a number of different sources, in a wide range of frequencies and for distances of the order of $40\,\lambda$, where λ is the wavelength of the source. The limiting factor for a second-order scheme is the minimum point per wave length required to solve the acoustic signal. Our results show that the dispersion error remains marginal at least up to 40 wave lengths, and it is expected to remain very small even for larger domains. The multipole sources have been constructed from simple monopole sources for simplicity and a more straightforward approach to normalizing the sound power emitted by these sources. Analytical expressions for higher order singularities are available in the literature. We have also tested the propagation model using these analytical expressions, and since the results are comparable to those for multiple monopoles, we have decided to show only these results.

3.2 Validation of the acoustic wave propagation model in classical waveguide

In the present Section we consider the propagation of an acoustic signal in two classical waveguides, the Ideal one and the Pekeris one, both representing a simplification of the marine environment. The two waveguides are standard benchmarks for the evaluation of the performance of propagation model. More benchmarks are described in [36]. Most of them are relative to the propagation over long distances and are not of interest in the present work. I n addition, these cases investigate the interaction between an omnidirectional source and a range-dependent environment, where the depth of the waveguide changes with the distance from the source.
Further, we consider the acoustic response of the Pekeris waveguide considering the different sources discussed in the previous Section. Compared to the monopole's spherical symmetry, the introduction of a complex directivity pattern enables multiple configurations with respect to the free surface. An axis of zero sound emission characterizes the SPL generated by a dipole. This axis can be either aligned or inclined with respect to the free surface, generating a change of the acoustic energy distribution inside the waveguide. This aspect is analyzed in section 3.3.1.
The first benchmark problem is the Ideal waveguide. The waveguide is range-independent, it extends at the infinite over the horizontal directions, and is bounded by two planes where the pressure is set to zero. The numerical domain used to reproduce the benchmark is shown in Figure 3.11, panel *a*. The density of the fluid is $\rho = 1000\,\mathrm{kg\,m^{-3}}$ and the speed of sound is $c_0 = 1500\,\mathrm{m\,s^{-1}}$.
The second benchmark problem is the Pekeris waveguide. It is range-independent and extends at the infinite in the horizontal direction. Along the vertical, the homogenous fluid layer is bounded from above by the free surface and below by an infinite layer of sediment. The numerical domain used to reproduce the benchmark is shown in Figure 3.11, panel *b*. The density of the fluid is $\rho = 1000\,\mathrm{kg\,m^{-3}}$ and the speed of sound is

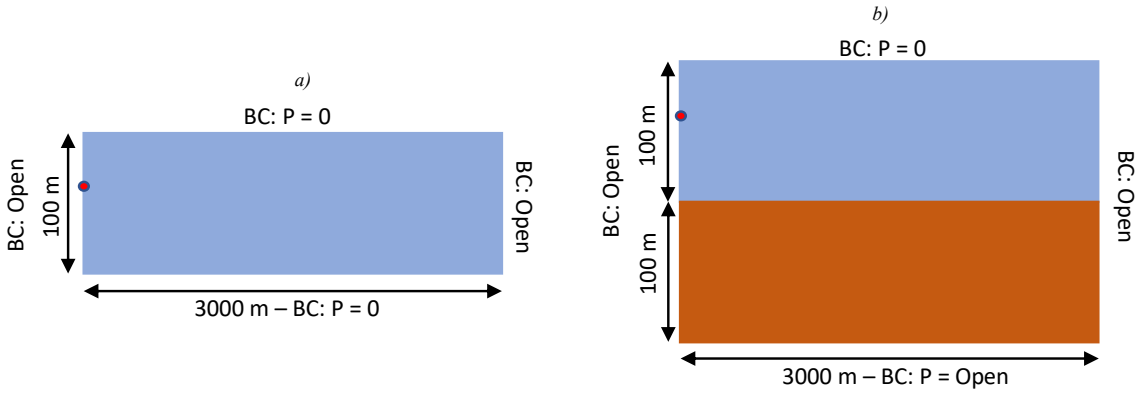

Figure 3.11: Schematic of the waveguides: *a*) Ideal waveguide; *b*) Pekeris waveguide.

c_0 =1500 m s^{-1}. The sediment has a density of $\rho_{sediment}$ = 1800 kg m^{-3} and the speed of sound is $c_{sediment}$ = 1800 m s^{-1}.

3.2.1 Ideal Waveguide

A continuous 20 Hz monopole source is placed 36 m below the free surface in the Ideal waveguide (Figure 3.11 *a*). The source function $p(t)$, imposed as *hard source* on a single node, is:

$$p(t) = \sqrt{2}\sin(2\pi f t), \tag{3.7}$$

where f is the frequency of the source, t is time, and $\sqrt{2}$ is an amplitude factor. The source is omnidirectional like the monopole, but with a finite amplitude at the origin. The pressure values used to obtain the results are collected in the time window T-3T, where T is defined as the time needed by the acoustic pressure to reach the farthest computational boundary along an horizontal line. In the simulation, this distance is equal to L_x, and $T = L_x/c$, where c is the slowest speed of sound in the domain when different media are present. This approach is needed to allow the simulation to reach a statistically steady state. The numerical grid is uniform in all directions, and the grid cells dimension is 1 m, which normalized by the wavelength is 0.013; the largest horizontal extension of the numerical domain is 40 wave lengths. In Figure 3.12 we show the numerical and the analytical results of the Transmission Loss (TL) of the monopole source in the ideal waveguide.
The TL, defined in [37], is:

$$TL(\boldsymbol{r}, \boldsymbol{r}_s) = -10\log_{10}\left(\frac{Z_0(\boldsymbol{r}_s)}{Z(\boldsymbol{r}, \boldsymbol{r}_s)}\left|\frac{p(\boldsymbol{r}, \boldsymbol{r}_s)}{p_0(\boldsymbol{r}_s)}\right|^2\right), \tag{3.8}$$

where $\boldsymbol{r}$ is the distance from the source, $Z(\boldsymbol{r}) = \rho(\boldsymbol{r})c(\boldsymbol{r})$ is the acoustic impedance of the medium, and p is the acoustic pressure. The TL is obtained by dividing the acoustic pressure at a distance $\boldsymbol{r}$ by a reference pressure given by the same source at reference distance $\boldsymbol{r}_s$ =1 m in a homogenous infinite medium. In our numerical experiment the

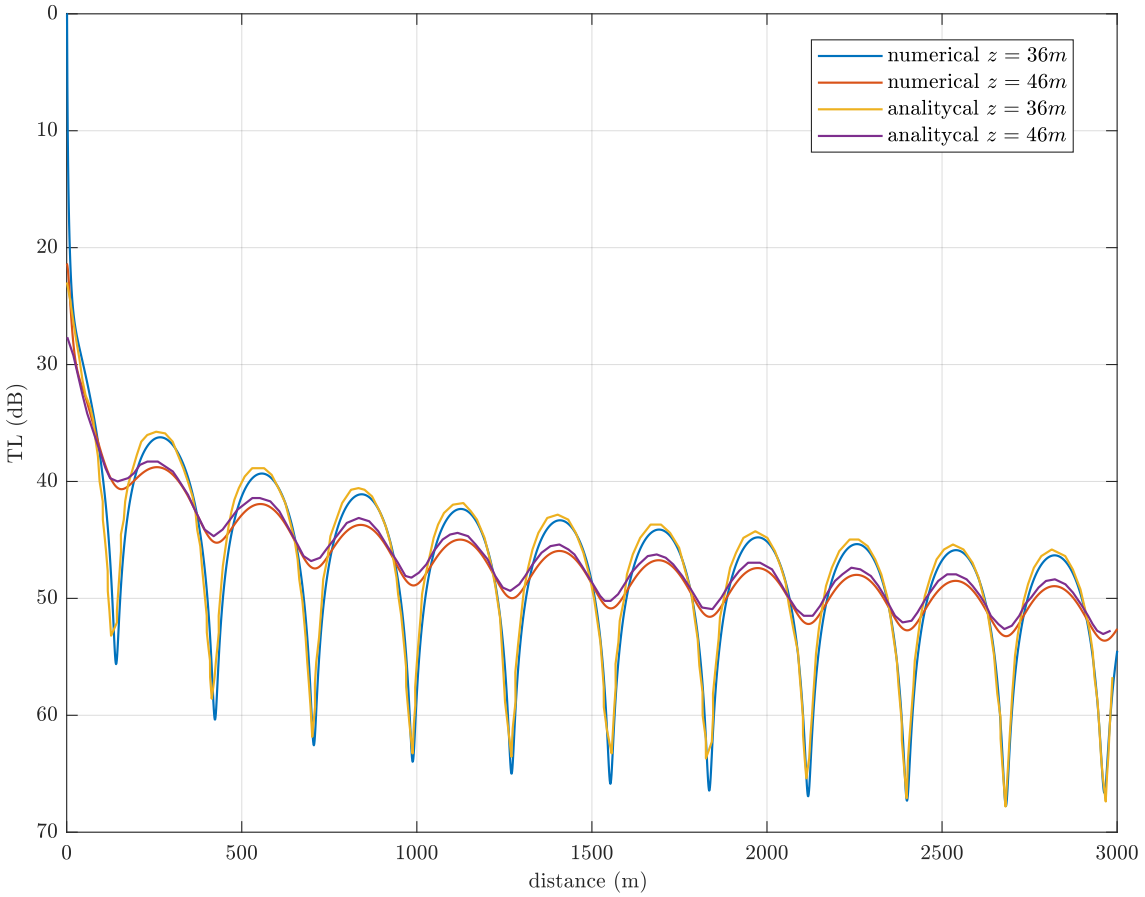

Figure 3.12: Transmission loss for a 20 Hz continuous point source placed at 36 m of depth in the Ideal waveguide. The numerical and analytical results at $z = 36$ m and at $z = 46$ m.

acoustic pressure is evaluated in the time domain, as a consequence, $p(\boldsymbol{r}, t)$ is a function of time. For this reason in Eq.(3.8) the root-mean-square pressure p_{rms} is used instead of $p(\boldsymbol{r}, \boldsymbol{r}_s)$.
The analytical results are taken directly from Figure 2.23 panel *b* of [37], where the authors solved the Helmholtz equation, using the normal-modes approach.
The results are shown at two different depths, namely at the source depth 36 m and below, at 46 m. The characteristic oscillations of the TL, which are related to the two modes propagating in the waveguide, are well-replicated at both depths. These two modes have a specific modal interference length L_i, which in this case is of $L_i \simeq 300$ m, namely $6\lambda_{20}$. The difference in the amplitude of oscillation is related to the amplitude associated with the propagating modes, as explained in more detail in [37]. At 36 m both modes are excited with the same amplitudes, and at 46 m the amplitude of the first mode is higher than that of the second mode. A spherical decay ($\sim 1/r$) is observed near the source. At a distance

equal to the depth of the domain, as expected, we observe a cylindrical decay ($\sim 1/\sqrt{r}$). There is a 1 dB to 2 dB difference at the maxima of the two TLs. However, the difference is constant across the domain so that the error might be related to the method used to extract the reference data. The difference observed at the minima is basically due to the low resolution of the analytical results, as extracted by the reference paper. Overall, the second-order numerical method implemented for the solution of the wave equation in the physical space provides accurate results.

3.2.2 Pekeris Waveguide

The second classical problem is the Pekeris waveguide, an archetypal representation of a shallow-water marine environment (Figure 3.11 *b*). The only physical boundary of the problem is the upper free surface, but the interface between the water and sediment layers entraps part of the acoustic energy inside the fluid waveguide and allows the propagation of the acoustic waves over long distances as in a real shallow water environment.
A 20 Hz monopole source is placed 36 m below the free surface and it is implemented as in the previous case using the function (Eq.3.7). The pressure values are collected in the time window $T - 3T$ following the previous approach. The numerical grid is uniform in all directions, and the grid cell dimension is 1 m, as in the previous case. In Figure 3.13 we show the numerical and the analytical results of the TL of the monopole source in the Pekeris waveguide. As in the previous case, the analytical results are taken directly from Figure 2.29 panel *b* [37]. The authors obtained the analytical results solving the Helmholtz equation using a wavenumber integration approach. The results are shown at the source depth 36 m and at 46 m. The fact that the domain is a semi-infinite layer allows the energy to leave the domain by the bottom side, propagating in the sediment layer. As a consequence, the modal interference length is different compared to the Ideal waveguide case. In this case, it is larger, and it decreases with the distance from the source. Moreover, as discussed in [37], just two modes are excited, a lossless mode, which propagates without losing energy, apart the geometrical decay, and a leaky one, which losses energy with the distance. The difference in the magnitude of the TL between the two depths is related to the amplitude at which the modes are excited. Compared to the Ideal waveguide case, the TL is larger for the Pekeris waveguide, since the energy is not constrained inside the fluid waveguide.
The comparison of the numerical and analytical results (Figure 3.13) shows a difference of the order of 1 dB away from the minima of the TL. The maximum of the error is observed near the minima of the TL. This is comparable with the error observed in Figure 3.4 panel *d*), for the monopole with a higher frequency. The error is related to the numerical dispersion, which is known to increase with the frequency and, as observed in this case, with the distance from the source. Increasing the resolution of the numerical simulation reduces the error as shown in Figure 3.4, where the refined grid is used (note that for the Pekeris waveguide we evaluated a refined-grid case also).
In the refined-grid case, the propagation of the source is evaluated on a smaller numerical domain, which is halved with respect to the standard domain, due to computational re-

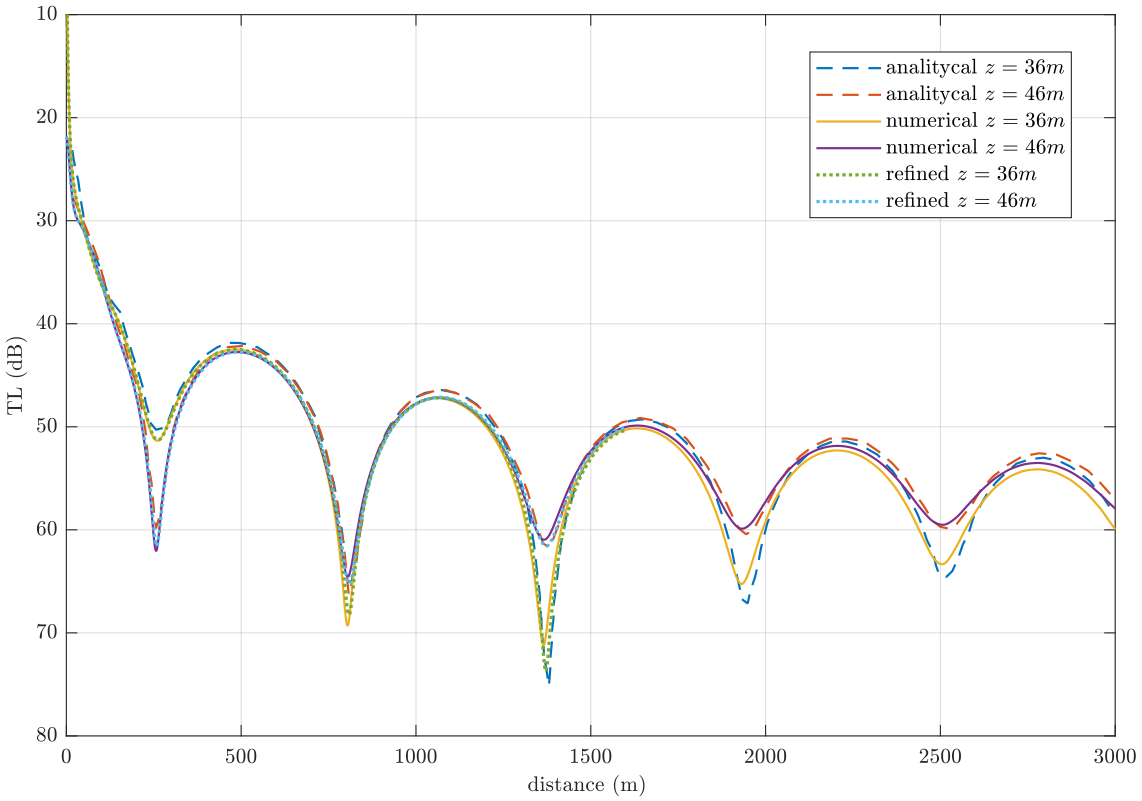

Figure 3.13: TL for a 20 Hz continuous point source placed at 36 m depth in the Pekeris waveguide. Comparison between numerical and analytical results at $z = 36$ m and at $z = 46$ m.

source limitations. The grid cells dimension in the refined case is 0.5 m, which normalized by the wavelength is 0.0066. In the refined case, the error is reduced, in that the minima and maxima of the analytical solution are better reproduced. Up to the second minimum, the two numerical simulations give similar results. On the third minimum, the refined solution follows better the behavior of the analytical solution, although the results obtained with the coarse grid still appear of good quality.
The overall behavior of the interference pattern and the range of value of the TL is correctly reproduced by the numerical simulation. The errors can be reduced by implementing a higher-order method as in Hafla et al. [30] although the second-order scheme herein presented produces accurate results.

3.3 Directivity effects on a the Pekeris waveguide

The Pekeris waveguide (Figure 3.11 *b*) is used to evaluate the propagation of the three different sources described in Section 3.1. The physical characteristics of the waveguide

and the numerical domain are the same as in the previous case, togheter with the duration in time of the simulation and the grid size. The sources have a frequency of 20 Hz and are placed at a depth of 36 m. The source strength has been chosen as described in Section 3.1. The different sources generate the same amount of energy as the monopole, although distributed with a specific directivity in space.

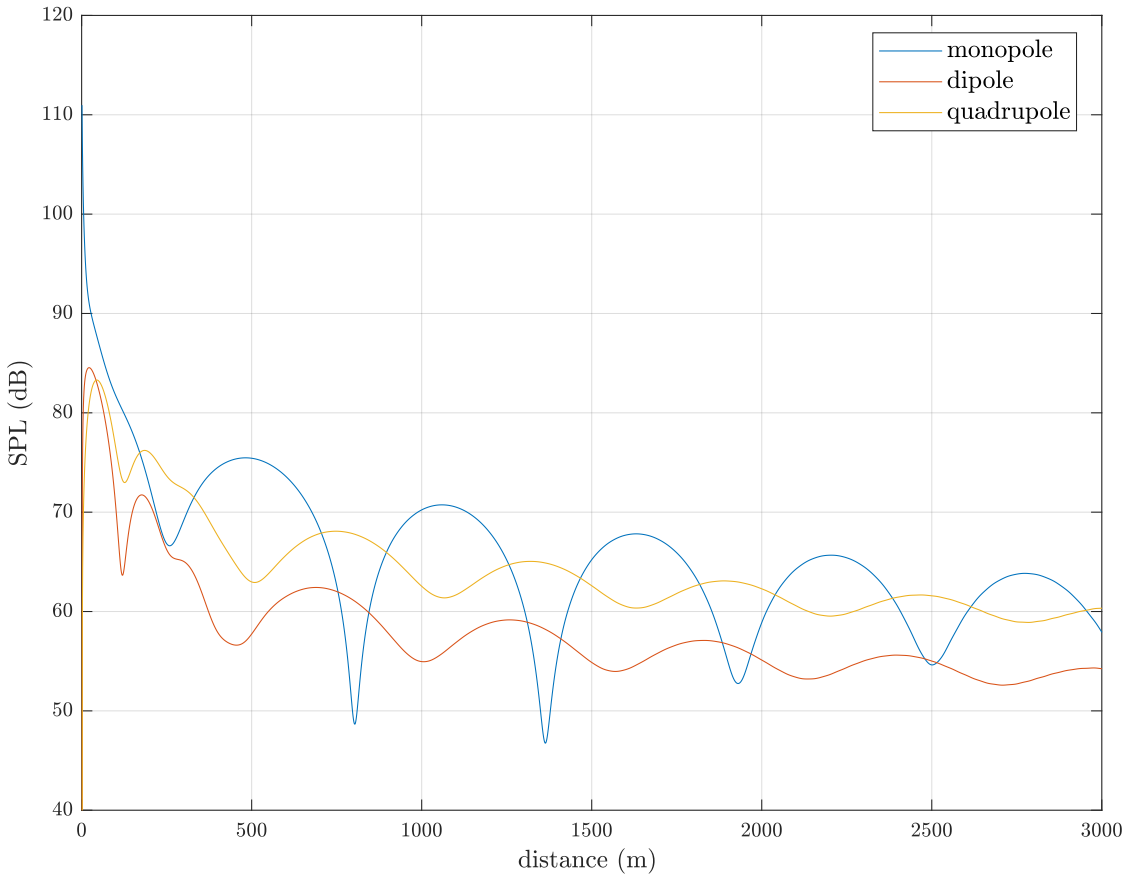

Figure 3.14: SPL comparison at a depth of $z = 36$ m between a 20 Hz continuous monopole, dipole, and quadrupole source in a Pekeris waveguide.

In Figure 3.14 the SPL of the monopole, the dipole, and the quadrupole in a Pekeris waveguide are displayed at a depth of 36 m along a line along the x-direction. The increasing complexity of the dipole and quadrupole sources contributes to significant difference in the SPL profile in the vicinity of the source up to a distance of 500 m ($6.66\,\lambda_{20}$) where multiple local minima of the SPL are observed for the dipole and quadrupole cases compared to the monopole.
At a distance larger than 500 m ($6.66\,\lambda_{20}$), the characteristic oscillatory pattern and the cylindrical decay of the SPL are recovered. The SPL amplitude of the oscillations of the monopole is about 2.5 times larger than those of the dipole and quadrupole. Among the

three sources, the dipole has the lower level of SPL across the domain; it is about 4 dB lower than that of the quadrupole and about 8 dB lower than that of the monopole.
The modal interference length is the same for the three sources, but it appears shifted by half the interference length for the quadrupole and less than half the distance for the dipole. This effect is related to the excitation of the modes inside the waveguide, which are the same described in the previous case. The amplitude at which the modes are excited depends on the source's depth and the type. As observed, the monopole at a depth of 36 m excites both modes with similar amplitude. Conversely, at the same depth the dipole and quadrupole excite the first (lossless) mode more than the second (leaking) mode as shown in Figure 3.15. (details on these aspects are in the book of [37].)

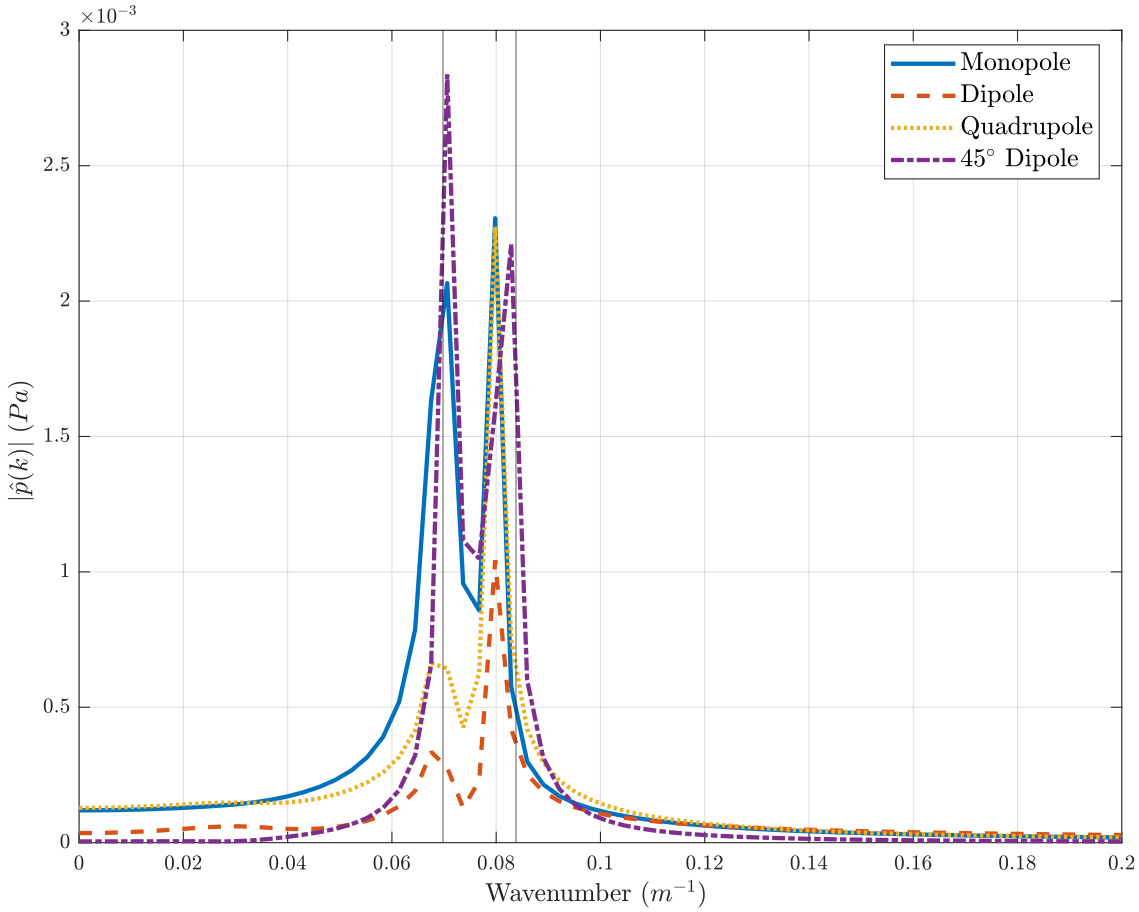

Figure 3.15: Pressure amplitude $\hat{p}(k)$ of the Fourier Transform of the pressure field along the x-direction from 300 m to 2348 m at a depth $z = 36$ m for the four sources considered in the Pekeris waveguide. The two vertical lines correspond to $k = \omega/c_{sediment}$ and $k = \omega/c_{water}$.

The difference in the SPL is a direct consequence of the directivity. Only the monopole can propagate the same energy in every $x - z$ plane passing through the source, in opposition

to the dipole and quadrupole sources.
In Figure 3.16 we show the SPL over the vertical $x-z$ plane passing through the source. The presence of the sediment layer substantially changes the energy distribution inside the fluid waveguide, compared to the case discussed in Section 3.1. The typical Lloyd pattern is not observable in this case. The monopole (Figure 3.16 *a*) is able to better transmit energy inside the fluid waveguide compared to the other two sources. The dipole (Figure 3.16 *b*) transmits most of energy in the direction perpendicular to the free surface; consequently, most of the energy leaves the fluid domain, entering the sediment layer. The presence of a zero plane of sound emission perpendicular to the free surface for the quadrupole source (Figure 3.16 *c*) constrains energy over a specific directions, and, as a consequence, more energy is propagated inside the fluid waveguide, compared to the dipole case.
The dipole maintains an axial-symmetry over the x-y plane, as shown in Figure 3.17 panel *b*). Along this plane, the distribution of energy is similar to the monopole (Figure 3.17 *a*). The quadrupole breaks the spherical symmetry over the $x-y$ plane, as shown in Figure 3.17, panel *c*. Only a quadrant of the $x-y$ plane is shown due to the symmetry properties of the solution. The $y-z$ plane passing through the source, which is not shown, is identical for the monopole and dipole sources due to symmetry. The zero plane of the quadrupole is on the $y-z$ direction (Figure 3.16 panel *c*) and it is not shown.
The monopole source, or, in general, the spherical symmetric source, is the typical type of source used to investigate the acoustic response of a marine environment due to its simplicity. The behavior of a more complex source far from the origin is somewhat similar to a monopole and, at a first approximation, it can be used as a reference. However, the SPL can be significantly different. Also, our results show that the monopole-like approximation is not valid in the near field, when the analysis of sound generated by complex sources is required.

3.3.1 Effects of the inclination of a dipole source in Pekeris waveguide

Finally, we consider the same Pekeris waveguide (Figure 3.11 *b*) used in the previous cases to evaluate the propagation of the acoustic pressure generated by the same dipole of the previous Section but inclined by 45 degrees with respect to the free surface (Figure 3.1 *d*). The main aim is to analyze the effect of a variation of the geometrical configuration of the source which exhibits a directivity on the noise propagated in the medium. We compare the results of this additional case study with those of the horizontal dipole discussed in the previous Section. The inclined dipole is placed at a depth of 36 m as the horizontal one. The physical characteristics of the waveguide and the numerical domain are the same as in the previous case, together with the time of the simulation and the grid dimension. In Figure 3.18 we show the SPL level over an horizontal line at a depth of 36 m. The SPL is significantly affected by the inclination of the source. In the near field, up to a distance of 500 m ($6.66\,\lambda_{20}$), the decay of the signal is substantially different between the two cases. Specifically, the inclined dipole resembles the monopole, with a decay typical of a source exhibiting radial symmetry along this plane. (compare Figure 3.18 with Figure 3.14) Further, at intermediate distances (larger than 500 m, $6.66\,\lambda_{20}$) the signals appear

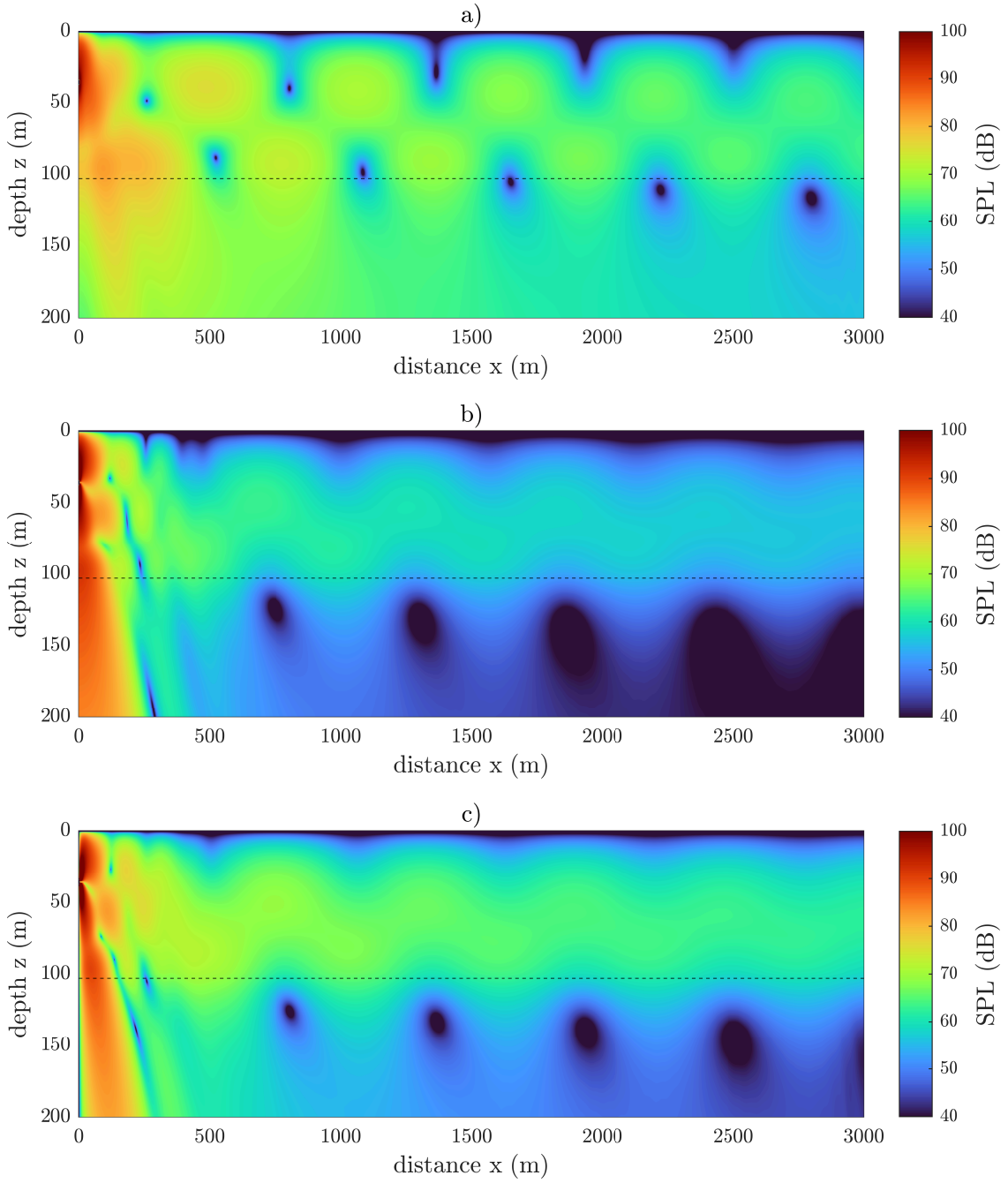

Figure 3.16: SPL over the vertical $x - z$ plane at a depth of $z = 36\,\mathrm{m}$: a) 20 Hz monopole; b) dipole; c) quadrupole.

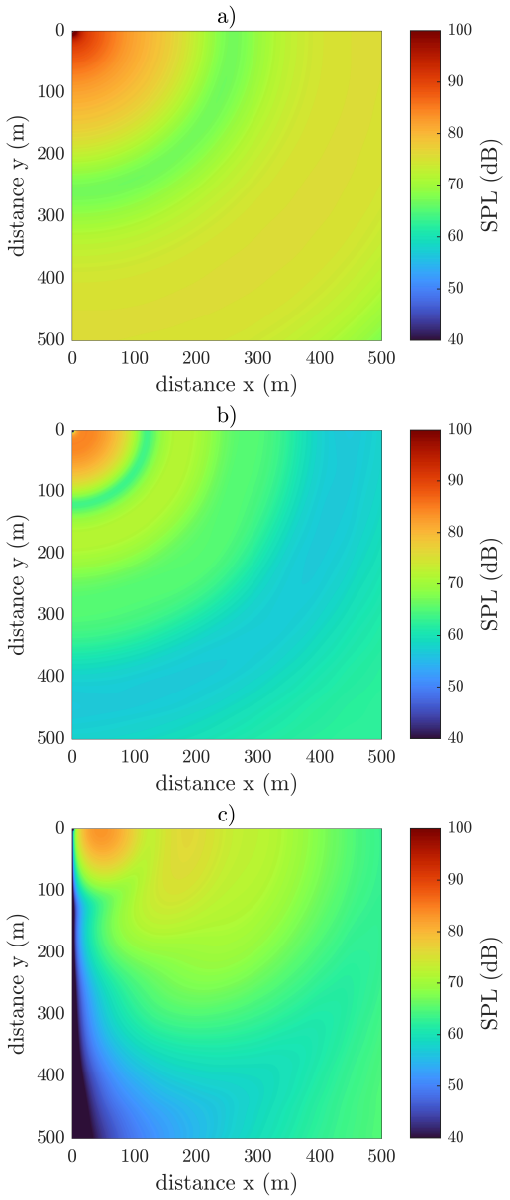

Figure 3.17: SPL on a quadrant of the $x - y$ plane at a depth of $z = 36\,\mathrm{m}$; a) 20 Hz monopole; b) dipole; c) quadrupole.

different in shape and amplitude. The inclined dipole SPL profile resembles that of the monopole (compare Figure 3.14). Specifically, the amplitude of the oscillations of the SPL is nearly doubled with respect to that of the horizontal dipole and more similar to that of the monopole. This is due to the fact that the orientation of the source may dramatically affect the amplitudes at which the modes are excited. In particular in Figure

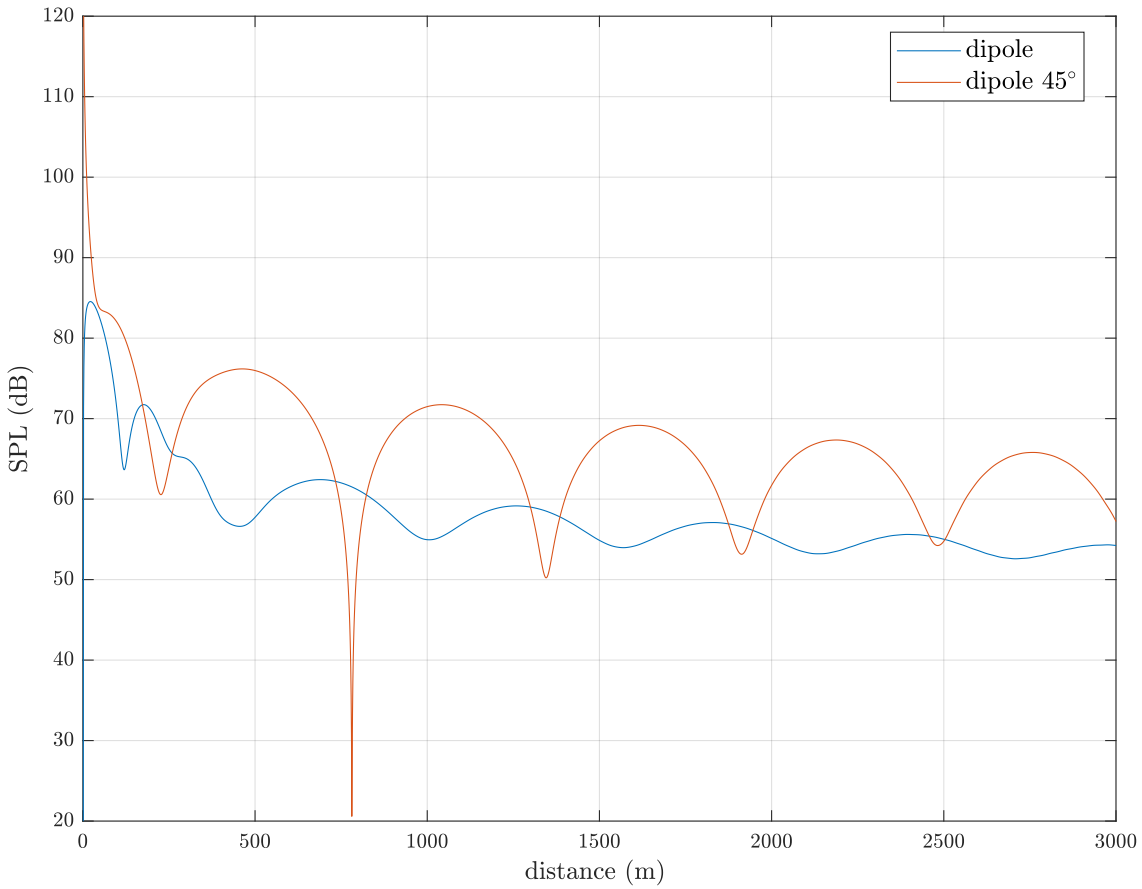

Figure 3.18: SPL of the 20 Hz dipole at a depth of $z = 36$ m: a) horizontal dipole; b) dipole inclined by 45° with respect to the free surface.

figure:wavenumber we show that the modes of the inclined dipole are comparable to those of the monopole. In Figure 3.19 we show the SPL over the $x - z$ plane passing through the inclined dipole. The black line is at a depth of 100 m at the interface between the fluid layer and the sediment layer. The inclination of the dipole enables more reflection of energy at the seabed than the case of the horizontal dipole (Figure 3.16 *b*), where most of energy leaves the domain. This aspect is related to the angle of incidence of the acoustic waves at the interface between the two media. Obviously, different orientations may give rise to different energy patterns, showing that directivity typical of real world sources introduces non trivial effects worth of analysis. The minima of SPL along the water-air interface are narrower for the inclined dipole compared to the horizontal one. Different orientations may give rise to different energy patterns, showing that directivity typical of real world sources introduces non trivial effects worth of analysis. The situation may be even more complex in presence of multiple sources.

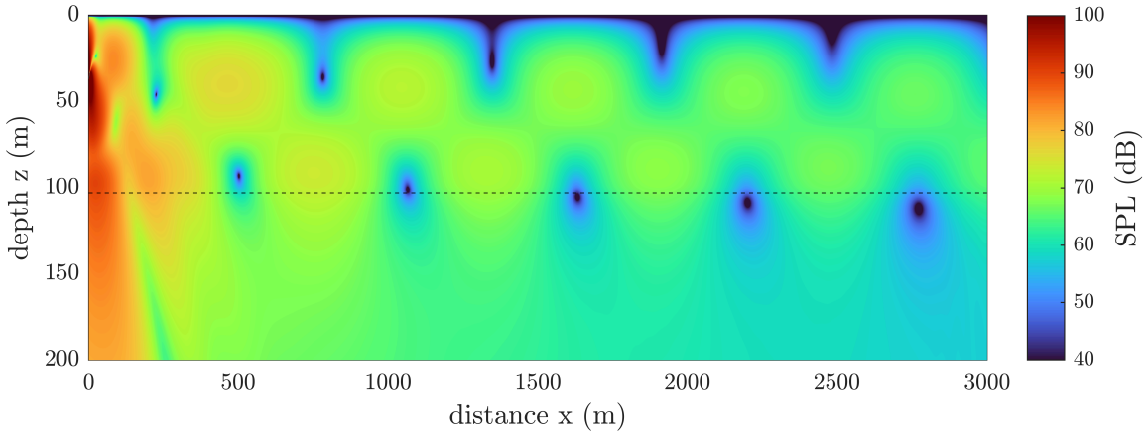

Figure 3.19: SPL on the $x-z$ plane passing through the 20 Hz dipole inclined by 45° with respect to the free surface.

Chapter 4

Full Acoustic Analogy

For simple omnidirectional sources, such as a monopole, propagation models based on the solution of the Helmholtz equation are widely used. They can evaluate the propagation over very long distances in stratified media, which approximate a marine environment. Flow-generated sources, which constitute the majority of the anthropogenic noise emission, are characterized by complex acoustic directivity patterns not assimilable to omnidirectional sources. Therefore, using only propagation models based on the Helmholtz equation is impossible due to the difficulties in considering the directivity. A different approach must be followed, and usually for acoustic pressure generated by the interaction of fluid and immersed objects, the propagation can be evaluated following two numerical approaches: the direct and hybrid methods.
The direct approch relies on the solution of both the sound and the fluid dynamics fields, and it is achieved by solving the compressible Navier-Stokes equations. This methodology can directly solve the propagation in a complex domain such as a marine environment. However, the computational cost of renders this option non-viable even for simple realistic cases.
In the hybrid method, the computation of the fluid dynamics field is decoupled from the computation of the acoustic field. This decoupling enables the ouse of different techniques to solve the fluid dynamics field, which expands the range of applications to realistic problems such as marine propellers or aircraft nozzles. Still, high-fidelity unsteady numerical fluid flow simulations must be conducted to correctly reconstruct the noise emitted by a specific source. The far-field acoustic pressure is evaluated by integrating an acoustic analogy, a mathematical formulation that rules the conversion of the flow's kinetic energy into acoustic energy. This method is well known in the scientific community and largely applied to the study of flow-generated noise. This method allows to fully characterize the noise source but has important limitations concerning the noise propagation process. Indeed, the solutions are generally valid for an infinite homogenous medium, which does not represent a realistic environment.
On the other hand, propagation models based on the wave equation's solution in time and space can propagate complex directivity patterns in heterogenous media and we consider

them suitable to propagate the flow-generated sources correctly. Therefore, this propagation model could be used as a third step of the hybrid method, defining a new methodology called Full Acoustic Analogy. The complexity, in this case, is coupling the acoustic pressure computed with the acoustic analogies with the propagation model.
In this chapter, we describe the Full Acoustic Analogy and all the steps necessary to obtain the propagation of acoustic pressure from a flow-generated sound. In particular, to introduce this new methodology, we show its application to a marine propeller.

4.1 The Full Acoustic Analogy

The Full Acoustic Analogy (FAA) extends the classical hybrid methodology used to compute acoustic pressure propagation in a complex far-field environment, adding a third step that relies on the acoustic wave equation.
The methodology is defined by three separate steps, as presented in the flowchart in Figure 4.1. The first two steps correspond to the hybrid methodology used to compute the acoustic

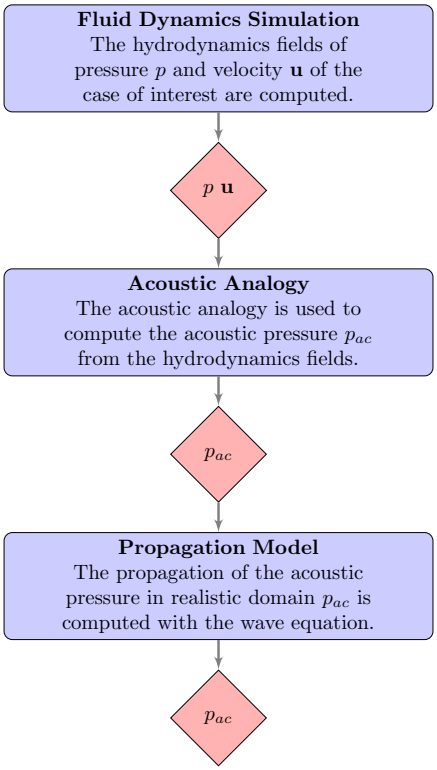

Figure 4.1: Flowchart of the proposed methodology.

pressure for flow-generated sound. In the first step, a CFD simulation is conducted, which evaluates the velocity and pressure that generates the sound. Laboratory measurements

could also be exploited at this stage. Different approaches can be used to evaluate the hydrodynamics fields, such as DNS, LES or URANS. Generally, high-resolved unsteady simulation must be performed to ensure that the fluid flow structures are finely reproduced. In the second step, an acoustic analogy is applied: the fields of pressure p and velocity v are used to compute the acoustic pressure p_{ac}. For example, for a free-shear flow, one can use the original formulation of [43], or one can used the integral formulation of FW-H or the FW-H porous formulation propose by [20]. Also, proper laboratory or off-shore measurements may provide for the acoustic pressure p_ac. The second step, therefore, is used to characterize the source and provide a source term for the propagation model used in the third step.
The third step is defined by a propagation model, which solves the wave equation and evaluates the propagation of the acoustic waves in a realistic environment. In principle, any propagation model can be used; we chose to discretize and solve the wave equation in the time-space domain through a finite difference method. The advantage of considering the third step is that the propagation models can include reflection and refraction effects. The delicate aspect concerns how to fit data obtained in step two to the solver adopted in the third step.
In the next subsection we describes the case study we used to verify this new methodology.

4.2 Fluid Dynamics Simulation

Different approaches can be followed to solve the hydrodynamics fields, such as DNS, LES, or URANS. The difference between these approaches is the capability to resolve the turbulence structures. DNS is capable of solving all the turbulent scales of the flow but requires high computational costs. URANS, cut away the turbulence off the smallest scales and often fails to reproduce the coherent structures of the flows responsible for the noise emitted. For this reason, in recent literature, URANS simulations have been reported as an insufficient methodology for the purpose of acoustic analysis. As a consequence, URANS are mainly used for resolving engineering cases due to the lower computational cost. The LES method is obtained by applying a filtering operator to the Navier-Stokes equations; therefore, this method can capture the turbulence's more energetic length scale of the problem, filtering out the smallest length scales. Being a compromise between accuracy and computational cost, a Large-Eddy Simulation has been identified as the best-suited method to be applied for acoustic purposes.
In this thesis, we focus on analyzing the noise generated by a marine propeller. The theoretical studies in [35] highlight the necessity to resolve the wake of marine propellers in order to resolve their acoustic signature. Indeed, it was found that the wake turbulent structures developing from the tip of the blades generates noise. The importance of the wake contribution was also highlighted in [15], and more recently in [57], where in both numerical experiments, the LES approach was used. All the simulations are performed in open-water conditions, meaning that the simulations are carried out considering an isolated immersed propeller. This approach is necessary since it is still unaffordable to carry out

the numerical simulation with enough accuracy considering complete problem, constituted by the propeller, the hull of the ship and the free surface.
Another major source of noise for marine propellers is the inception of cavitation [72]. Cavitation bubbles develop in negative pressure zones, which are a consequence of the increased flow velocity at the propeller blade. The successive generations and collapse of gas bubbles determine the emission of acoustic waves. The cavitation phenomena are usually reproduced in CFD simulation with cavitation models [40, 60], and different examples of numerical simulation of cavitating propellers are available [4, 63]. Still, it is an ongoing field of research due to the complexity of reproducing this phenomenon correctly, both from a fluid dynamic point of view and (mainly) concerning the related noise emission. We mentioned cavitating flows because, in principle, our proposed methodology can consider the cavitation phenomenon. The only limitation we foresee for the propagation model is the coupling due to the high-frequency range associated with the cavitating flows (over kHz).

4.2.1 Numerical Simulation of a Marine Propeller

The fluid dynamics case taken into consideration is the CFD simulation of the five-blade benchmark propeller [66]. The fluid dynamic data are those obtained in a previous study [15]. The details of the case under study and the fluid dynamic simulation are recalled briefly. The isolated propeller is immersed in a uniform flow, working in pull-conditions. The advance ratio of the propeller and the Reynolds number of the numerical experiment are:

$$J = \frac{U_0}{nD} = 1.0683, \qquad Re = \frac{U_0 D}{\nu} = 889680,$$

where $U_0 = -4\,m/s$ is the advance velocity, n is the rotational velocity in revolutions per seconds (rps) and $D = 0.25\,m$ is the diameter of the propeller. Indicating with S the thrust and with Q the torque, the nominal values of the thrust (K_T) and the torque (K_Q) coefficients provided by the propeller with a advance ratio of $J = 1.0683$ are:

$$K_T = \frac{S}{\rho n^2 D^4} = 0.3538, \qquad K_Q = \frac{Q}{\rho n^2 D^5} = 0.09096,$$

where $\rho = 1000\,Kg/m^3$ is the water density. The numerical domain of the CFD simulation is a cylindrical mesh, as depicted in Fig.4.2.
The LES was conducted in a rotating frame of reference, as proposed in the article of [39]. The incompressible Navier–Stokes equations were rewritten as a function of the absolute velocity vector, taking into account the rotation effect and adding the Coriolis and centrifugal body force terms. The numerical experiment was performed within the OpenFOAM 2.3.0 framework, where the incompressible Navier-Stokes equations were solved using the Pressure-Implicit with Splitting of Operation (PISO) algorithm. The numerical schemes adopted were a second-order linear upwind scheme in space and a backward time integration, thus ensuring a second-order overall accuracy. The SGS stress tensor was modelled using the Dynamic Lagrangian model developed by [47]. A wall model was utilized, which

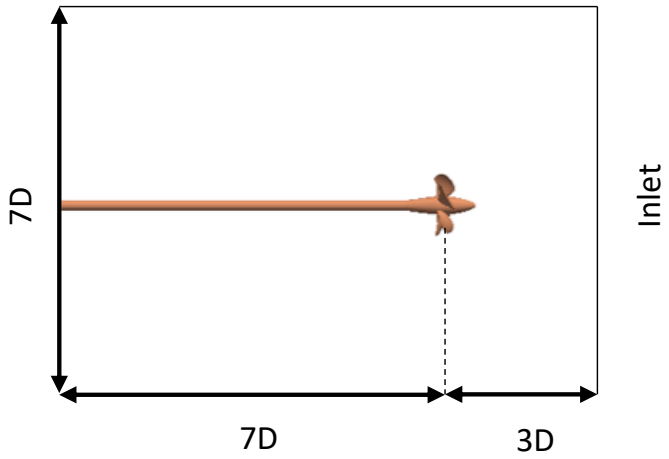

Figure 4.2: Schematic of the numerical domain of the propeller CFD simulation.

allowed locating the first grid point off the wall at a distance of about $y^+ = 40$. The relative error of the integral quantities obtained with the numerical simulation were $e_{K_T} = 3.5\%$, and of $e_{K_Q} = 0.5\%$.
In Figure 4.3, coherent structures are visualized using the Q-Criterion (isosurface $Q = 20000$) coloured with $x-component$ of the vorticity vector. Both the tip vortex and the shaft vortex are visible, being the latter more intense and persisting downstream. Indeed, due to the pull-condition a strong vortex rolls-up on the shaft, which was also considered an important source of noise, at very low frequencies (see [15] for details).

4.3 Acoustic Analogies

The far-field acoustic pressure is evaluated by integrating an acoustic analogy. Lighthill [43] originally derived from the equations of mass and momentum conservation of a compressible fluid the acoustic analogy for a free-shear flows. The theory was later extended by [26] incorporating the effects of a moving body in a medium. This enabled the use of the hybrid approach for the computation of the noise generated by complex rotating object. A detailed review by Wang et al. [69] describes the limit and the ongoing research in this field. In this work, we used the integral formulation FW-H analogy 4.1, which is described in more detail in the next subsection 4.3.1. Other approaches can be used to evaluate the acoustic pressure, such as the porous formulation proposed by [20]. Any approach capable of evaluating the acoustic pressure at a specific microphone in space can be used for the coupling procedure with the propagation model descripted in 4.4.1.

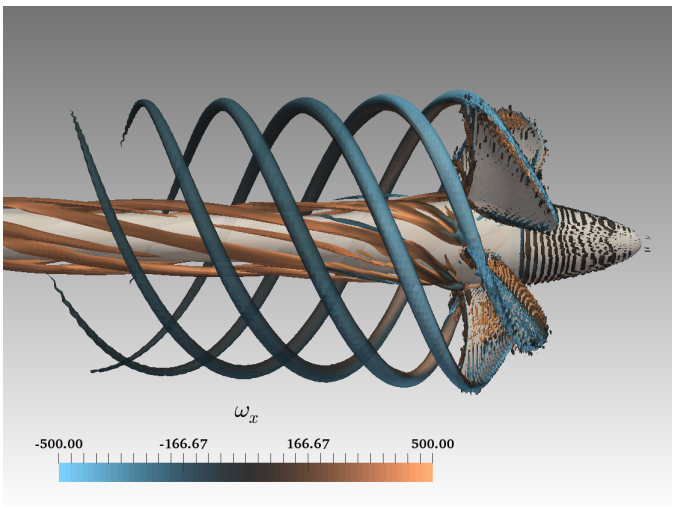

Figure 4.3: Isosurface of the Q-Criterion ($Q = 20000$) coloured with value of the $x-$*component* vorticity between the range $[-500, 500]$.

4.3.1 Ffowcs-Williams and Hawkings Analogy

The FWH is a general formulation of the Lighthill acoustic analogy, which considers the effects of an arbitrary body in motion. The acoustic pressure p_{ac}^{fwh} originated by a moving source within a fluid is evaluated with the following FW-H equation:

$$\begin{aligned} p_{ac}^{fwh}(\mathbf{x},t) \;=\; & \frac{\partial}{\partial t}\int_S \left[\frac{\rho v_i \hat{n}_i}{4\pi r|1-M_r|}\right]_\tau dS + \frac{1}{c_0}\frac{\partial}{\partial t}\int_S \left[\frac{\tilde{p}\hat{n}_i\hat{r}_i}{4\pi r|1-M_r|}\right]_\tau dS \\ & + \int_S \left[\frac{\tilde{p}\hat{n}_i\hat{r}_i}{4\pi r^2|1-M_r|}\right]_\tau dS + \frac{1}{c_0^2}\frac{\partial^2}{\partial t^2}\int_W \left[\frac{T_{rr}}{4\pi r|1-M_r|}\right]_\tau dW \\ & + \frac{1}{c_0}\frac{\partial}{\partial t}\int_W \left[\frac{3T_{rr}-T_{ii}}{4\pi r^2|1-M_r|}\right]_\tau dW + \int_W \left[\frac{3T_{rr}-T_{ii}}{4\pi r^3|1-M_r|}\right]_\tau dW \end{aligned} \tag{4.1}$$

where $T_{ij} = \rho u_i u_j + \left(\tilde{p} - c_0^2\tilde{\rho}\right)\delta_{ij}$ is the Lighthill tensor, $\tilde{p} = p - p_0$ denotes the fluid dynamic pressure perturbation with respect to the reference value p_0, ρ is the bulk density, $\tilde{p} - c_0^2\tilde{\rho}$ is deviation from an isentropic behaviour, $\hat{n}$ is the (outward) unit normal vector to the surface element dS, dW is the volume element, $r = |\mathbf{x} - \mathbf{y}|$ is the source-observer distance, being $\mathbf{x}$ the coordinate of the position of the microphone and $\mathbf{y}$ the coordinate of the source, $\hat{r}_i$ is the i-component of the unit vector $(\mathbf{x} - \mathbf{y})/r$, v_i is the i-component of the surface velocity vector, $M_r = v_i\hat{r}_i/c_0$ is the local Mach number in the source-observer direction, with c_0 the speed of sound.
The integral terms have to be evaluated at the emission time τ which, in the present case, is assumed equal to the observer time t. This assumption is valid since the rotational speed of the marine propeller considered in this work is much lower than the speed of sound

and the source extension is such that the Maximum Frequency Parameter $MFP > 1$ (for details see [14]). A more detailed description of the propeller's acoustic compactness here considered is reported in [15]. This approximation is not generally valid for high Mach numbers, where the rotational speed of the surfaces is approaching the speed of sound.
The three surface integrals, referred to as linear terms, are associated with the noise generated by the rigid surface immersed in the flow. The first (thickness) term is related to the body motion, while the second and third terms (loading) are related to the unsteady pressure loads over the propeller blades. The volume terms evaluate the contribution of the fluid flow structures which populate the wake.. These terms are defined as non-linear. We note that vortex noise may be dominant, mostly in the wake direction. However, the present study focuses on the linear terms contribution only; thus, we evaluate the acoustic pressure through the FW-H equation (4.1) considering only the surface integrals. However, the non-linear terms can be retained and evaluated directly with the original FWH equation (Eq. 4.1). We are still evaluating the verification of this methodology with the non-linear terms. A brief description of the ongoing research is given in 5.2.

4.3.2 Ffowcs-Williams and Hawkings Analogy applied to a Marine Propeller

The evaluation of the acoustic pressure with the integral FW-H equation 4.1 of the [66] propeller is described in detail in [15]. The hydrodynamic pressure and velocity on the blades is integrated to obtain the acoustic pressure at a distance r from the propeller. As an example, in Figure 4.4, we show a directivity plot of the linear term.

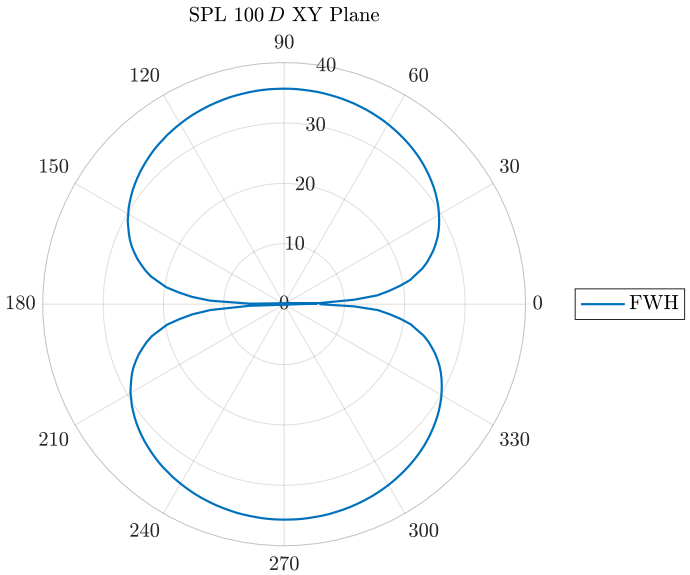

Figure 4.4: Directivity plot of the linear terms of the FW-H equation 4.1.

Instead, the integration of the volume term is calculated on a volume that contains the

most energetic structure of the fluid flow, as observed in Figure 4.5. The Figure shows a schematic of the FW-H domain: a cylinder with axis aligned with the propeller axis and radius $r = 0.6\,D$.

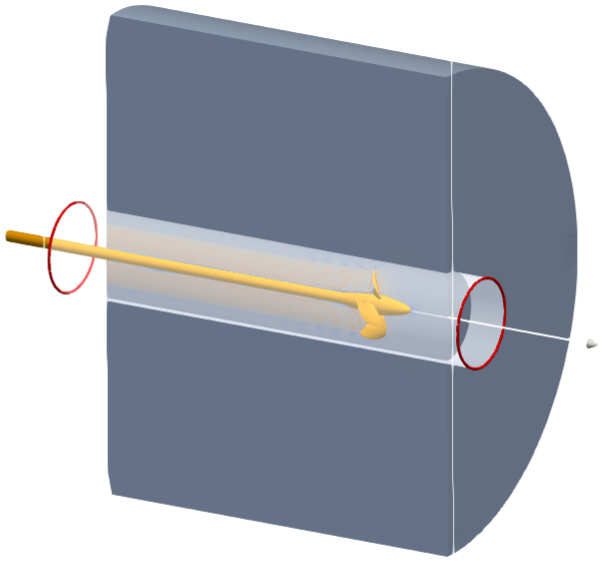

Figure 4.5: Schematic of the integration volume of the non-linear terms of the FWH equation 4.1.

In Figure 4.6, we show the directivity plot, with SPL value, of the non-linear terms of the FW-H equation at $100D$ from the propeller. The propeller axis and the wake direction are oriented along the 180°.

4.4 Propagation Model

The propagation model is used to propagate the acoustic pressure generated by the complex source. Any propagation model can be used for this step. The most important aspect is the coupling between the acoustic analogy and the propagation model. The coupling with the acoustic wave equation is defined in this thesis in the next section 4.4.1. A different coupling is proposed in [45], where the author used a 2D propagation model based on the acoustic wave equation and coupled with the acoustic pressure generated by a biomimetic flapping-foil thruster. The noticeable difference between the proposed methodology and the paper's results is that the author did not perform a CFD simulation to obtain the hydrodynamics fields but relied on an analytical approximation of the loading term.
A coupling with the Helmholtz equation could also be defined based on directivity functions used in particular propagation models. This aspect was not treated in this work.

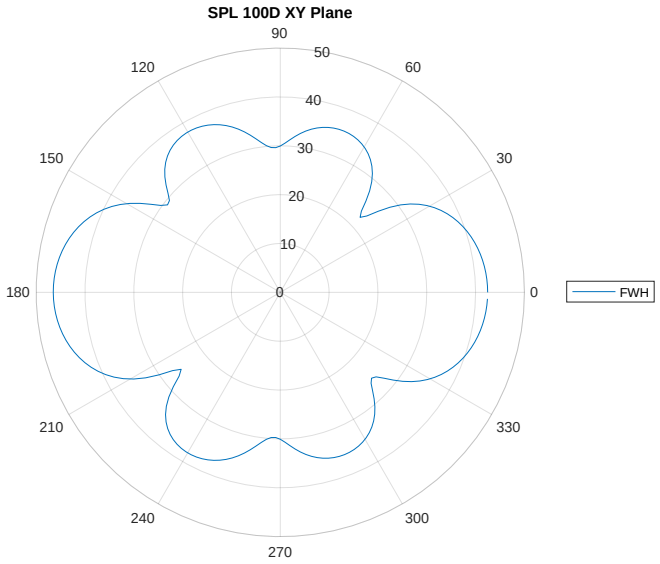

Figure 4.6: Directivity plot of the non-linear terms of the FWH equation 4.1.

4.4.1 Characterisation of Fluid-Generated Source by a Marine Propeller

The FWH equation characterized the source in the near field. The sources in the FDTD are implemented with the *hard source* method. In the following, we describe how we impose the acoustic pressure evaluated with the FWH equation 4.1 in the acoustic equation 2.1.
The nesting procedure consists in using the FW-H acoustic pressure p_{ac}, evaluated at specific microphones, as a forcing term for the acoustic wave equation, i.e., they act as boundary conditions. The procedure is described in detail for a marine propeller but can be extended to any compact source.
We considered a marine propeller placed at the center $(0, 0, 0)$ of the numerical FDTD domain, which has a constant grid spacing $\Delta x = \Delta y = \Delta z = 4D$, where $D = 0.25\,m$ is the propeller diameter. The schematic of the frame of reference together with the position of the propeller is depicted in Fig. 4.7. The propeller rotates counter-clockwise, and the wake develops along the negative $x-direction$. The important aspect is that the volume where we impose the acoustic pressure must be greater than the volume in which the FWH integral is computed.
The acoustic pressure is computed with the FW-H equation 4.1 at the specific microphones illustrated as red dots in Fig. 4.7, also representing the grid nodes where the time-varying Dirichlet boundary conditions for the wave equation (*hard source* method) are imposed:

$$p_{ac}^{w}(\mathbf{x}, t) = p_{ac}^{fwh}(\mathbf{x}, t), \qquad \mathbf{x} \in \Lambda, \tag{4.2}$$

where Λ is the ensemble of grid nodes illustrated as red dots in Fig. 4.7, p_{ac}^{w} refers to the acoustic pressure imposed in the propagation model, and p_{ac}^{fwh} refers to the acoustic pressure computed with the FW-H. The microphones where FW-H acoustic pressure is

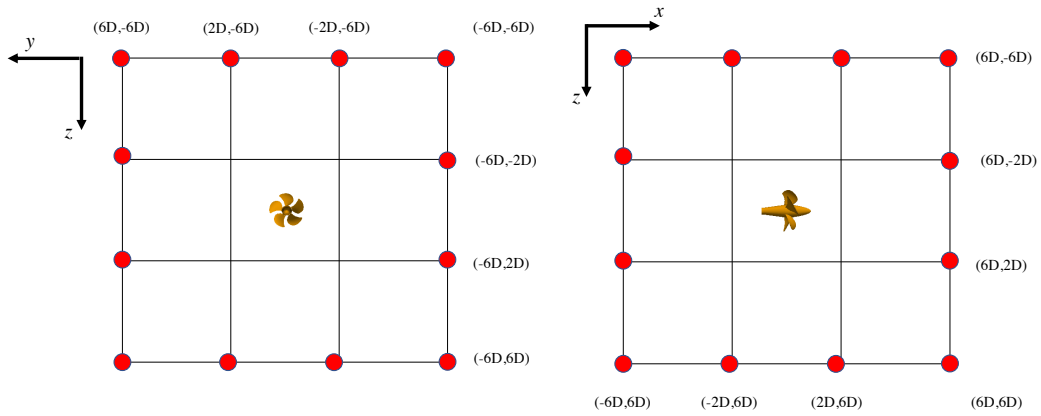

Figure 4.7: Schematic of the grid nodes used to implement the propeller acoustic source on two different planes: left panel, $x = 2D$; right panel $y = 2D$. The *hard source* nodes are depicted in red.

computed are chosen in such a way to correspond with the grid nodes of the FDTD. This approach avoids an interpolation procedure in space. The grid nodes that define the outer box vertexes are $(-6\,D, -6\,D, -6\,D)$ - $(6\,D, 6\,D, 6\,D)$. The cubic box, where the grid nodes (microphones) are distributed, is large enough to retain the source's directivity. In this case, these grid nodes are the second nearest grid nodes from the source center; since in these nodes the acoustic wave equation is not evaluated but imposed as a forcing boundary condition, all the nodes within the box are not considered for the solution of the wave equation while the grid nodes outside the box the acoustic wave equation (Eq.(2.3)) is solved.

The rationale of this choice stands on the fact that that the acoustic pressure gradient increases moving toward the source. Therefore, to evaluate the Laplacian correctly, two options are available: the first one is to increase the grid's spatial resolution which consequently increases the computational cost; the second one consists in applying the FW-H acoustic signals at grid nodes positioned at larger distances from the source, where the gradients of the acoustic pressure are less severe. Therefore, the choice of the dimension box has to be made to reach the following compromise: the box must be large enough to resolve the pressure gradient correctly and capture the directivity of the source correctly; the box has to be small enough to avoid spurious reflections in the presence of reflected waves (due for example to the free surface).

Because of the LES computational cost, the available FW-H signal is limited to a period of $T = 0.8\,s$, corresponding to about 12 revolutions. Linear interpolation in time is needed since the time step of the FDTD is typically less than the interval between two consecutive available measures of acoustic pressure computed with the FW-H equation. In addition, the FDTD method requires a more extended signal since the acoustic field needs to reach a statistically steady-state before calculating the root-mean-square of the acoustic pressure.

The time needed to reach a steady state solution depends on the size of the domain. The recommended time window to collect the results obtained with the wave equation has to be at least three times the time needed by the waves to reach the most distant boundary from the source of the numerical domain. If the time required by the FDTD method exceeds the available FW-H time signal, it is extended by repeating a copy several times until the time required by the FDTD method is obtained. This procedure may introduce errors in the range of the highest frequencies, which may be out-of-phase when the signal is truncated. A comparison of the sound Spectrum Level (SL) of the original FW-H signal (limited to a period $T = 0.8\,s$) and the same signal extended to $T = 2.4\,s$ is shown in Fig. 4.8. The original signal has been collected at the point $(-6\,D, -6\,D, -6\,D)$ and the SL is evaluated as $SL = 20\log_{10}(A/pref)$, where A is the amplitude of the Fast Fourier Transform of the acoustic pressure p^{fwh}_{acs} and $p_{ref} = 1\mu Pa$. Fig. 4.8 shows no evident difference in the spectral content between the two acoustic signals. Moreover, it must be pointed out that the energy-containing frequencies are the lowest ($< 20\,Hz$); consequently, the possible differences in the higher frequency ranges are of minor importance and can be neglected.

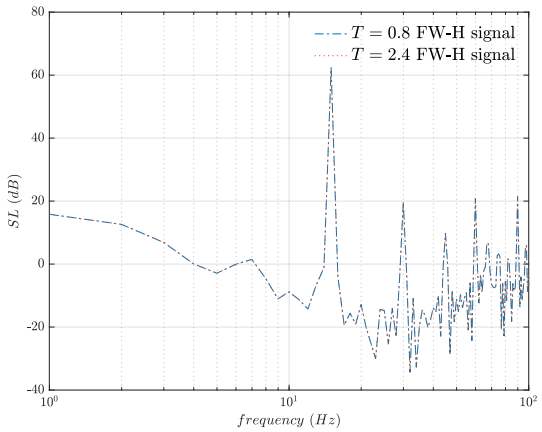

Figure 4.8: Comparison of the original FW-H signal (labeled $T = 0.8\,s$) and the same signal extended up to $T = 2.4\,s$ at the point $(-6\,D, -6\,D, -6\,D)$.

The propagation model implemented considered the medium quiescent and the source nodes fixed in time; thus, the fact that the source moves with a constant velocity is not taken into account in the propagation of the acoustic wave. Although, in principle, the source velocity should be considered, due to the small propeller's advance velocity compared to the speed of sound and to the dimension of the propagation domain, our assumption of fixed source point does not introduce appreciable errors. We note that to overcome this problem, a different coupling approch should be designed to compute the movement of the source.

Chapter 5

Verification Full Acoustic Analogy in a infinite homogenous domain

In this chapter we present the verification of the Full Acoustic Analogy in an unconfined and homogeneous medium for a marine propeller. We follow the step presented in Chapter 4 and in the first section 5.1 we show the verification obtained considering only the thickness and loading terms. In the second section 5.2, we show preliminary developments on the propagation of the acoustic waves that originated from the propeller's wake (volume terms of the FW-H equation). The marine propeller under consideration is evaluated in open water conditions with uniform inflow. The effect of the hull on the flow reaching the disk of the propeller is not considered. In addition, the hull is not included in the acoustic propagation, so the scattering effects resulting from the interaction between the acoustic waves and the hull are not considered. The inclusion of the hull in the propagation model is important to obtain a more realistic acoustic field. A new methodology developed in [2] to threaten the scattering of acoustic waves in an underwater environment could also be exploited with the propagation model presented in this thesis and will be addressed in the future.

5.1 Verification of the Full Acoustic Analogy applied to the linear term of FWH equation

The validity of the methodology, introduced in the previous section, is evaluated by comparing the acoustic results obtained by solving the wave equation with those obtained using the FW-H equation. Indeed, we point out that computing FW-H is equivalent to solving the wave equation in the case of unbounded and homogeneous domains.
We consider a homogenous infinite domain with $\rho = 1000\,Kg/m^3$ and $c = 1500\,m/s$. The FDTD domain is a square box, $404\,D\,(101\,m)$ wide, and the cell's width is set to $4\,D\,(1\,m)$. The open boundary conditions, applied in all directions, ensure that the acoustic waves can leave the numerical domain without reflections. Accordingly, the numerical experiment mimics an infinite domain. The propeller is placed at the center of the domain $(0, 0, 0)$. The

propeller axis is along the $x-direction$, the wake develops along the negative $x-direction$, and the propeller plane lies on the $y-z$ plane. A schematic of the $x-y$ plane of the domain is shown in Figure 5.1. The propeller is placed inside the red box, and the arrow defined the advance direction. The black line perpendicular to the red arrow is the line of microphones used for the comparison of the SPL. The nesting procedure follows the guidelines in section 4.4.1.

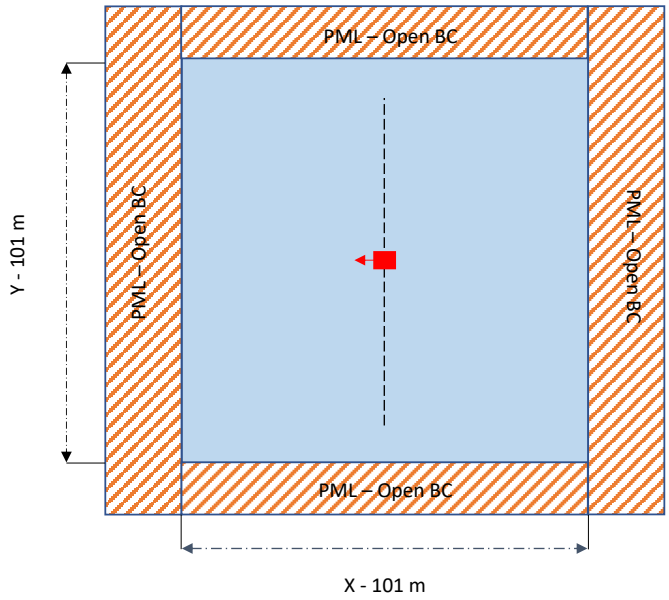

Figure 5.1: Schematic of the homogenous infinite domain. The red box represent the source and the red arrow the advance direction. The PML boundary layer are positioned at the edge of the square numerical domain.

The linear terms of the FW-H equation (4.1) are propagated with the FDTD method, and in Figures 5.2 and 5.3 we show the SPL over two different planes. As expected, the propeller generates a dipole-like pattern arises, which in this case is also related to the rotation of the source, as evidenced by, among the others, [33]. The linear terms of the FW-H equation generate most acoustic energy over the propeller plane, as evident from the comparison of Figures 5.2 and 5.3. The numerical experiment is conducted for $8\,\hat{t}$, where $\hat{t}$ is time made nondimensional as $\hat{t} = t * V_0/D$, with $V_0 = 4\,m\,s^{-1}$ the advance velocity of the propeller of the LES simulation and D the propeller's diameter. The results are then collected for $6\,\hat{t}$ starting from $2\,\hat{t}$. This time, $2\,\hat{t}$, is sufficient to enable the acoustic waves generated from the propeller to reach the furthest boundary. Then, the $6\,\hat{t}$ time window ensures that a statistically steady state is reached.
Fig. 5.2 shows the SPL on the $x-z$ plane with an offset of $2\,D\,(0.5\,m)$ in the $y-direction$. The plane passing through the propeller axis is not available since the propeller is located at the center of the grid cell (see Fig. 4.7). This holds for all numerical experiments herein

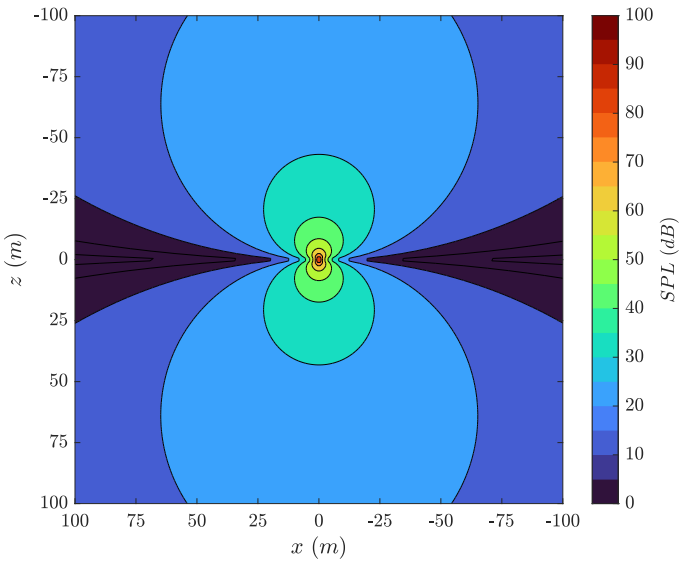

Figure 5.2: Contour of sound pressure level of the marine propeller in the open-water case on the $x-z$ plane at $y = 2D$, computed with the FDTD method, considering only the linear terms of 4.1

discussed.
The linear terms do not contribute to the acoustic energy along the propeller axis ($x-direction$) since the SPL decays rapidly below zero in this direction. Indeed, in this plane, the acoustic energy exhibits an axial-symmetrical dipole-like pattern. Fig. 5.3 shows that the SPL in the $y-z$ plane passing through $x = 2\,D$ is axisymmetric. Consequently, the acoustic pressure is evenly distributed in these planes. The combined analysis of Fig. 5.2 and Fig. 5.3 shows that a large part of the acoustic energy is contained in the $y-z$ planes close to the propeller.
In Fig. 5.4 we compare the acoustic pressure computed through the FW-H equation (4.1) with that obtained with the methodology proposed in this paper. The analysis is made by comparing the signals along the y-line $x = 2D$, $z = 2D$ contained in the $y-z$ plane, which is the plane that contains the most acoustic energy. The results from the FW-H equation are labeled FW-H, and the results from the FAA are labeled WAVE. The acoustic pressure evaluated with the FW-H method is recorded at probes positioned every $4\,D\,(1\,m)$ between $6\,D\,(1.5\,m)$ and $42\,D\,(10.5\,m)$ and then every $40\,D\,(10\,m)$, along the $y-direction$. The acoustic pressure evaluated with the FDTD method is recorded at the same points reported above, along the $y-direction$ The decay of the SPL is the same for both method, and the relative error is below 1% at all probes.
The pressure signal is then evaluated at a single probe, placed at ($2D$, $202D$, $2D$) from the source to verify that the acoustic pressure's spectral component is propagated correctly. The comparison between the SL of the two signals obtained with the two methods is shown in Fig. 5.5. The results are shown up to $100\,Hz$ since the FDTD method has a limitation

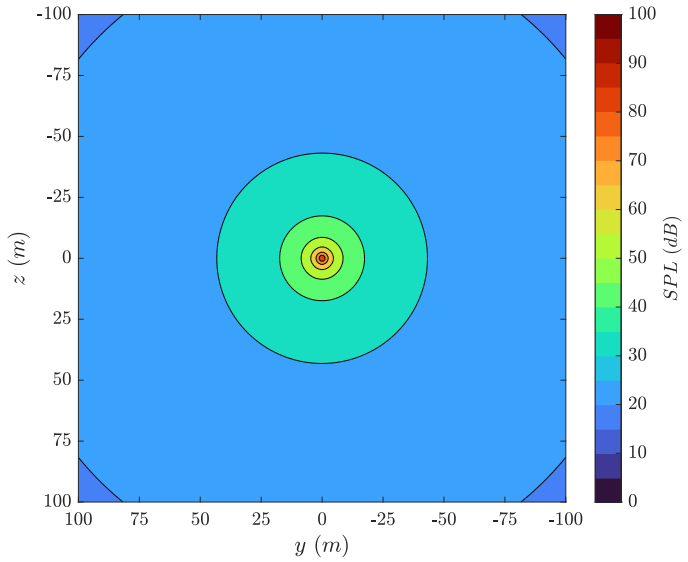

Figure 5.3: Contour of sound pressure level of the marine propeller in the open-water case on the $y-z$ plane at $x = 2D$, computed with the FDTD method, considering only the linear terms of 4.1

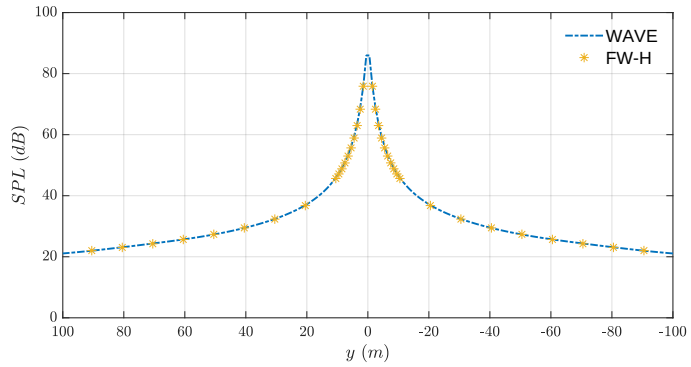

Figure 5.4: Comparison of sound pressure level on the line $x = 2D$, $z = 2D$ evaluated with the FW-H equation (FW-H) and with the wave equation (WAVE) for an unbounded domain and homogeneous medium, , considering only the linear terms of 4.1

on the maximum frequency which can be propagated without dispersion error. However, since most of the acoustic energy generated by marine propellers is concentrated in a low-frequency range, the FDTD method is suitable for this purpose. The coupled method correctly reproduces the peak frequency at $15\,Hz$, which corresponds to the propeller's revolution frequency ($n = 15\,rps$), and the relative error between the two amplitudes is less than 1.5%. The secondary peak that typically occurs at blade frequency nN is not observed in this case, due to the distance from the source. Indeed, it is observable in

the acoustic near-field up to few diameters ($\sim 6D$, see Fig. 4.8 and [15]). The low-frequency region is similar between the two methods, and only minor discrepancies in the high-frequency region are observed.

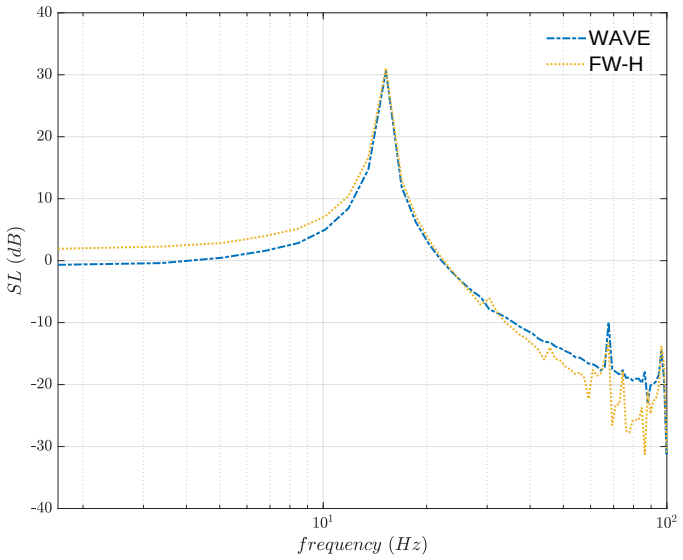

Figure 5.5: Sound spectrum level of the marine propeller evaluated with the FW-H equation (FW-H) and the wave equation (WAVE) at the point $(2\,D, 202\,D, 2\,D)$ for an unbounded domain and homogeneous medium, considering only the linear terms of 4.1

5.2 Preliminary results on the verification of the propagation of non-linear terms

In this second section, we show preliminary results on verifying the FAA considering the non-linear terms of the FWH equation 4.1. The numerical experiment is conducted on the same numerical domain presented in Figure 5.1. The only difference between the two cases is that we expanded the box containing the source. In this case, the grid nodes that define the outer box vertexes are $(-12\,D, -12\,D, -12\,D)$ - $(12\,D, 12\,D, 12\,D)$. Therefore, we doubled the dimension of the box. The smaller box did not capture the increased complexity of the directivity pattern of the non-linear terms; consequently, we enlarged the dimension of the box. We were able to achieve promising results, at lest in the vicinity of the propeller.
In Figure 5.6 we show the comparison between acoustic pressure computed through the FW-H equation (4.1) with that obtained with the methodology proposed in this paper over the same line utilized in Figure 5.4. The domain is limited to half the length for better visualization of the results. The results from the FW-H equation are labeled FW-H, and the results from the wave equation are labeled WAVE, as in the previous case. We can see the dimension of the *hard source* box, since the SPL is 0 from $0\,D$ to $12\,D$. We observe that in the near field up to $72\,D\,(8\,m)$ the decay of the SPL is similar, but after the SPL decay differently. The results from the wave equation decay as $\approx 1/r$ after $72\,D\,(8\,m)$, while the decay of the FWH is still $\approx 1/r^2$ and start decay as $\approx 1/r$ at $180\,(45\,m)$. As a results in the far-field the acoustic wave equation overestimate the results from FW-H.

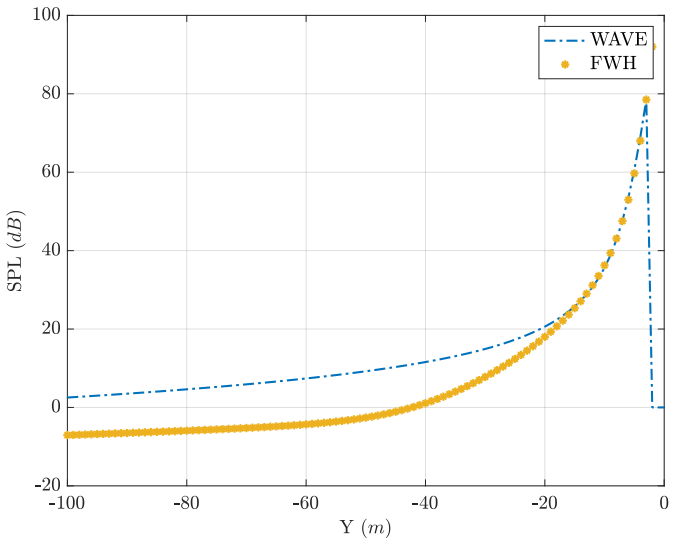

Figure 5.6: Comparison of sound pressure level on the line $x = 2D$, $z = 2D$ evaluated with the FW-H equation (FW-H) and with the wave equation (WAVE) for an unbounded domain and homogeneous medium, considering only the non-linear terms of 4.1

The overestimation is not localized on the line shown in Figure 5.6, but it accusers in all directions, as shown in Figure 5.7. In this Figure, two directivity plots of the SPL are present at two different radii. In Figure 5.7 *a*), the comparison between the results obtained with the FW-H equation and the wave equation at $r = 50\,D\,(\,12.5\,m)$ show good agreement. The main differences are observed on the two lobes perpendicular to the propeller axis. Up to this distance, the directivity of the acoustic pressure is reproduced correctly by the wave equation along with the amplitude. At $r = 100\,D\,(\,25\,m)$, instead, we observe (as in Figure 5.6) an overestimation of the SPL in all directions, in particular along the propeller axis. Another important aspect is directivity shape. The results from the wave equations lost the characteristic directivity pattern obtained with the FWH and developed a more oval shape.

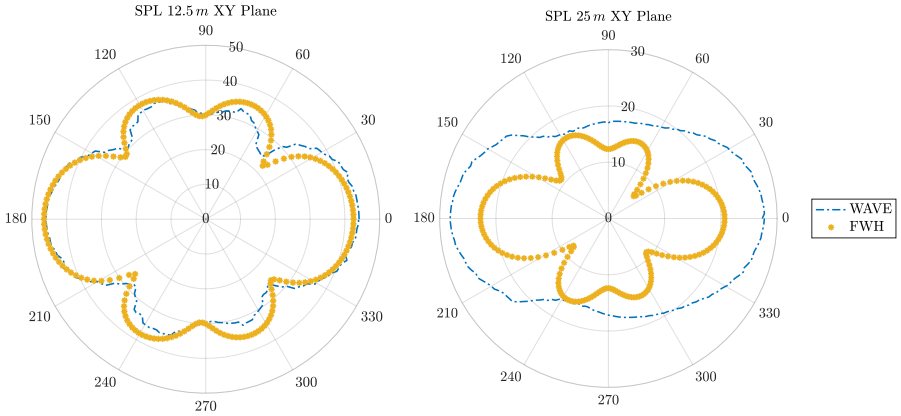

Figure 5.7: Directivity plot of the SPL evaluated with the FW-H equation (FW-H) and with the wave equation (WAVE) of the non-linear terms of 4.1: a) at fixed radius $r = 50\,D\,(\,12.5\,m)$, b) at fixed radius $r = 100\,D\,(\,25\,m)$

We are investigating the possible cause related to these discrepancies.

Chapter 6

Propeller noise propagation in a confined basin

In this chapter, we apply the FAA methodology to evaluate the effects of a confined basin on the propagation of the acoustic waves generated by the marine propeller, which is the same analyzed in chapter 5. The acoustic fields develop distinct regions of minima and maxima, and we investigate the causes.
In the first section 6.1, we analyzed the acoustic pressure propagation in a canal. In the second section 6.2, we discuss a symmetry breaking of the acoustic fields.

6.1 Acoustic propagation in a canal

In this section, we analyze sound propagation in a canal that exhibits interesting differences from the open-space case.
The domain considered herein is a simplified perfectly reflecting canal with a free surface at the top boundary, a schematic of the domain is presented in Figure 6.1. The canal is $200D$ $(50\,m)$ deep, $412\,D\,(103\,m)$ wide and $1612\,D\,(403\,m)$ long. Along the $x-direction$ open boundary conditions are imposed, mimicking a canal infinite in length.
The analysis conducted is devoted to quantifying the effect of confinement on the composition of direct and reflected acoustic waves generated by the propeller. Therefore, the dimension of the channel is not crucial for the main scope of our research. However, we may note that the dimensions we have chosen are comparable with those of the Suez Canal which has a depth of $\simeq 25\,m$, a width of $\simeq 300\,m$ and a length of the order of tens of kilometers.
At $z = 0$ we set the free surface boundary condition $p = 0$, mimicking the interface between water and air. At $z = 200\,D\,(50\,m)$, the bottom wall is considered as a perfect reflecting surface so as the two lateral boundaries, and it is obtained by imposing the Neumann boundary condition. This can be considered an approximation of the reflection occurring at the interface between water and a medium much denser than water. The water has a constant density ($\rho = 1000\,Kg/m^3$) and speed of sound ($c = 1500\,m/s$). The numerical

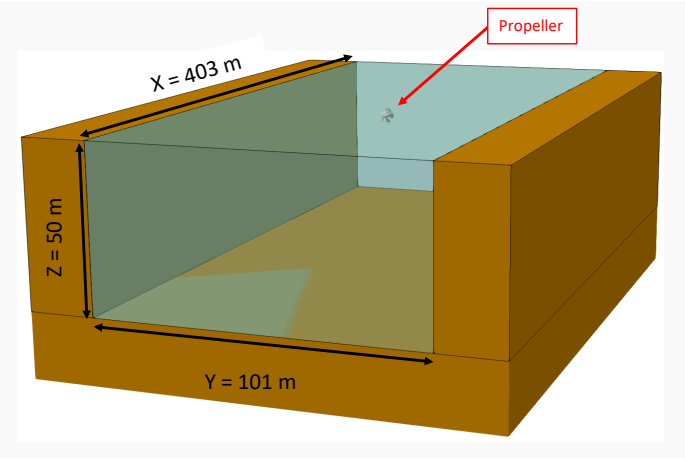

Figure 6.1: The brow walls represent the perfectly reflecting walls, and we underline that the canal is open along the $x-direction$.

experiment is conducted on a grid with a cell's width of $4\,D\,(1\,m)$ and in a time window of $8\,\hat{t}$, where $\hat{t}$ is time made nondimensional as in the previous chapter($\hat{t} = t * V_0/D$, advance velocity $V_0 = 4\,m\,s^{-1}$, propeller's diameter D). Then, in order to compute the root-mean-squares, the acoustic pressure is collected in the time interval $2\,\hat{t}-8\,\hat{t}$. The propeller in this numerical experiment is located at the center of the canal at a depth $22\,D\,(5.5\,m)$. It is representative of an underwater vehicle passing through the canal.
The acoustic pressure signal imposed at the nodes of the FDTD is the superposition of the direct and image signal computed with the FW-H equation. With the image method applied to the FW-H equation through the use of the half-space Green function, we consider the reflected waves by the nearest boundary to the source, in our case, the free surface. We showed that with the *hard image* method 3.1, which considers the source signal as the composition of direct acoustic waves and reflected ones from a free surface, a more accurate estimate of the propagated acoustic field is obtained.

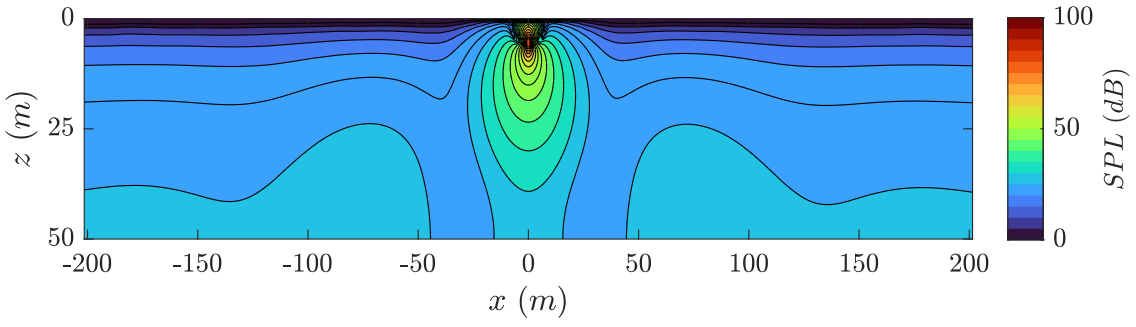

Figure 6.2: Contour of sound pressure level of the marine propeller in the canal case on the $x-z$ plane at $y = 2D$, computed with the FDTD method.

In Fig. 6.2 we show the contour of the SPL of the marine propeller in the canal case, extracted on plane $y = 2D$, close to the propeller axis. The characteristic dipole-like pattern observed in Fig. 5.2 for the open-water case is still observed in this case with substantial differences; the main difference is lack of symmetry with respect to the horizontal plane containg the axis of the propeller, due at large extend to the presence of the free surface and, also, to the presence of the lateral walls. The zero sound emission line, namely the propeller axis in the open water case, is now bent towards the free surface. A shadow zone, meaning an insonified region of the domain, is noticed along the free surface and spans the whole channel's length, deepening with the distance from the source. This shadow zone is the result of scattering of the acoustic waves incident on the free surface [31, 37]. The SPL is symmetric along the $x-direction$, whereas regions of higher and lower SPL are identified on the plane. In particular, a region of increased SPL is observed attached to the bottom from about $200\,D\,(50\,m)$ to the end of the channel due to bottom reflections. A region of lower SPL is observed between this region and the source, spanning from the free surface to the bottom wall. These effects result from the superposition of different acoustic waves reflected from the domain boundaries. Indeed, the canal's acoustic energy is constrained inside the canal compared to the open-water case, as shown in Fig. 6.3.

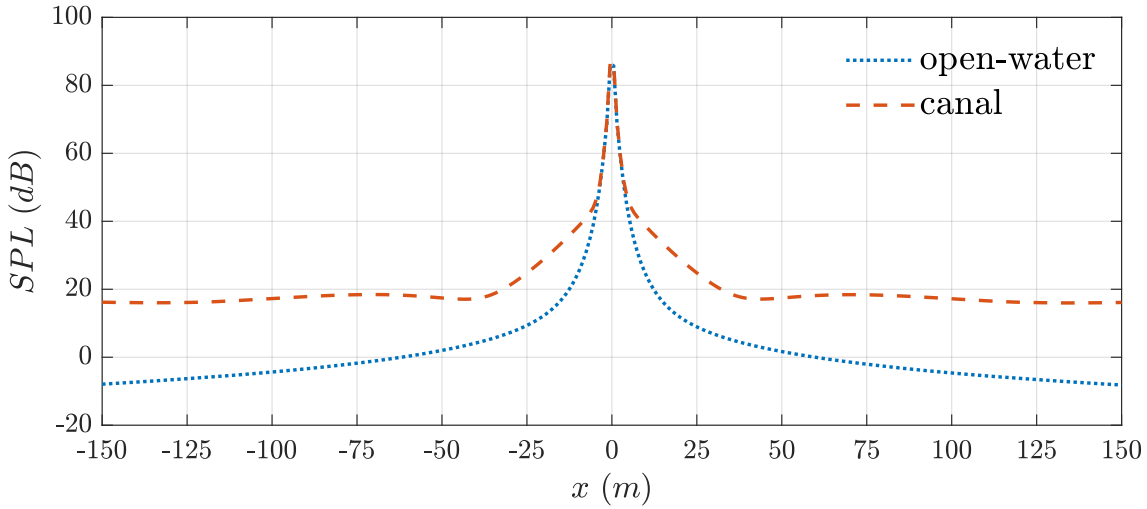

Figure 6.3: Comparison of the sound pressure level of the marine propeller in the canal case and the open-water case (Fig. 5.4) along the line $y = 2D$, $z = 2D$, computed with the FDTD method.

Specifically, in Fig. 6.3, we compare the SPL of the marine propeller, in the canal case and in the open-water case (Fig. 5.4), computed along the line $y = 2D$, $z = 2D$. In the open-water case, the SPL monotonically decays below zero because the decay of the acoustic pressure is governed by the geometrical spreading of the acoustic waves. This not holds in the canal case, where three different rates of decay of SPL with the distance from the source are detected: in the very near field, the decay rate is the same as in the open-

water case; the difference appears precisely at a distance equal to the depth of the source. This is because the spherical spreading of the acoustic waves is interrupted by the presence of the free surface and resulting reflection. Moving farther, the decay rate changes and remains constant almost up to the distance from the bottom, $178\,D$ ($44.5\,m$); even farther from the source, the acoustic energy remains constant along the canal's length since it is trapped inside the canal by the lateral and bottom walls and by the free surface. The change of decay appears mostly related to the presence of the upper and lower horizontal walls, whereas the nearly constancy of the signal in the far field has to be associated to the confinement of the acoustic signal in the cross-stream plane.

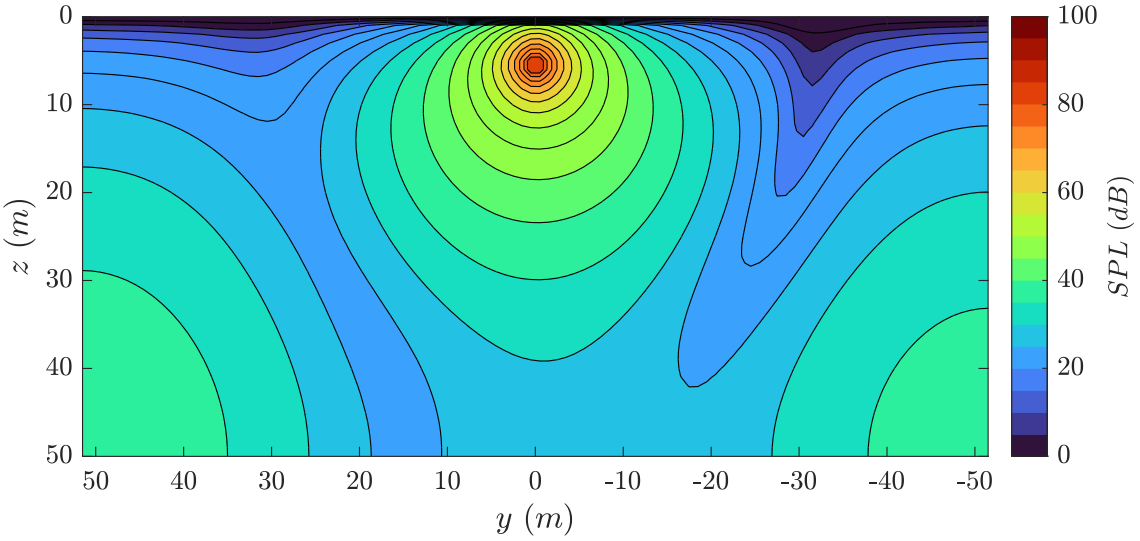

Figure 6.4: Contour of sound pressure level of the marine propeller in the canal case on the $y-z$ plane at $x = 2D$, computed with the FDTD method.

The presence of the four boundaries affects the distribution of acoustic energy also over the blade's plane, as shown in Fig. 6.4, where the contour of SPL of the marine propeller in the canal case is shown on the plane $x = 2D$. Similar to the $x-z$ plane, regions of relative maxima and minima of SPL are identified. At the bottom corners, large maxima of SPL are observed, but the SPL level is not the same at the two corners since the distribution of the acoustic energy is not symmetric with respect to the plane $y = 0$, where the propeller is located. This aspect is discussed further in Section 6.2. Between the corners and the source, a zone of minimum SPL at an angle of 53° to the bottom is observed. As discussed, the inhomogeneity of the SPL is due to the superposition of the acoustic waves reflected by the boundaries. In [18] these effects are examined for a very simple configuration; specifically, the authors provided a framework to evaluate the impact of a simple corner boundary on the acoustic field generated by a monochromatic monopole. We extend the mentioned work to highlight that the geometric characteristics of the domain are essential to understand the acoustic response for more complex cases. The total acoustic pressure

at a point close to a corner is obtained as

$$p_{tot} = F\, p_{dir} = F\, \frac{1}{r}\, exp(ikr), \tag{6.1}$$

where p_{tot} is the total pressure, F is the multipath factor , p_{dir} is the pressure of an open-water monopole, $k = 2\pi/\lambda$ is the wavenumber with λ the wavelength of the source, and r is the distance from the source. The multipath factor F is then evaluated as [18]:

$$\begin{aligned} F = \quad & 1 + R_h R_v \tfrac{q-s}{q+s} exp(i2ks) + exp\left[ik(s-q)\right] \\ \times \quad & \Bigg\{ R_h |cos^2\alpha + \left(\tfrac{q-s}{q+s}\right)^2 sin^2\alpha|^{-1/2} \\ \times \quad & exp\left(ik\sqrt{(q+s)^2 sin^2\alpha + (q-s)^2 cos^2\alpha}\right) \\ + \quad & R_h |sin^2\alpha + \left(\tfrac{q-s}{q+s}\right)^2 cos^2\alpha|^{-1/2} \\ \times \quad & exp\left(ik\sqrt{(q+s)^2 cos^2\alpha + (q-s)^2 sin^2\alpha}\right) \Bigg\}, \end{aligned} \tag{6.2}$$

where R_h and R_v are, respectively, the reflection coefficients of the horizontal and vertical wall, that constitute the corner ($R_h = 1$ and $R_v = 1$ in our case), q is the distance of the source from the corner, s is the distance of the corner from the observer (the distance from the source to the observer is then $r = q - s$), and α is the angle between the observer and the horizontal wall ($\alpha = 0.722\, rad$ in our case). In our case, the multipath factor F is function of the distance between the source and the observer only.
Here, we consider a monopole with $k = 0.0628\, m^{-1}$, which corresponds to a pressure signal oscillating at the revolution frequency of the propeller ($15\, Hz$), positioned at the same distance from the corner as the propeller in the canal case. We refer to this case as the *Ideal Corner Case*. In Fig. 6.5 we compare the p_{rms} computed through equation (6.1) with that obtained using the FDTD method, considering both the canal case (Fig. 6.4) and the ideal corner case. Pressure is computed along a straight line connecting the source with the corner from $kr > 0$ to $kr = 4.27$, where r is the distance from the source.
The ideal corner case mimics the case computed with Eq.(6.2), but is obtained by solving the acoustic wave equation with the FDTD. Therefore Neumann boundary conditions are imposed at the lateral walls that constitute the corner, while all other boundaries are treated as open. The p_{rms} is then collected in a time window sufficient to reach a steady state, and the grid cell dimension is $1\, m$.
As expected, the multipath factor and ideal corner case p_{ms} mostly overlap. Minor differences are observed near the minimum and near the source. The differences can be attributed to the assumption utilized in the evaluation of the multipath factor and the fact that the line in the ideal corner case is interpolated from the results over the numerical grid. Nevertheless, the location of the minimum of p_{rms} is correctly computed. We point out that the minimum of the p_{rms} of the canal case is located at the same distance as the

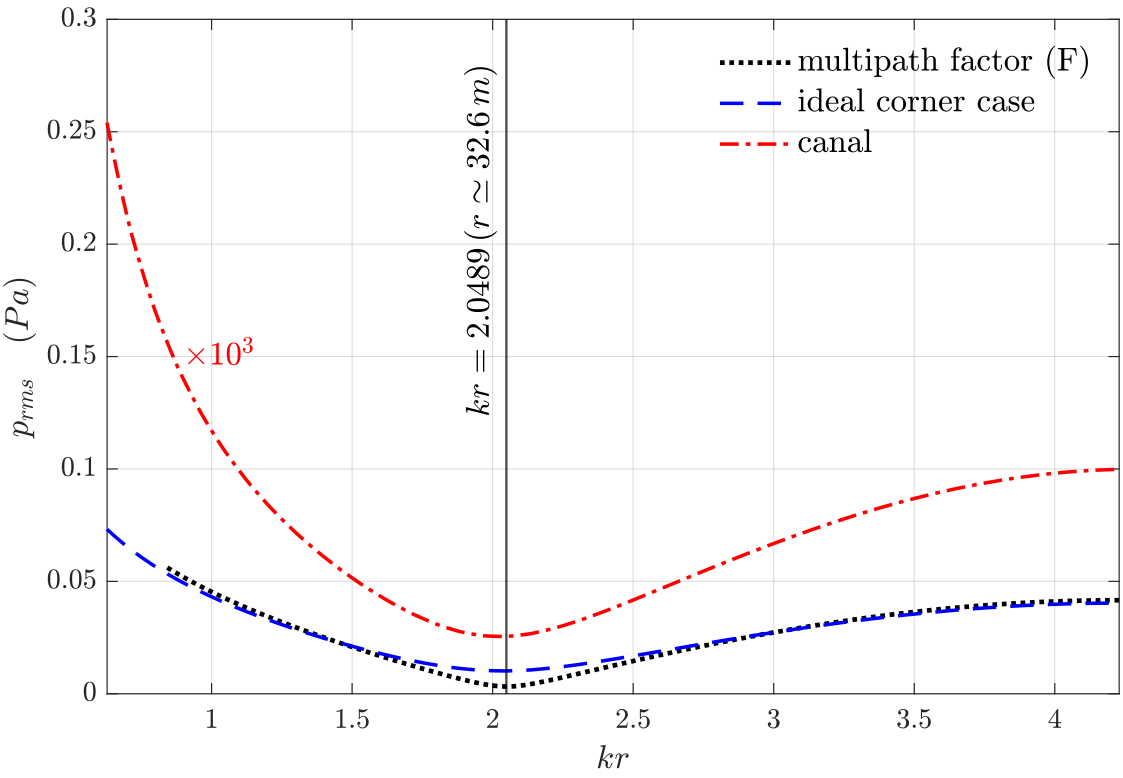

Figure 6.5: Comparison of the $p_{ac,rms}$ along the line connecting the source and the corner from $kr > 0$ to $kr = 4.27$ computed with equation (6.1), and the FDTD method in the ideal corner case and the canal case. The $p_{ac,rms}$ of the canal case is multiplied by a factor of 10^3.

other two cases. A contour plot of the SPL, in Fig. 6.6, shows the acoustic field in the two cases, ideal corner case and canal case. The location of the minumum is highlighted with a dashed line.

The multipath factor F formula represents a simpler case than the canal case since it does not consider all the others reflecting boundaries and a source with a specific directivity pattern. In spite of the simplification, the multipath factor F exhibits a minimum of pressure at a distance of about $kr = 2.0489\,(\simeq 32.6\,m)$ and a relative maximum close to the corner, similarly to the canal case. This simple analysis clearly shows that the presence of the corner definitely affects the acoustic energy distribution, and justify relative minima of SPL, as observed in Fig. 6.4.

A relative minimum is then also clearly identified in Fig.6.7, where a comparison of the SPL of the marine propeller in the canal case and the open-water case, computed along the line $x = 2D$, $z = 2D$ (the source depth), is shown. In Fig.6.7 we observe that two cases share the same decay near the source, up to a distance equal to the depth of the source

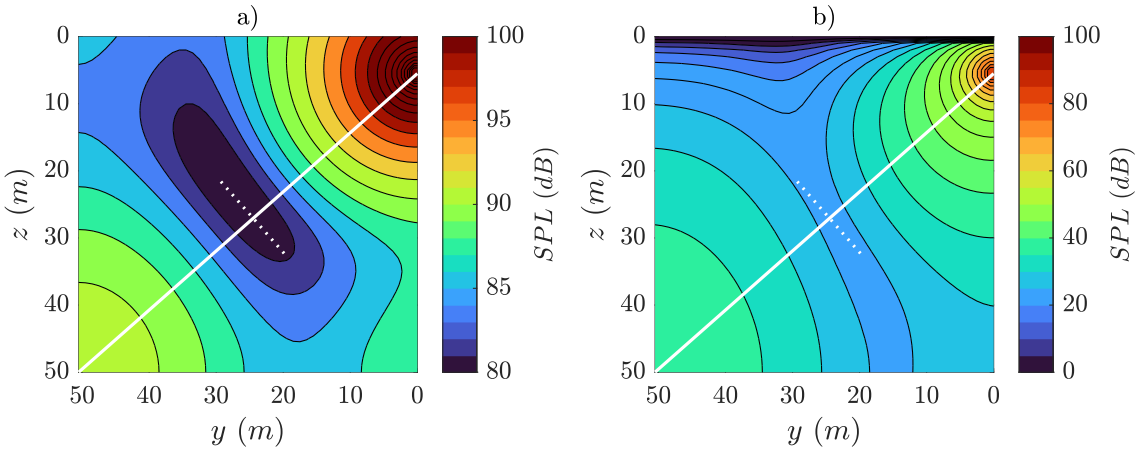

Figure 6.6: Contour of SPL of the ideal corner case *a*) and the canal case *b*) (Fig.6.4). Equation (6.2) is evaluated along the white line and the intersection with the perpendicular dashed line represents the position of the minimum at $kr = 2.0489\,(\simeq 32.6\,m)$ from the source.

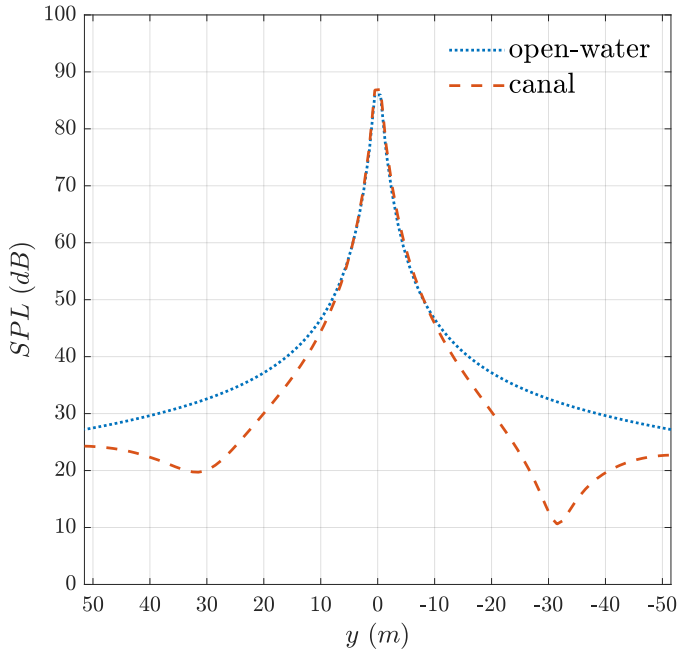

Figure 6.7: Comparison of the sound pressure level of the marine propeller in the canal case and the open-water case along the line $x = 2D$, $z = 2D$, computed with the FDTD method.

$22D\,(5.5\,m)$. Then, relative minima are observed in both positive and negative $y-direction$ at approximately $124\,D\,(31\,m)$, where a clear asymmetry is detected. At the edges of the canal, an increase of SPL is observed. For the canal case, the measured SPL on the blade plane is lower than in the open-water case, and apparently this is in contrast with Fig. 6.3, which shows that the SPL of the canal case is always greater than the open-water case. This occurs because less energy is transmitted in the blade plane for the canal case due to the boundedness of the cross sectional area, and most of the reflected energy is propagated along the canal's length. In this sense, the boundedness of the cross sectional area provides the only direction of propagation of the acoustic signal over the unlimited dimension.
In Fig.6.8 we compare the spectra of the acoustic signals, regarding open-water case and canal case, evaluated at the point $(2\,D, -126\,D, 2\,D)$, where the absolute minimum of sound pressure level of Fig. 6.7 is observed. The SL is evaluated from a pressure signal

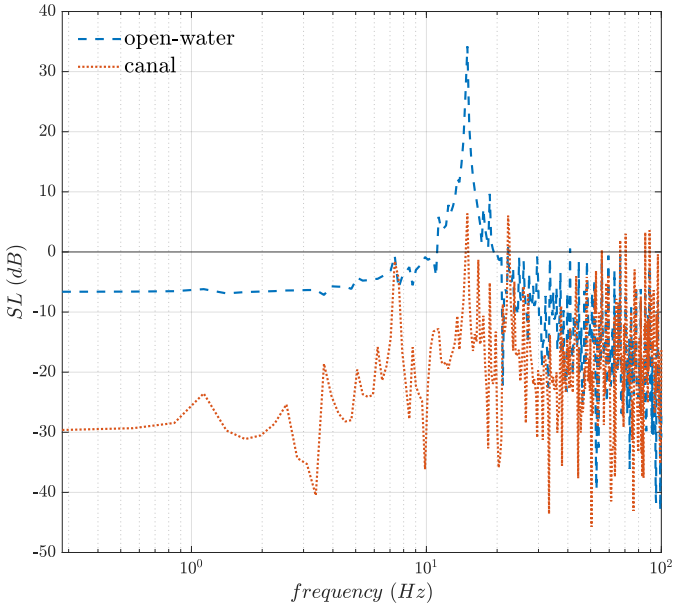

Figure 6.8: Comparison of the sound spectrum level of the marine propeller in the canal case and the open-water case along the line $(2\,D, -126\,D, 2\,D)$, , computed with the FDTD method, where the absolute minimum of sound pressure level of Fig. 6.7 is observed, computed with the FDTD method.

collected for $12\,\hat{t}$. The numerical experiment has been extended only to collect the acoustic pressure at this microphone to obtain more data for the Fourier Transform analysis. The boundedness of the domain dramatically modifies the signal, the main differences between the two cases being the complete absence of the primary peak frequency at $15\,Hz$ and the damping of the pressure signal in the low-frequency range. To be noted that the low frequencies are those primarily affected by the boundaries, whereas the high frequency part of the signal feels the boundaries as placed "in the far field".
Regions of minima of SPL other than those discussed above are present in other re-

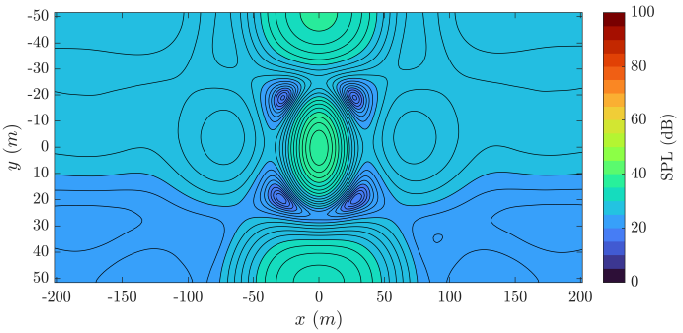

Figure 6.9: Contour of sound pressure level of the marine propeller in the canal case on the $x-y$ plane at $z = 104\,D$, computed with the FDTD method.

gions, as highlighted in Fig.6.9, where the contour of SPL of the horizontal plane at $z = 104\,D\,(26\,m)$ depth is shown. Four minimum SPL spots are located at the corner of a square of $100\,D\,(25\,m)$ side, enclosing the propeller's horizontal position, creating a region of insonification in this particular case. The distance at which the insonification occurs is comparable with the relative minimum evaluated with equation (6.1), and these effects are related to the presence of the lateral walls. It is clear that the effects are related to the lateral wall since, since in Fig. 6.3 we do not observe the presence of a minimum along the $x - direction$. Compared to the $y-z$ plane, where the path of the direct and the multiple reflected acoustic waves are analyzed on the same plane, in the $x-y$ plane, the multiple reflected waves lay on different planes than the one connecting the source and the minima. Consequently, an analytical estimation of a correct multipath factor is more complicated. Then, along the $y-direction$, a higher SPL near the lateral walls is observed, as in Fig. 6.4. The asymmetry of the SPL along this direction is even more evident.
In conclusion, the presence of boundaries generates strong inhomogeneity of the acoustic field compared to the open-water case.

6.2 Symmetry breaking rotating acoustic source

Within an unbounded domain, it is impossible to determine the rotor's direction of rotation by measuring the acoustic field of a rotating source at a single point in space. A rotor that turns clockwise or counterclockwise with respect to the single observer will produce the same acoustic field. As observed in Fig. 5.3, the acoustic energy is perfectly symmetric in any plane orthogonal to the propeller axis. However, if a free surface bounds the propagation domain the symmetry is broken. We perform an additional simulation, considering the presence of the free surface while considering all other boundaries open. In this case the marine propeller is placed $22D\,(5.5\,m)$ below the free surface as in the previous case and the acoustic pressure has been collected in the time window $2\,\hat{t} - 8\,\hat{t}$. The effects of the free surface are evident in Fig. 6.10, where we show the contour of SPL, on the plane $x = 2\,D$, which corresponds to a location upstream the propeller.
The effects of the free surface on the acoustic field, *i.e.* the asymmetry, are independent of the hydrodynamics effects that would occur if the propeller were placed in the proximity of the surface. Indeed, at the depth considered, the hydrodynamics of the propeller is not affected by the free surface, and the open-water condition of the LES simulation is valid.

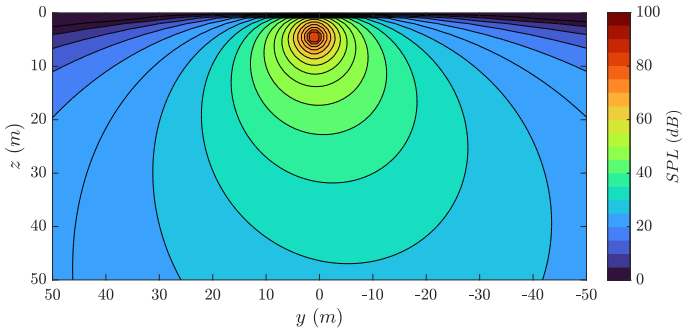

Figure 6.10: Contour of sound pressure level of the marine propeller in the free surface case on the $y-z$ plane at $x = 2D$, computed with the FDTD method.

In the SPL contour, the shadow zone near the free surface is present as in the canal case, but a clear asymmetry of the acoustic energy distribution in the plane is detected. The propeller turns counterclockwise, and an increase of SPL is observed in the direction of the fourth quadrant of a frame of reference centered at the propeller axis.
The asymmetric distribution of the acoustic energy was also verified by placing the propeller near the bottom; the latter was treated as a free surface. In this case, an increase in SPL was observed in the direction of the second quadrant. (The results are not shown). Consequently there is a relation between the direction of rotation and the free-surface location.
An asymmetry of the acoustic pressure field is also observed in Figure 8 in [12], where the authors showed the acoustic field generated by two top-in propellers, which are co-rotating in Fig. 8 *a*) [12] and counter-rotating in Fig. 8 *b*) [12]. This latter condition mimics our

experiment, where a vertical plane passing through the airframe center replaces the role of the free surface. In Fig. 8 *a*) [12], the acoustic pressure is asymmetric with respect to the airframe plane. The asymmetric acoustic pressure distribution in the space is related to the different directions of rotation of the blade relative to the airframe (direction of rotation of the marine propeller with respect to the free surface in our case). On the other hand, in Fig. 8 *b*) [12], the propellers rotate specularly with respect to the airframe, producing the same reflected field. In Fig. 8 *b*) [12] the asymmetry is clear also with respect to the $z-direction$, as in our case (Fig. 6.10). Indeed, the two propellers of Fig. 8 *b*) [12] can be interpreted as the real and the imaginary sources, where one is a mirror reflection of the other.
In order to further verify the correctness of the methodology, we evaluate the asymmetry using the FW-H equation (Eq.4.1) and compare it with the results obtained with the wave equation.

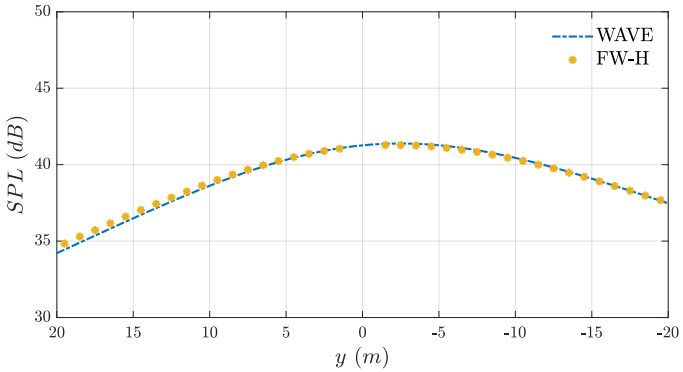

Figure 6.11: Comparison of the sound pressure level of the marine propeller in the free surface case on the line $x = 2\,D$, $z = 84\,D$ between the FW-H equation and the wave equation (WAVE)

In Fig. 6.11, the comparison of SPL between the FW-H equation (label FW-H) and the wave equation (label WAVE) is shown on the line $x = 2\,D, z = 84\,D$. The FW-H results are obtained using the method of the image. The imaginary source is equivalent to a propeller which rotates in a specular way with respect to the real one. The two methods show the same asymmetry across the $y-direction$, confirming the ability to use the wave equation instead of the image method to obtain correct estimate of the noise propagation. The SPL difference at the two opposite point of the line, see Fig. 6.11, at about $y = \pm 20m$, is of $3\,dB$. A minor difference is observed between the FW-H equation and the wave equation, however the maximum relative error is less than 1%.
We show in Fig. 6.12, a snapshot of the acoustic pressure of the marine propeller on the plane $x = 2D$ for the *open water case* (*a*) and the *free surface case* (*b*). In both cases, the range of acoustic pressure is limited in the range from $-5\times10^{-4}\,Pa$ to $5\times10^{-4}\,Pa$ to better highlight the acoustic pressure far from the source. Results are shown at the same time instant from the start of the simulation. In the *open water case*, Fig. 6.12 *a*), the dipole-like

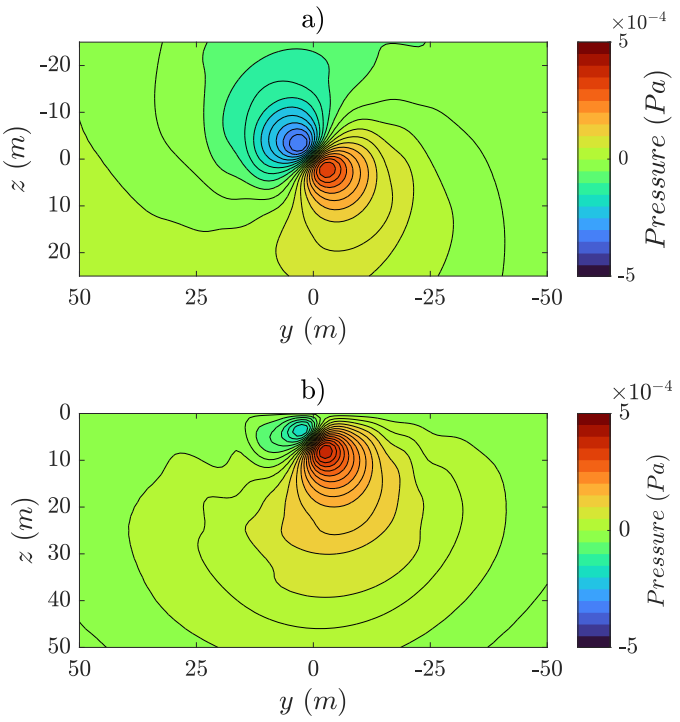

Figure 6.12: Acoustic pressure of the marine propeller on the plane $x = 2\,D$ relative to the source position: *a*) *open water* case *b*) free surface case, computed with the FDTD method.

pattern of the acoustic waves is clear near the source. Two lobes with an opposite value of pressure are identified. Far from the source, the pressure level lines bend, assuming the shape of a spiral, following the propeller's rotation. At this distance from the source, in the acoustic far-field, we cannot visualize the acoustic waves originating from the single blades but only a superposition of acoustic waves, which give rise to a signal characterized by the revolution frequency. In the near field, as discussed by [10], it is possible to visualize the transition from the near field (blade region) to a intermediate field, where the shape of the acoustic waves still "remember"the blades.

The free surface breaks the spiral symmetry of the acoustic waves, Fig. 6.12 *b*). The two lobes of the dipole pattern are still present, but they do not have the same shape as in the unbounded domain. At this instant, the positive pressure lobe is similar to Fig. 6.12 *a*), while the free surface affects the negative pressure lobe, deforming it compared to the unbounded domain case. So in the vicinity of the reflecting surface, negative and positive pressure lobes deform, alternating with the rotation. Indeed, the dipole-shaped pressure field rotates following the rotation of the propeller. The acoustic wave's wavefront, impacting the free surface, generates the asymmetry of the acoustic pressure field.

It is easier to understand the phenomenon from Fig. 6.13, where we show a schematic of Fig. 6.12. The two wavefronts generated from the dipole are displayed with a solid line,

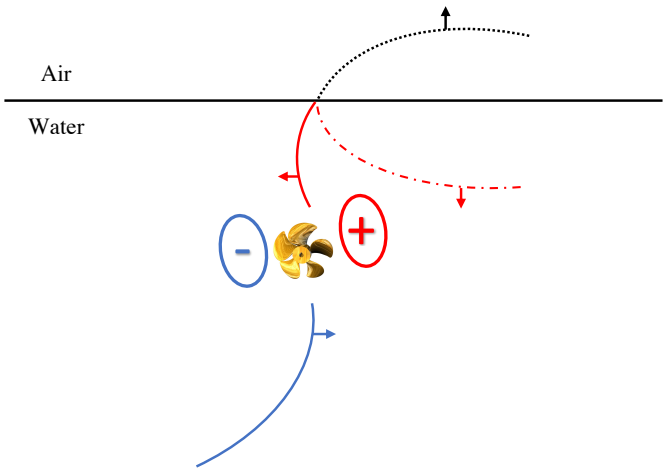

Figure 6.13: Schematic of the acoustic pressure field of Fig.6.12. The propeller is rotating counterclockwise, and we observe the figure from upstream.

and as the propeller rotates, the normal of the wavefront turns toward the direction of rotation. The dotted black line in the air region represents the wavefront if the free surface was absent, as in Fig. 6.12 *a*). In this case, the wave's wavefronts are symmetric, and the overall acoustic pressure field is symmetric, as observed in Fig. 5.3. If the interface between air and water is present, the wavefronts impact the interface always from the right side of the Figures 6.12 and 6.13. Then, the reflected acoustic wavefront, displayed in a dash-dotted red line, consistently originates from the right side. The superposition of the reflected wavefront and the direct one, which is continuously generated by the rotation of the two-lobes pressure field, leads to an increase in acoustic pressure on the right side of Fig.6.12 (*b*). Therefore, more acoustic energy is observed in the negative y-direction of Fig. 6.10 or Fig. 6.12 *b*).

Chapter 7

Scaled Marine Propeller in Stratified Medium

In this last chapter, we used the FAA methodology in conjunction with the scaling property of the FW-H equation proposed in [13] to evaluate the propagation of the noise generated by a real scale propeller in a heterogeneous stratified fluid column. In the previous chapter, we only assessed the effects of boundaries and not the presence of inhomogeneity in the medium. In this case, we considered a discontinuous stratification of the fluid column. It's a simplified representation of the environment since, in reality, the stratification is continuous but still allows us to evaluate the effects on the acoustic field. In future, we are planning to use directly real data of density and speed of sound of the water column. Indeed, they are available thanks to the Argo system [73], a fleet of Scientific CTD units deployed across all oceans. This possibility increases the fidelity of the methodology and brings us closer to representing the environment even more realistically. In the next section 7.1, we discuss the scaling of acoustic pressure from the model propeller. Then, we analyze the results in two different scenarios: a deep-sea scenario and a shallow-water scenario.

7.1 Scaling of the model propeller

The idea is to use the hydrodynamic results of the propeller LES simulation at the model scale and compute the equivalent acoustic pressure generated by a full-scale propeller. This operation is not possible in a real laboratory experiment. To get a perfect acoustic similarity between the approach and the full-scale propeller, keeping constant the Froude number and the advance ratio of the propeller J, the speed of sound must change, but this is a fluid property. Using a numerical model allows us to change the speed of sound of the medium and, accordingly, obtain a perfect similarity. We propose a scaled version (as suggested in [13]) of the FW-H equation 4.1, with the scaling factor λ, which allows us to obtain the acoustic pressure generated by a full-scale propeller with a diameter $D_f = \lambda D_s$ and the speed of sound is scaled accordingly as $c_0 = c_f/\sqrt{\lambda}$, with $c_f = 1500\,m/s$ the reference speed of sound at full scale. The scaled equation FW-H, concerning only the

linear terms, reads as follows:

$$
\begin{aligned}
4\pi\, p(\mathbf{x},t) = \lambda \frac{\partial}{\partial t} \int_S \left[\frac{\rho v_i \hat{n}_i}{4\pi r |1 - M_r|} \right]_\tau dS \\
+ \lambda\sqrt{\lambda} \frac{1}{c_0} \frac{\partial}{\partial t} \int_S \left[\frac{\tilde{p} \hat{n}_i \hat{r}_i}{4\pi r |1 - M_r|} \right]_\tau dS \\
+ \lambda \int_S \left[\frac{\tilde{p} \hat{n}_i \hat{r}_i}{4\pi r^2 |1 - M_r|} \right]_\tau dS.
\end{aligned}
\tag{7.1}
$$

With this equation we are able to compute the acoustic pressure of a full-scale propeller, scaled by a factor λ, from a model scale hydrodynamic data. In our case, we decided to scale the model by a factor $\lambda = 16$; therefore the diameter of the full-scale propeller is $D_f = \lambda D_m = 4\,m$. We note that also the frequency of the full-scale signal results scaled by a factor $\sqrt{\lambda}$, thus $f_f = f_m/\sqrt{\lambda}$, being f_m and f_f the frequency at model scale and full scale, respectively (from here on we will remove the subscript f to simplify the notation). Therefore, the revolution frequency of the propeller decreases to $3.75\,Hz$.
The nesting procedure is the same as described in section 4.4.1. We changed the dimension of the box containing the acoustic source and where the acoustic pressure is computed with the FW-H equation and the grid cell size, which in all the following simulation is set as $\Delta X = D/2\,(2\,m)$. The propeller is placed at the numerical domain's center (0, 0, 0), and the rectangular box vertexes are at $(-1D,\ -1.5D,\ 1.5D)$ and $(3.5D,\ 1.5D,\ -1.5D)$, where the x-directions is positive downstream, the z-direction is positive with increasing depth, and the y-direction is defined completing the right-handed coordinates system. Also, the source signal length is extended from $T = 0.8\,s$ to $T = 9\,s$ since the FDTD method requires a more extended signal; indeed the acoustic field needs to reach a statistically steady state before computing the p_{rms}.

7.2 Propagation in a deep sea stratified scenario

In the deep-sea scenario the only physical boundary condition considered is the air-water interface. Therefore the domain is a semi-infinite layer of fluid as shown in Figure 7.1. The water-air interface is modeled as a zero pressure boundary condition.
To mimic a semi-infinite domain, we set open boundary conditions along the x and y directions and at the bottom. As a result, the acoustic waves are able to leave the domain along the horizontal direction and across the bottom of the numerical domain. The numerical domain is $100\,D$ long in the direction of the the propeller axis (x), $850\,D$ large in the horizontal direction along the propeller blades plane (y), and $100\,D$ deep in the z-direction. The numerical grid is composed of cubic cells with side of $0.5\,D$. Two different profiles of density and speed of sound are considered. The first one is the case of homogeneous medium (Figure 7.2) with constant density and speed of sound along the fluid column (*Deep Sea* case). In this case we consider the reference value of density and speed of sound for the water.

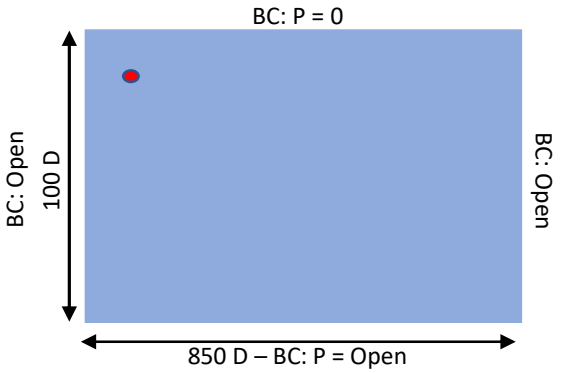

Figure 7.1: Schematic of the numerical domain for the deep-sea scenario. The red point represents the source.

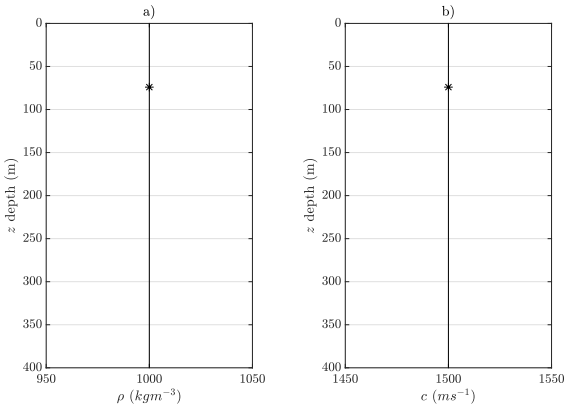

Figure 7.2: *a*) Density profile along the vertical direction (z) of the *Deep Sea* case. *b*) Speed of sound profile along the vertical direction (z) of the *Deep Sea* case.

The second profile (Figure 7.3) is representative of a stable stratified water column with a density and speed of sound jump in the upper layer of the water column (*Deep-Sea Stratified* case). In the latter case, the upper layer of water extends from the free surface $z = 0$ to 26 m of depth and has $\rho = 1019.8\,\mathrm{kg\,m^{-3}}$ ($T = 15.8\,^{\circ}\mathrm{C}$, $S =$ 27 PSU) and $c = 1500\,\mathrm{m\,s^{-1}}$; the bottom layer of water begins at a depth of 26 m and has $\rho = 1021\,\mathrm{kg\,m^{-3}}$ ($T = 10\,^{\circ}\mathrm{C}$, $S =$ 27 PSU) and $c = 1480\,\mathrm{m\,s^{-1}}$. In this case, the second fluid layer extends up to the bottom boundary of the computational domain.
In both cases the propeller is placed at ($50\,D$, $50\,D$, $19\,D$). The source is placed multiple diameters from the free surface, representing a submerged source. The propeller could also be placed near the free surface, mimicking the position of a naval propeller. To enable this low depth placement, the signal evaluated with the FWH equation and used as a source term for the wave equation should be obtained as the sum of the direct and the reflected pressure signal from the free surface. The FWH equations can be solved when considering

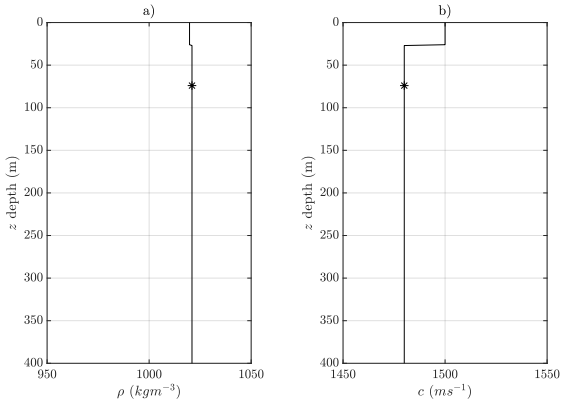

Figure 7.3: *a*) Density along the vertical direction (z) of the *Deep Sea Stratified* case. *b*) Speed of sound along the vertical direction (z) of the *Deep Sea Stratified* case.

a single boundary. Therefore the only complexity is the evaluation of the contribution of the reflected signal.
The data are collected in the time window 3 s-9 s, allowing the acoustic pressure to reach a statistical steady state. The time window in which the data are collected is defined using the reference speed of sound of $c = 1500\,\mathrm{m\,s^{-1}}$ and the farthest distance from the source along an horizontal line ($750\,D$). This allows the acoustic wave to travel at least three times from the source to the boundary, since the time needed to reach the right boundary is about 2 s. The choice of the time window is related to the dimension of the computational domain; the larger is the domain, the larger is the time required to record the data. Our choice of the time domain is done using this criterion.
In Figure 7.4 the SPL over the $y - z$ plane passing through the propeller blades axis for the *Deep Sea Stratified* case is shown. Along this plane, an axial symmetry of the SPL is observed near the propeller. The air-water interface breaks the symmetry, and most acoustic energy is deflected toward the bottom boundary. A lower sound zone is observed near the surface, and its depth increases with the distance.
In Figure 7.5 the SPL difference between the *Deep Sea Stratified* and the *Deep Sea* case over the $y - z$ plane passing through the propeller blades axis is shown. There are three noteworthy points to notice. First, we observe an increase of SPL in the upper layer of the *Deep Sea Stratified* since part of the acoustic energy is trapped inside the first water layer. Second, there is a decrease of SPL just below the density and speed of sound jump, which increase with the distance from the source. These two effects are located in the shadow zone, where there is a minimum of SPL. Third, there is an increase of SPL, for the *Deep Sea Stratified* case, in the rest of the water layer, apart from the zone right below the propeller. The increase of SPL is not constant, but a wavy pattern appears. The differences in SPL are low compared to the SPL measure across the domain, but they clearly depend on the characters of the density and speed of the sound profile along the fluid column.

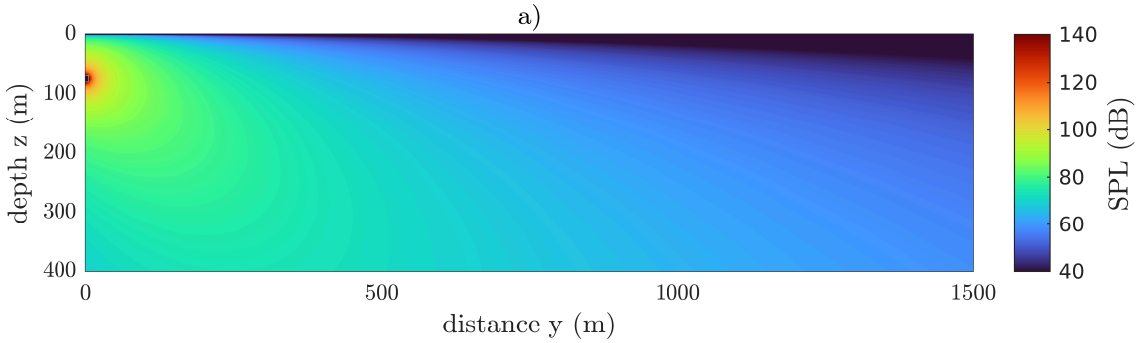

Figure 7.4: Sound Pressure Level of the scaled SVA VP1304 marine propeller over the $y-z$ plane passing trough the propeller blades axis for the *Deep Sea Stratified* case.

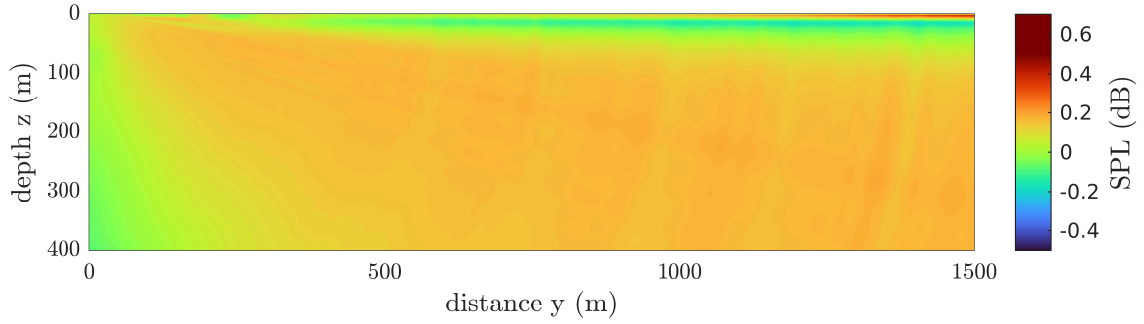

Figure 7.5: Sound Pressure Level difference between the *Deep Sea Stratified* and the *Deep Sea* cases of the scaled SVA VP1304 marine propeller over the $y-z$ plane passing through the propeller blades axis.

7.3 Propagation in a shallow water stratified scenario

In the shallow water scenario, the only physical boundary condition considered is the air-water interface, but we add a sediment layer that mimics the seabed, as shown in Figure 7.6. In this scenario, the acoustic waves after reaching the sediment layer are reflected in the fluid layer or refracted inside the sediment layer. In the sediment layer, only the compressional waves are solved. As a consequence the sediment layer is treated as a fluid layer.

The numerical domain is the same as for the deep-sea scenario, and open boundary conditions are employed along the x and y directions and at the bottom of the sediment layer. Therefore a hard bottom, which reflects all the acoustic waves, is not present; the acoustic waves entering the sediment layer can exit at the bottom of the numerical domain since an open-boundary condition is present. This is an approximation of the seabed since a perfect knowledge of the solid structure with the depth is required to model exactly the propagation of the sound. This scenario is considered as a model of a real environment. The same density and speed of sound profiles of the deep sea case are used also. In the first

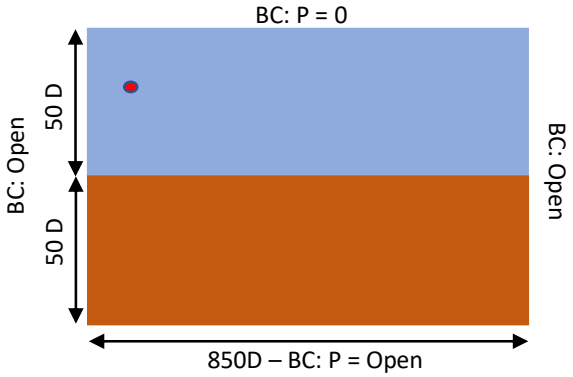

Figure 7.6: Schematic of the Shallow Water scenario. The red point represents the source.

case (Figure 7.7) water is considered as an homogeneous medium (*Shallow Water* case). The water layer has a density of $\rho = 1000\,\mathrm{kg\,m^{-3}}$, and a speed of sound $c = 1500\,\mathrm{m\,s^{-1}}$. The sediment layer has a density of $\rho = 1800\,\mathrm{kg\,m^{-3}}$, and a speed of sound $c = 1800\,\mathrm{m\,s^{-1}}$. We chose these properties for the sediment layer since they are used in benchmark cases to validate the ocean acoustic propagation models.

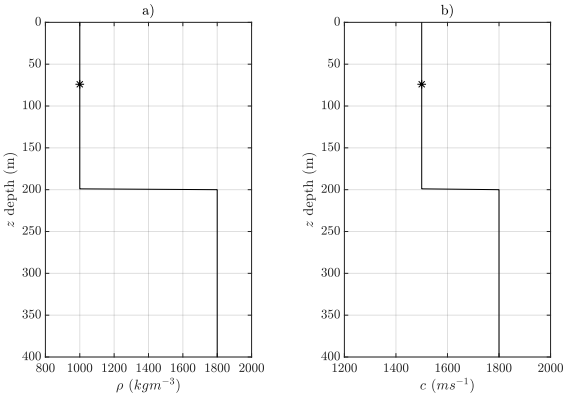

Figure 7.7: *a*) Density profile along the vertical direction (z) of the *Shallow Water* case. *b*) Speed of sound profile along the vertical direction (z) of the *Shallow Water* case.

In the second case labeled *Shallow Water Stratified*, the same jump of density and speed of sound for the water layer as the *Deep Sea Stratified* case is used. (Figure 7.8). Therefore, two different layers of fluid are considered in the shallow water column, and the property of the sediment layer are the same as in the *Shallow Water* case. The first layer of water extends from 0 to 26 m of depth and has $\rho = 1019.8\,\mathrm{kg\,m^{-3}}$ ($T = 15.8\,^{\circ}\mathrm{C}$, $S = 27$ PSU) and $c = 1500\,\mathrm{m\,s^{-1}}$; the second layer of water begins at a depth of 26 m and has $\rho = 1021\,\mathrm{kg\,m^{-3}}$ ($T = 10\,^{\circ}\mathrm{C}$, $S = 27$ PSU) and $c = 1480\,\mathrm{m\,s^{-1}}$.
As in the deep sea senario, the propeller is placed at ($50D$, $50\,D, 19\,D$) and the data are collected in the time window 3 s-9 s.

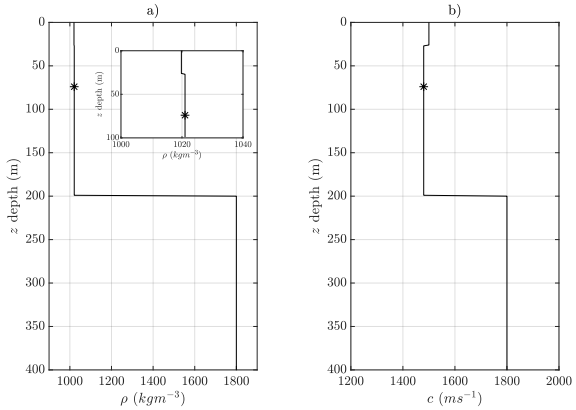

Figure 7.8: *a*) Density profile along the vertical direction (z) of the *Shallow Water Stratified* case. *b*) Speed of sound profile along the vertical direction (z) of the *Shallow Water Stratified* case.

In Figure 7.9 the SPL over the $y-z$ plane passing through the propeller blades axis for the *Shallow Water Stratified* case is shown. The SPL values, in this scenario, are higher than the *Deep Sea Stratified* since the energy is constrained inside the water layer due to the seabed. The majority of the acoustic waves are reflected by the sediment layer. A lower sound zone is also observed in this case, but the zone is narrower compared to the *Deep Sea Stratified*. Another important aspect is that, in the far-field (compared to the source's depth), a maximum of the SPL is observed in a small layer above the seabed. This effect is related to the higher speed of sound in the sediment layer. The presence of the seabed highly influences the SPL distribution. The distance and depth at which experimental measurements are conducted can greatly vary the outcome, and the presence of the seabed should be taken into consideration.

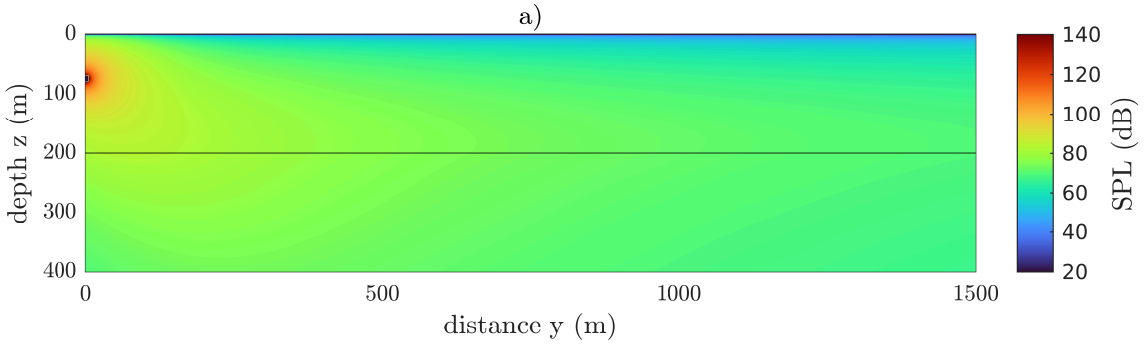

Figure 7.9: Sound Pressure Level of the scaled SVA VP1304 marine propeller over the $x-z$ plane passing trough the propeller axis for the *Shallow Water Stratified* case.

In Figure 7.10 the SPL difference between the *Shallow Water Stratified* and the *Shallow Water* case over the $y-z$ plane passing through the propeller blades axis is shown. The

SPL is almost equal up to 500 m from the source. Interference zones are observed in the first layer of fluid below the air-water interface, highlighted by higher and lower SPL spots perpendicular to the air-water interface. After 1000 m, the interference zones are also observed parallel to the air-water interface. The SPL of the *Shallow Water Stratified* case increases, compared to the *Shallow Water* case, in the water column. The stratification enhances the acoustic energy trapped inside the fluid layer.

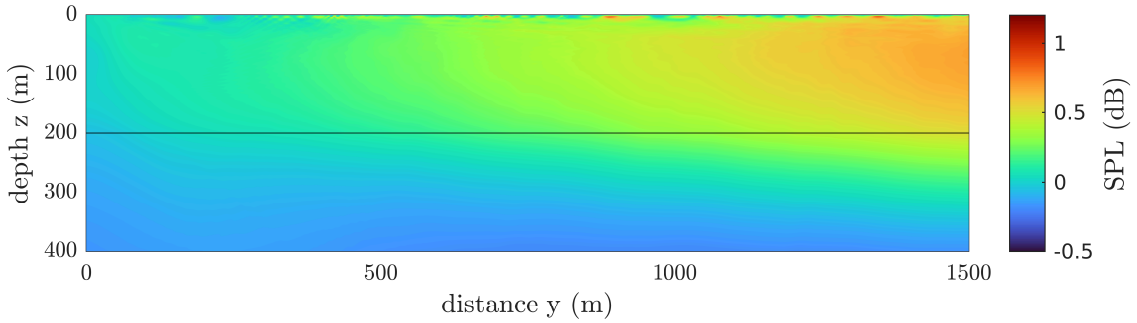

Figure 7.10: Sound Pressure Level difference between the *Shallow Water Stratified* and the *Shallow Water* cases of the scaled SVA VP1304 marine propeller over the $y - z$ plane passing trough the propeller blades axis.

Chapter 8

Conclusions

In the present thesis, the Full Acoustic Analogy methodology was developed to evaluate the acoustic propagation in a bounded inhomogeneous domain. This methodology opens the possibility of better evaluating and understanding noise propagation and eventually monitoring the noise hazard in the marine environment. To apply the methodology, we first developed a propagation model based on the solution of the acoustic wave equation. The propagation model relies on the finite-difference-time-domain method to solve the wave equation in space and time, using a second-order numerical scheme. The algorithm implements the perfectly matched layer (PML) boundary conditions to minimise the spurious reflection of acoustic waves occurring at the open boundaries of the numerical domain. A new method for implementing the acoustic source was defined, increasing the accuracy of the results, particularly in case of a single reflecting boundary, such as a free surface.
We extensively compared analytical and numerical solutions for archetypal sources (monopole, dipole, and quadrupole) in a semi-infinite homogeneous water domain. Successively, we investigate the propagation of the acoustic signals in the Ideal waveguide and the Pekeris waveguide. These tests were necessary to evaluate the accuracy of the propagation model. Then, we investigated how the source directivity may affect the acoustic field patterns, considering the case of a Pekeris waveguide. The results showed that a spherically symmetric source (i.e. monopole) is not sufficient to characterize complex acoustic sources. Indeed, the energy distribution in the fluid waveguide is strongly affected by the source type and the environment.
A natural development possible improvement of the developed solver is the implementation of a higher-order method for the solution of the wave equation and a better general optimization of the algorithm, therefore expanding the applicability range of the propagation method. For what concerns the physical modelling, two aspects worth investigating are implementing a dissipative model, at least for the sediment layer, and considering the scattering of an immersed object. The major obstacle for the dissipative model is compatibility with the open-boundary conditions. We are currently working on the scattering of acoustic waves incident to an object, which requires reformulating the boundary conditions. In terms of underwater propagation, this would allow accounting for the ship hull,

for example, and its consequent effects on the acoustic fields.
In the second part of the thesis, we introduced the new methodology FAA composed of three steps: i) a numerical simulation of the fluid flow to obtain the hydrodynamics field of the problem of interest; ii) the integral form of the FW-H equation is used to contain the acoustic pressure in the near field of the noise source; iii) the propagation model developed is used for the propagation of acoustic waves in complex domain. The first two step defines the classical acoustic analogy method. Next, we add the third step to overcome some known limitations of acoustic analogies. The methodology couples the advantages of the acoustic analogy with the flexibility given by the wave equation, which allows calculating the noise propagation in a realistic domain characterized by the presence of boundaries and fluid inhomogeneity.
Inserting the acoustic signals obtained by means of the FW-H equation in the propagation model is carried out using the hard source method. Although the methodology is of general use, here it is applied to a marine propeller. Verification of the methodology has been carried out in open-water conditions and in presence of a water-air interface. We successively studied the case of a propeller emitting noise in a canal bounded by the free surface and by three reflecting walls, namely lateral and bottom surfaces. It was shown how the boundaries in the marine environment largely affect the propagation of acoustic waves. The noise distribution loses the typical shape that characterizes the open water case and exhibits a complex pattern with local minima and maxima, depending on the combination of direct and reflected waves. The spatial decay of the acoustic field is similar to that of the open water case in the near field only; with increasing distance from the source, the decay rate changes, and the change of slope occurs at specific distances from the source related to the distance of the source from the boundaries and to the dominant wave lengths.
Moreover, the rotation of the propeller, combined with the presence of the free surface, gives rise to an asymmetric distribution of the acoustic signal over the planes parallel to the propeller axis. This is attributed to the fact that rotation modifies the composition of the direct and reflected waves increasing the overall signal by one side of the propeller.
The results of this thesis may be helpful for the analysis of signals propagated in real-scale confined regions, as well as for the analysis of laboratory-scale experiments carried out in water tunnels.
In the future, we will also consider the contribution of the volume term of the FW-H equation, in particular, understanding the cause of the overestimation of the acoustic pressure observed with the wave equation. In conjunction, we plan to consider a stratified domain, characterized by continuous density variations along the fluid column, to address the presence of a bathymetry profile, possibly studying a natural marine environment. The methodology presented still needs to consider the propeller's forward motion, which may be relevant in the case of high-speed marine vehicles. Therefore we are going to investigate this aspect.

Bibliography

[1] M. A. Ainslie and J. G. McColm. A simplified formula for viscous and chemical absorption in sea water. *The Journal of the Acoustical Society of America*, 103(3):1671–1672, 1998.

[2] Kostas Belibassakis, John Prospathopoulos, and Iro Malefaki. Scattering and directionality effects of noise generation from flapping thrusters used for propulsion of small ocean vehicles. *Journal of Marine Science and Engineering*, 10(8):1129, 2022.

[3] R. Bensow and M. Liefvendahl. An acoustic analogy and scale-resolving flow simulation methodology for the prediction of propeller radiated noise, 2016. Paper presented at the 31^{st} Symposium on Naval Hydrodynamics, 11-16 September 2016, Monterey.

[4] R. E Bensow and G. Bark. Implicit les predictions of the cavitating flow on a propeller. *Journal of fluids engineering*, 132(4), 2010.

[5] J. Bezanson, S. Karpinski, V. B. Shah, and A. Edelman. Julia: A fast dynamic language for technical computing. *arXiv preprint arXiv:1209.5145*, 2012.

[6] S. Bilbao and B. Hamilton. Directional sources in wave-based acoustic simulation. *IEEE/ACM Transactions on Audio, Speech, and Language Processing*, 27(2):415–428, 2018.

[7] D. Botteldooren. Finite-difference time-domain simulation of low-frequency room acoustic problems. *The Journal of the Acoustical Society of America*, 98(6):3302–3308, 1995.

[8] L. M. Brekhovskikh, Y. P. Lysanov, and J. P. Lysanov. *Fundamentals of ocean acoustics*. Springer Science & Business Media, 2003.

[9] R. Broglia, M. Cianferra, A. Posa, M. Felli, and V. Armenio. Hydroacoustic analysis of a marine propeller in open water conditions through les and acoustic analogy, 2020. Paper presented at the 33^{rd} Symposium on Naval Hydrodynamics, October 2020, Osaka, Japan.

[10] C. J. Chapman. The structure of rotating sound fields. *Proceedings of the Royal Society of London. Series A: Mathematical and Physical Sciences*, 440(1909):257–271, 1993.

[11] A. Chern. A reflectionless discrete perfectly matched layer. *Journal of Computational Physics*, 381:91–109, 2019.

[12] G. Chirico, G. N. Barakos, and N. Bown. Propeller installation effects on turboprop aircraft acoustics. *Journal of Sound and Vibration*, 424:238–262, 2018.

[13] M. Cianferra and V. Armenio. Scaling properties of the ffowcs-williams and hawkings equation for complex acoustic source close to a free surface. *Journal of Fluid Mechanics*, 927, 2021.

[14] M Cianferra, S Ianniello, and V Armenio. Assessment of methodologies for the solution of the ffowcs williams and hawkings equation using les of incompressible single-phase flow around a finite-size square cylinder. *Journal of Sound and Vibration*, 453:1–24, 2019.

[15] M. Cianferra, A. Petronio, and V. Armenio. Non-linear noise from a ship propeller in open sea condition. *Ocean Engineering*, 191:106474, 2019.

[16] MSC Maritime Safety Committee et al. Adoption of the code on noise levels on board ships. *Englisch. Techn. Ber. MSC*, 337:91, 2012.

[17] N. Curle. The influence of solid boundaries upon aerodynamic sound. *Proceedings of the Royal Society of London. Series A. Mathematical and Physical Sciences*, 231(1187):505–514, 1955.

[18] L. M. B. da Costa Campos, M. J. dos Santos Silva, and A. R. A. da Fonseca. On the multipath effects due to wall reflections for wave reception in a corner. *Noise Mapping*, 8(1):41–64, 2021.

[19] M. A. Dablain. The application of high-order differencing to the scalar wave equation. *Geophysics*, 51(1):54–66, 1986.

[20] P. Di Francescantonio. A new boundary integral formulation for the prediction of sound radiation. *Journal of Sound and Vibration*, 202(4):491–509, 1997.

[21] Strategy Framework Directive. Directive 2008/56/ec of the european parliament and of the council. *European Parliament*, 2008.

[22] B. Engquist and A. Majda. Absorbing boundary conditions for numerical simulation of waves. *Proceedings of the National Academy of Sciences*, 74(5):1765–1766, 1977.

[23] C. Erbe, S. A. Marley, R. P. Schoeman, J. N. Smith, L. E. Trigg, and C. B. Embling. The effects of ship noise on marine mammals—a review. *Frontiers in Marine Science*, page 606, 2019.

[24] P. C. Etter. Advanced applications for underwater acoustic modeling. *Advances in Acoustics and Vibration*, 2012, 2012.

[25] M. Felli, S. Grizzi, and M. Falchi. A novel approach for the isolation of the sound and pseudo-sound contributions from near-field pressure fluctuation measurements: analysis of the hydroacoustic and hydrodynamic perturbation in a propeller-rudder system. *Experiments in fluids*, 55(1):1–17, 2013.

[26] J. E. Ffowcs Williams and D. L. Hawkings. Sound generation by turbulence and surfaces in arbitrary motion. *Philosophical Transactions of the Royal Society of London. Series A, Mathematical and Physical Sciences*, 264(1151):321–342, 1969.

[27] J. R. Fricke. Acoustic scattering from elemental arctic ice features: Numerical modeling results. *The Journal of the Acoustical Society of America*, 93(4):1784–1796, 1993.

[28] Y. Gao, H. Song, J. Zhang, and Z. Yao. Comparison of artificial absorbing boundaries for acoustic wave equation modelling. *Exploration Geophysics*, 48(1):76–93, 2017.

[29] O. A. Godin. Anomalous transparency of water-air interface for low-frequency sound. *Physical review letters*, 97(16):164301, 2006.

[30] E. Hafla, E. Johnson, C. N. Johnson, L. Preston, D. Aldridge, and J. D. Roberts. Modeling underwater noise propagation from marine hydrokinetic power devices through a time-domain, velocity-pressure solution. *The Journal of the Acoustical Society of America*, 143(6):3242–3253, 2018.

[31] C. H. Harrison. Acoustic shadow zones in the horizontal plane. *The Journal of the Acoustical Society of America*, 65(1):56–61, 1979.

[32] J. A. Hildebrand. Anthropogenic and natural sources of ambient noise in the ocean. *Marine Ecology Progress Series*, 395:5–20, 2009.

[33] S. Ianniello. The ffowcs williams–hawkings equation for hydroacoustic analysis of rotating blades. part 1. the rotpole. *Journal of Fluid Mechanics*, 797:345–388, 2016.

[34] S. Ianniello and E. De Bernardis. Farassat's formulations in marine propeller hydroacoustics. *International Journal of Aeroacoustics*, 14(1-2):87–103, 2015.

[35] S. Ianniello and E. De Bernardis. Farassat's formulations in marine propeller hydroacoustics. *International Journal of Aeroacoustics*, 14(1-2):87–103, 2015.

[36] F. B. Jensen and C. M. Ferla. Numerical solutions of range-dependent benchmark problems in ocean acoustics. *The Journal of the Acoustical Society of America*, 87(4):1499–1510, 1990.

[37] F. B. Jensen, W. A. Kuperman, M. B. Porter, H. Schmidt, and A. Tolstoy. *Computational ocean acoustics*, volume 794. Springer, 2011.

[38] J. Keller, P. Kumar, and K. Mahesh. Examination of propeller sound production using large eddy simulation. *Physical Review Fluids*, 3(6):064601, 2018.

[39] P. Kumar and K. Mahesh. Large eddy simulation of propeller wake instabilities. *Journal of Fluid Mechanics*, 814:361–396, 2017.

[40] R. F. Kunz, D. A. Boger, D. R. Stinebring, T. S. Chyczewski, J. W. Lindau, H. J. Gibeling, S. Venkateswaran, and T. Govindan. A preconditioned navier–stokes method for two-phase flows with application to cavitation prediction. *Computers & Fluids*, 29(8):849–875, 2000.

[41] G. Kuznetsov and A. Stepanov. The field of an equivalent multipole composite radiator in a waveguide. *Acoustical Physics*, 53(3):326–334, 2007.

[42] G. Kuznetsov and A. Stepanov. Approximate analytic representations of laws of attenuation in vector-scalar fields of multipole sources in a pekeris waveguide. *Acoustical Physics*, 63(6):660–672, 2017.

[43] M. J. Lighthill. On sound generated aerodynamically i. general theory. *Proceedings of the Royal Society of London. Series A. Mathematical and Physical Sciences*, 211(1107):564–587, 1952.

[44] Y. Lin, M. B. Porter, F. Sturm, M. J. Isakson, and C. Chiu. Introduction to the special issue on three-dimensional underwater acoustics. *The Journal of the Acoustical Society of America*, 146(3):1855–1857, 2019.

[45] I. Malefaki and K. Belibassakis. A novel fdtd–pml scheme for noise propagation generated by biomimetic flapping thrusters in the ocean environment. *Journal of Marine Science and Engineering*, 10(9):1240, 2022.

[46] M. F. McKenna, D. Ross, S. M. Wiggins, and J. A. Hildebrand. Underwater radiated noise from modern commercial ships. *The Journal of the Acoustical Society of America*, 131(1):92–103, 2012.

[47] C. Meneveau, T. S. Lund, and W. H. Cabot. A lagrangian dynamic subgrid-scale model of turbulence. *Journal of fluid mechanics*, 319:353–385, 1996.

[48] R. Muscari, A. Di Mascio, and R. Verzicco. Modeling of vortex dynamics in the wake of a marine propeller. *Computers & Fluids*, 73:65–79, 2013.

[49] P. L. Nielsen, M. Zampolli, R. Le Bras, P. Mialle, P. Bittner, A. Poplavskiy, M. Rozhkov, G. Haralabus, E. Tomuta, R. Bell, et al. Ctbto's data and analysis pertaining to the search for the missing argentine submarine ara san juan. *Pure and Applied Geophysics*, 178(7):2557–2577, 2021.

[50] M. P. Norton and D. G. Karczub. *Fundamentals of noise and vibration analysis for engineers*. Cambridge university press, 2003.

[51] United Nations Convention on the Law of the Sea (UNCLOS). 1833 unts 397, 21 ilm 1261. ., 2008.

[52] IMO International Maritime Organization. Guidelines for the reduction of underwater noise from commercial shipping to address adverse impacts on marine life. *MEPC*, 2014.

[53] G. Petris, M. Cianferra, and V. Armenio. Marine propeller noise propagation within bounded domains. *Ocean Engineering*, 265:112618, 2022.

[54] G. Petris, M. Cianferra, and V. Armenio. A numerical method for the solution of the three-dimensional acoustic wave equation in a marine environment considering complex sources. *Ocean Engineering*, 256:111459, 2022.

[55] P. Petrov, A. Zakharenko, and M Y. Trofimov. The wave equation with viscoelastic attenuation and its application in problems of shallow-sea acoustics. *Acoustical Physics*, 58(6):700–707, 2012.

[56] Allan D Pierce. *Acoustics: an introduction to its physical principles and applications*. Springer, 2019.

[57] A. Posa, R. Broglia, M. Felli, M. Cianferra, and V. Armenio. Hydroacoustic analysis of a marine propeller using large-eddy simulation and acoustic analogy. *Journal of Fluid Mechanics*, 947:A46, 2022.

[58] A. Posa, M. Felli, and R. Broglia. The signature of a propeller rudder system: Acoustic analogy based on les data. *Ocean Engineering*, 259:112059, 2022.

[59] S. W. Rienstra and A. Hirschberg. An introduction to acoustics. *Eindhoven University of Technology*, 18:19, 2004.

[60] Y. Saito, R. Takami, I. Nakamori, and T. Ikohagi. Numerical analysis of unsteady behavior of cloud cavitation around a naca0015 foil. *Computational Mechanics*, 40(1):85–96, 2007.

[61] L. Savioja. Real-time 3d finite-difference time-domain simulation of low-and mid-frequency room acoustics. In *13th Int. Conf on Digital Audio Effects*, volume 1, page 75, 2010.

[62] J. B. Schneider, C. L. Wagner, and S. L. Broschat. Implementation of transparent sources embedded in acoustic finite-difference time-domain grids. *The Journal of the Acoustical Society of America*, 103(1):136–142, 1998.

[63] S. Sezen, M. Atlar, P. Fitzsimmons, N. Sasaki, G. Tani, N. Yilmaz, and B. Aktas. Numerical cavitation noise prediction of a benchmark research vessel propeller. *Ocean Engineering*, 211:107549, 2020.

[64] J. Sheaffer, M. van Walstijn, and B. Fazenda. Physical and numerical constraints in source modeling for finite difference simulation of room acoustics. *The Journal of the Acoustical Society of America*, 135(1):251–261, 2014.

[65] F. Sturm. Numerical study of broadband sound pulse propagation in three-dimensional oceanic waveguides. *The journal of the acoustical society of America*, 117(3):1058–1079, 2005.

[66] SVA-VP1304. https://www.sva-potsdam.de/en/potsdam-propeller-test-case-pptc, 2011. Proceedings of the Second International Symposium on Marine Propulsors - smp'11, 15 – 17 June 2011, Hamburg, Germany.

[67] J. T. Tate and L. J. Spitzer. Physics of sound in the sea: Summary technical report of division 6. *US Government Printing Office, Washington DC*, page 566, 1946.

[68] A. Tolstoy. 3-d propagation issues and models. *Journal of Computational Acoustics*, 4(03):243–271, 1996.

[69] M. Wang, J. B. Freund, S. K. Lele, et al. Computational prediction of flow-generated sound. *Annual Review of Fluid Mechanics*, 38(1):483–512, 2006.

[70] L. S. Weilgart. A brief review of known effects of noise on marine mammals. *International Journal of Comparative Psychology*, 20(2), 2007.

[71] H. Weinberg and R. E. Keenan. Gaussian ray bundles for modeling high-frequency propagation loss under shallow-water conditions. *The Journal of the Acoustical Society of America*, 100(3):1421–1431, 1996.

[72] D. Wittekind and M. Schuster. Propeller cavitation noise and background noise in the sea. *Ocean Engineering*, 120:116–121, 2016.

[73] A. P. S. Wong, S. E. Wijffels, S. C. Riser, S. Pouliquen, S. Hosoda, D. Roemmich, J. Gilson, G. C. Johnson, K. Martini, D. J. Murphy, et al. Argo data 1999–2019: two million temperature-salinity profiles and subsurface velocity observations from a global array of profiling floats. *Frontiers in Marine Science*, 7:700, 2020.

Acknowledgment

The present research has been developed within the Ph.D. Program Earth Science, Fluid-Dynamics, and Mathematics (ESFM) and was supported by OGS, Italy and CINECA, Italy under HPC-TRES program award number 2019–05.